University of California
Santa Cruz

The Molecular Mechanisms of Cell Cycle Regulation by CDK4, DREAM, and Myb-MuvB Complexes

A dissertation submitted in partial satisfaction of the requirements for the degree of

DOCTOR OF PHILOSOPHY

in

CHEMISTRY

by

Keelan Z. Guiley

June 2018

The dissertation of Keelan Z. Guiley is approved:

_____
Professor Seth Rubin, chair

_____
Professor Susan Strome

_____
Professor Michael Stone

_____
Tyrus Miller
Vice Provost and Dean of Graduate Studies

Table of Contents **Page**

List of Figures **Page**

Chapter 1

Chapter 2

Chapter 5

List of Tables

Chapter 2

Chapter 3

Chapter 4

Abstract:

The Rb family (p130, p107 and Rb) are tumor suppressor proteins that are frequently inactivated in human cancers. p130 and p107 form the DREAM complex to regulate quiescence while Rb-E2F regulates G_1 of the cell cycle. The Rb family prevents cell cycle entry and proliferation by suppressing E2F directed gene activation. The activation of cyclin dependent kinases following growth stimulation results in serine/threonine phosphorylation of the Rb proteins resulting in release of E2F. Following DREAM and Rb-E2F complex inactivation by CDK phosphorylation, E2F and the Myb-MuvB complex activate genes required for DNA synthesis and mitosis. This study focuses on the molecular mechanisms that CDKs and oncogenic viruses use to inactivate DREAM and Rb-E2F complexes to activate E2F and Myb-MuvB in cancer.

Acknowledgements:

I would like to acknowledge my lovely wife Thy Guiley for her love, support, and upmost patience throughout the 6 years of graduate school. I would like to thank my graduate advisor Dr. Seth Rubin for providing the training and guidance for me to develop as a biochemist, a public speaker, and a scientific writer. Seth goes well beyond what is expected from a mentor to assure that his students are successful. I would like to thank Dr. Carrie Partch who I considered a second advisor through all of her generous support in developing my career and providing insight into the structural and biochemical experiments included in this dissertation research. I would like to thank my family (Guiley and Bui) and friends for their inspiration to pursue a career in science. I would like to thank my labmates, “the Rubinites”, both past and present for all of the training and help on my projects, and for all of humor that makes the lab a great place to be. I would like to thank my thesis committee members Dr. Susan Strome and Dr. Michael Stone for their invaluable insight on my dissertation research. I would like to thank the Partch Lab both past and present for all of their suggestions on my projects in our weekly lab meetings. I would like to thank my cohort; Dr. Andrew MacRae, Dr. Andreea Nistorica, Dr. Joe Dahl, Dr. Chelsea Gustafson and Dr. Kate Markham for all of the good times and great support network we had throughout graduate school. Finally, I would like to thank Dr. Ilan Benjamin, Janet Jones, Karen Meece, Katie Cramton and the Department of Chemistry and Biochemistry at UC Santa Cruz for providing all of the resources necessary to run this fantastic graduate program.

Chapter 1: The Cell Cycle and Cancer: Rb and p53 Loss of Function in Cancer

1.1 Introduction

1.1.1 The cell cycle

The ability of cells to divide and differentiate constitutes the building blocks for multi-cellular organisms and complex life. When cells divide uncontrollably, the integrity of the genome and the physiology of the organism is at risk. The origin of irregular cell growth can be attributed to the loss-of-function of genes involved in preventing tumors known as tumor suppressor genes, or due to the activation of genes involved in promoting cell growth and migration known as oncogenes. The ability of tumor cells to evade tumor suppressors

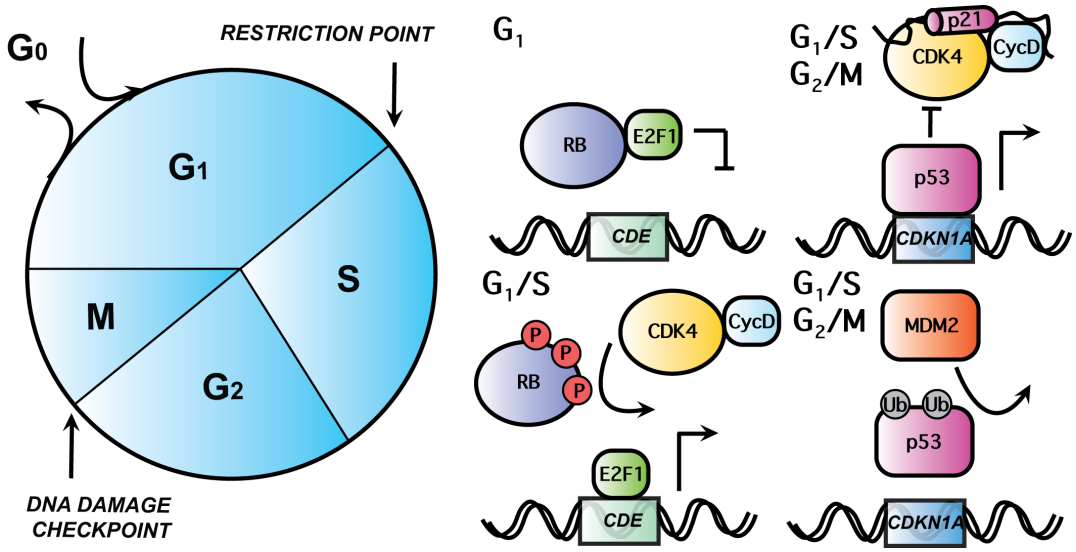

Figure 1.1 Rb and p53 are key regulators of cell division. There are two major checkpoints that are regulated by Rb and p53 during the cell cycle, the restriction point at G_1/S and the DNA damage checkpoint at G_2/M. Rb and p53 repress cell-cycle genes by sequestering E2F activators and expressing the CDK inhibitor p21. Phosphorylation of Rb by CDK4 allows for release of E2F and cell-cycle gene activation. p21 can inhibit CDK4, CDK2 and CDK1 to prevent Rb phosphorylation and cell cycle progression. Ubiquitination of p53 by MDM2 results in proteasomal degradation and relieving CDK inhibition and allowing cells to divide.

represents one of the hallmarks of cancer (Hanahan and Weinberg 2000). The loss-of-function of tumor suppressor genes can arise from inherited mutations, mutations acquired from carcinogens, from infection of oncogenic viruses, or through silencing by epigenetic

modifications (Hanahan and Weinberg 2011)(Dawson 2017)(Mesri et al. 2014). Many tumor suppressor genes and oncogenes are direct regulators of cell division.

The sequential set of events that occurs in order for a cell to divide is known as the cell cycle, and this process can be characterized by distinct phases. When cells initially decide to divide, they enter a growth phase to prepare for the replication of the genome. This initial growth preparation is known as the gap phase, or G_1. It is during G_1 that cells remain on stand-by until given the proper cues to divide such as mitogens and space (Lloyd 2013). Loss of regulation during G_1 is a common theme in cancer, in which alterations in tumor suppressor genes or oncogenes allows cells to progress into mitosis in the absence of growth factor signaling (Foster et al. 2011). If the cell does not receive growth stimulation in G_1 for an extended period, it will exit the cell cycle in a reversible state of resting called quiescence (G_0). If the cell is successful in progressing through G_1, it is committed to cell division and is no longer influenced by external growth factors (Zetterberg et al. 1995).

1.1.2 *Rb and G_1 restriction point*

The most well characterized negative regulator of the G_1/S transition is the *RB1* gene product, Rb (**Figure 1.1**). The first characterization of *RB1* came from a statistical analysis of a rare pediatric cancer, retinoblastoma, that develops in children that have inherited a *RB1* deleterious mutation in one allele and suffer another mutation in the second allele in retinoblasts during development of the retina (Knudson 2001). This type of cancer can also arise from somatic mutations in both alleles without inheritance from either parent. Alfred Knudson was the first to discover that retinoblastoma only develops when both alleles of *RB1* are altered. His model for the origin of this cancer became known as his “two-hit” hypothesis (Knudson 1971). The concept that the loss of one gene could give rise to cancer was a major turning point in cancer biology, and represents the first description of a tumor suppressor gene. Prior to Knudson’s “two-hit” hypothesis, the Hermann Muller model was that, in general, excessive somatic mutations drove tumorigenesis (Knudson 2001). Although

retinoblastoma is rare in adults given retinoblasts stop dividing once they have fully differentiated (Dyer and Bremner 2005), people that have inherited an *RB1* mutation are more susceptible to other types of cancer throughout adulthood (Fletcher et al. 2004). Survivors of retinoblastoma that have been subject to radiation therapy and have inherited a *RB1* mutation have a 51% increased risk of developing a new malignancy by age 50, whereas somatic mutant *RB1* retinoblastoma survivors have a 5.7% increased risk (Kleinerman et al. 2005). Inherited *RB1* mutations and the development of retinoblastoma are rare; however, Rb loss or inactivation is found in most cancers. For example, retinoblastoma occurs in approximately 0.0011% of the population, whereas Rb loss is found in 80% of small cell lung cancers, and Rb inactivation is found in >80% of pancreatic cancer, breast cancer, glioblastoma and mantle cell lymphomas (Sherr and McCormick 2002)(Park et al. 2014). Rb loss refers to the absence of detectable protein in tumor cells, whereas inactivation refers to a highly phosphorylated (hyperphosphorylated) and inactive form of Rb. Genetic experiments in mice show that *RB1* is required for development, where $RB1^{-/-}$ mice die in utero at day 14 (Jacks et al. 1992). In contrast, $RB1^{+/-}$ mice develop adenocarcinoma at 10 months of age only when a second somatic mutation occurs in the second allele (Jacks et al. 1992), which is analogous to the increased risk for cancer in humans that have an *RB1* mutant allele.

At the molecular level, the retinoblastoma protein (Rb) functions as a negative regulator of transcription of cell cycle genes during G_1. There are three Rb paralogs in mammals; p130 (*RBL2*), p107 (*RBL1*) and Rb (*RB1*). All three Rb family members repress cell cycle gene transcription by preventing E2F directed activity (Dick and Rubin 2013a). Out of the three Rb family members, Rb has the highest affinity for the activator E2Fs (E2F1, E2F2 and E2F3) (Liban et al. 2017). Rb can directly bind to the transactivation domain of the activator E2Fs (**Figure 1.2**) and to the marked box domain to suppress E2F activity (Dick and Rubin 2013b). $RB1^{-/-}$ fibroblasts can arrest in the absence of growth factors or contact inhibition however

RB1$^{-/-}$;*RBL1*$^{-/-}$;*RBL2*$^{-/-}$ cells cannot. p130 and p107 have overlapping functions: *RBL1*$^{-/-}$ and *RBL2*$^{-/-}$ mice are viable, whereas *RBL2*$^{-/-}$;*RBL1*$^{-/-}$ pups die at postnatal day 18 (Cobrinik et al. 1996). Although Rb is considered the only bona fide tumor suppressor protein in the family, combined loss of p130 or p107 with Rb accelerates tumor growth in mice. Intriguingly, retinoblastoma only develops in mice that lose both Rb and p107/or p130 (Dannenberg et al. 2004) where p107/p130 levels are thought to be higher in mouse retinoblasts and can suppress tumor growth in the absence of Rb (Wirt and Sage 2010). Moreover, p107 has also been shown to arrest Rb-deficient cells when overexpressed (Jiang et al. 2000). Altogether, this genetic data suggest that p107 and p130 have tumor suppressing capability in certain circumstances. The roles of p130 and p107 in regulating cell cycle dependent genes in in the context of MuvB binding and the DREAM complex during quiescence is described in greater detail in **Chapter 2**. In summary, the Rb family represents important negative regulators of G_0 and G_1 that are inactivated in many cancers.

1.1.3 Cyclin dependent kinase activation and Rb inactivation

Cyclin-dependent kinases (CDK) are a family of serine/threonine kinases that regulate cell cycle progression, transcription, and mitosis. The cell cycle CDKs in mammals are CDK4/6 (G_0/G_1/S), CDK2 (G_1/S/G_2) and CDK1 (G_2/M). An important target of the cell cycle CDKs is the Rb family (Otto and Sicinski 2017). There are 13 phosphorylation sites in Rb, and specific sites have specific outputs (Dick and Rubin 2013b). For example, the release of the transactivation domain of E2F2 from the Rb pocket domain requires phosphorylation at Rb S608 (**Figure 1.2**), whereas Rb phosphorylation at T373 drives an alternative conformational change that blocks the histone deacetylase (HDAC) binding site called the LxCxE cleft (Burke et al. 2012). Paul Nurse found that CDKs are evolutionary conserved kinases required for cell cycle progression and mitosis in eukaryotes. He demonstrated that *cdc2* deficient *S. pombe* that could not progress into mitosis could be rescued with human *CDC2* (CDK1), and that both proteins were active kinases (Lee and

Nurse 1987). In mammals, CDK1 alone is sufficient to complete the cell cycle (Cerqueira et al. 2007). CDKs are only active when complexed with cyclin proteins, which are allosteric activators that drive the formation of the CDK catalytic site (Jeffrey et al. 1995). Specific cyclin isoforms are expressed at the different phases of the cell cycle. In mammals, cyclin D is expressed first (complexes with CDK4/6), followed by cyclin E (CDK2), then A (CDK2/CDK1) and finally B (CDK1) (Malumbres and Barbacid 2009). The waves of cyclin expression and turnover that occur during the cell cycle were first observed in sea urchin extracts by Timothy Hunt in 1983 (Jackson 2008). *CCND1* and *CCNE1* are commonly amplified in human cancers, resulting in high expression of cyclin D and cyclin E and therefore high CDK4/6 and CDK2 activity (Ohshima et al. 2017). Moreover, activation of the Myc, ER or MAPK pathways results in the expression of Cyclin D in cancer. This can occur through amplification of *MYC* or overexpression of *ERBB2* (Ohshima et al. 2017), or through mutations in Ras which result in a constitutively active GTP-bound state (Bryant et al. 2014).

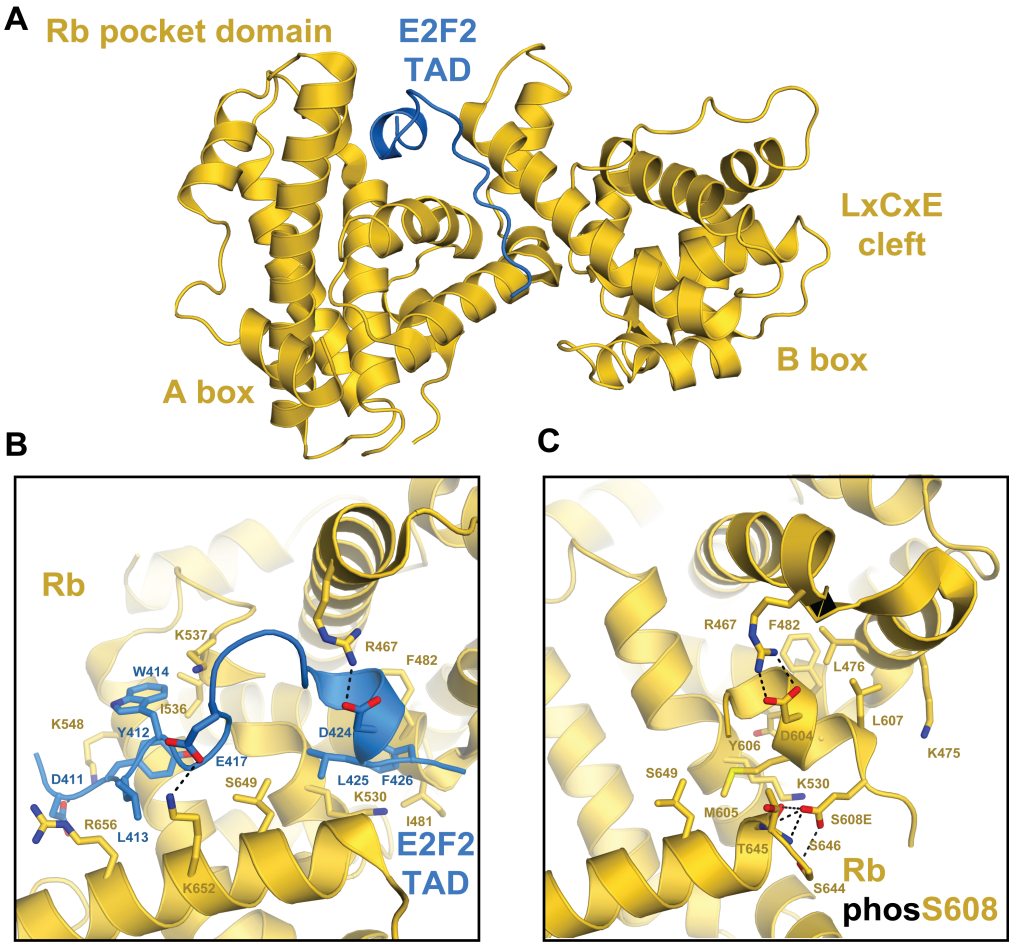

Figure 1.2. The suppression of E2F transactivation is relieved by Rb phosphorylation at S608. (A) Overall structure of E2F2 transactivation domain (TAD, blue) bound to the Rb pocket domain (gold) (PDB ID: 1N4M). The LxCxE cleft is a docking site for viral oncoproteins, which use a CR2 domain that contains an LxCxE sequence motif. (B) The E2F2 TAD L413, W414, L425 and F426 form van der Wals interactions with a hydrophobic cleft formed by the A box and B box of the Rb pocket. Salt bridge interactions are formed between D411, E417 and D424 in E2F2 and K548, K652 and R467 in Rb respectively. (C) (PDB ID: 4ELL) Rb phosphorylation leads to M605, L607 and Y606 forming van der Wals docking into the same hydrobic cleft that E2F2 binds to in Rb. This intramolecular interaction is driven by the S608 phosphorylation (phosphomimetic in the structure), which forms a salt bridge and hydrogen bonding network through the hydroxyls of S644 and S646, and the amide backbone of T645 and S644.

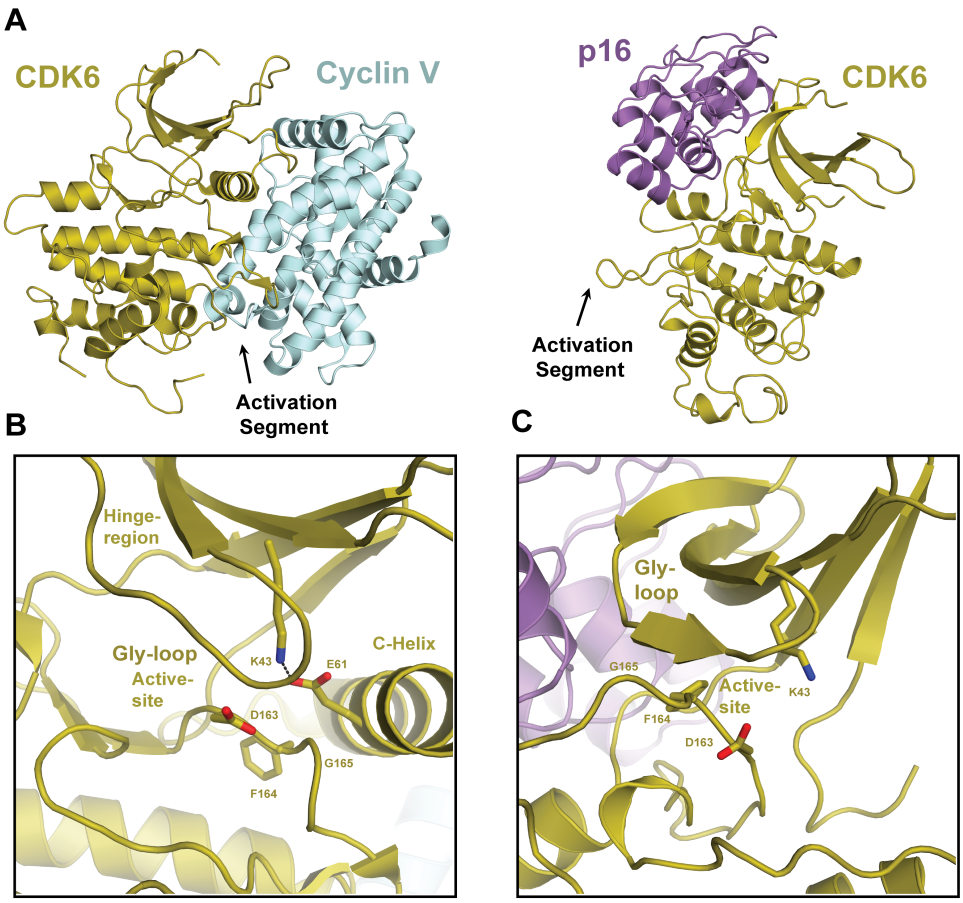

Figure 1.3. p16 is a tumor suppressor protein that inactivates CDK4/6. (A) Overall structure of CDK6-cyclin V (PDB ID: 2EUF) and CDK6-p16 (PDB ID:1BI7). In an active CDK6 complex, the activation segment is positioned below the c-helix, and the cyclin positions the c-helix into the active site. When p16 binds CDK6, the c-helix structure is distorted and the activation segment is pulled away from the cyclin. This blocks ATP binding, substrate binding and weakens cyclin binding, combinatorially leading to kinase inhibition. (B) An active "DFG-in" CDK6 conformation positions D163 for magnesium binding, and F164 below the C-helix allowing E61 to position K43 for catalysis. (C) When p16 binds CDK6, the activation segment rearrangement results in an "DFG-out" conformation, positioning F164 into the nucleotide binding pocket below the Gly-loop. This conformation inhibits kinase activity.

CDK4/6 are specifically inhibited by p16 (*CDKN2A*) (**Figure 1.3**), a tumor suppressor protein that is often deleted in human cancers, with up to 80% deletion in pancreatic cancer (Sherr and McCormick 2002). *CDKN2A* is also commonly silenced through epigenetic methylation in many cancers (Zhao et al. 2016). *CDKN2A*$^{-/-}$ mice develop sarcomas and lymphomas within 6 months of age. p16 plays a role in cell cycle arrest and senescence in response to negative proliferative regulators such as TGFβ signaling, but also in response to excessive oncogene activation such as Ras, Myc, and oncogenic viruses (Gil and Peters 2006)(Munger et al. 2013). When p16 levels accumulate with the age of a cell through Ets1 mediated *CDKN2A* expression (Ohtani et al. 2001), cells enter an irreversible state of arrest called senescence. The age of human fibroblast cells can be estimated directly from p16 levels (Ressler et al. 2006). In the absence of p16 in cancer cells, Rb is readily phosphorylated and inactivated by CDK4/6-cyclin D1 complexes.

1.1.4 Myc and E2F activate S phase genes

When cells receive the appropriate growth signals to divide, they will synthesize a duplicative set of chromosomes that will be incorporated into two daughter cells. This step is known as the synthesis phase, or "S" phase. In order for the DNA replication to occur, a major wave of transcription of cell cycle dependent genes must occur at G_1/S (Liu et al. 2017). The activators of S-phase genes are Myc and E2F1/2/3 (Liu et al. 2015). The regulation of the activator E2F2 is illustrated in **Figure 1.2**. E2F and Myc directed genes include *TYMS*, *RRM2*, and *POLA1* which are enzymes required for dNTP synthesis and polymerization (Pardee et al. 2004)(Lane and Fan 2015). E2F and Myc also promote cyclin D, E, and A expression. Knocking out Myc in cells only partially reduces proliferation, whereas E2F1-3 knockout cells suffer a severely reduced rate of proliferation, and finally combined c-Myc and E2F1-3 knockout cells do not proliferate (Leone et al. 2001)(Chen et al. 2009). As described earlier, the overexpression of Myc is observed in most tumors, whereas E2F overexpression is not (Ohshima et al. 2017). High levels of E2F in cells triggers an

apoptotic response (Poppy Roworth et al. 2015), whereas moderate levels drives progression of the cell cycle where the loss of Rb function is directly correlated with the loss of E2F suppression in cancer. The completion of the synthesis of the genome results in a second growth stage in preparation for division referred to as the second gap phase or G_2. At this stage cells determine whether the genome was properly synthesized, and prepare repair mechanisms or force apoptosis if the damage is irreparable.

1.1.5 p53 and the DNA damage response

The most commonly mutated tumor suppressor gene in all human cancers is *TP53* (Kandoth et al. 2013)(Vogelstein et al. 2010), which encodes for the p53 protein (**Figure 1.1**). While Rb primarily regulates the G_1/S transition, p53 regulates both the G_1/S and G_2/M transitions through the expression of the CDK inhibitor p21 (**Figure 1.5**), which is described in greater detail **Chapter 4**. The discovery of p53 unraveled soon after Rb was first

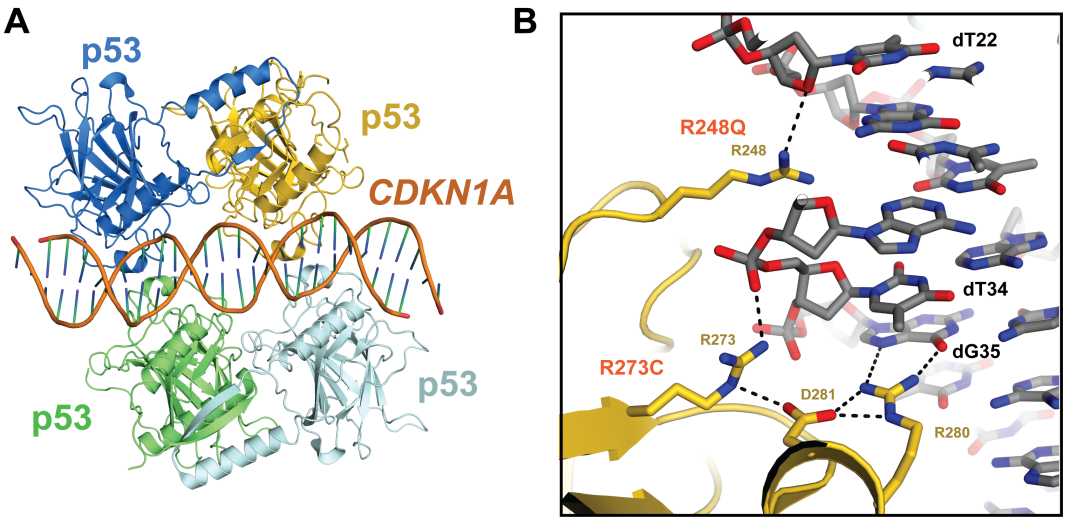

Figure 1.4. The structure of a p53 tetramer bound to *CDKN1A* promoter. (A) An overall view of the DNA-binding and tetramerization domains of p53 forming a tetramer on the *CDKN1A* prompter (PDB ID: 3TS8). (B) R248Q and R273C mutations are the most common mutations in p53 in cancer. In wild-type p53, R248 forms a hydrogen bond with the deoxyribose 4'O of thymidine 22. R273 forms a salt bridge with the phosphate of dT34, and the hydroxyl of D281. This positions D281 to form a hydrogen bond network to position R280 to contact guanosine 35 carbonyl. A R248Q or R273C mutation would disrupt p53's DNA-binding function.

described, although p53 was originally thought to be an oncogene. The expression of p53 was elevated in response to SV40 large-T-antigen infection, and therefore it was thought to be a downstream effector of the oncogenic virus (Linzer and Levine 1979). The theory of p53 as a tumor suppressor was solidified after *TP53* was found to be mutated in tumor samples from families affected by Li-Fraumini syndrome, a genetic disorder that increases the risk of tumorigenesis by 50% for a wide-spectrum of malignancies by age 30 (Malkin et al. 1990). The role of p53 in the cell is to stop division when DNA is damaged to allow for repair, but also to trigger cell death if the damage is excessive. In response to DNA damage or replicative stress, p53 activates *CDKN1A* (p21), which directly inhibits CDK activity and allows the Rb family to arrest the cell cycle (**Figure 1.5**). Mutations in *TP53* in cancer are commonly found within the DNA binding domain, leading to inactivation of the *CDKN1A* response (**Fig 1.4**) (Kastenhuber and Lowe 2017). Mice that maintain one copy of p53 with a DNA binding mutation R248W ($TP53^{R248W/-}$) are equally susceptible to tumorigenesis as $TP53^{-/-}$ mice (Donehower et al. 1992)(Tyner 2002). Moreover, $CDKN1A^{-/-}$ mice are highly susceptible to tumors, but only when exposed to ionizing radiation (Martı et al. 2001) highlighting the importance of the p53-p21 network in tumor suppression through the DNA damage response. In combination with cell cycle arrest, p53 can also activate DNA repair genes such as *DDB2,* or pro-apoptotic genes such as *BAX* and *BBC3* when the genomic damage is beyond repair (Fischer 2017). The threshold of DNA damage for which p53 triggers apoptosis is still debated (Kastenhuber and Lowe 2017), however higher levels of p53 are associated with the apoptotic response whereas low levels lead to cell cycle arrest (Jiang et al. 2010). The second most occupied promoter by p53 after *CDKN1A* in response to DNA damage is *MDM2* (Fischer et al. 2014). MDM2 is a p53 E3 ligase that polyubiquitinates p53 resulting in proteosomal degradation. The activation of *MDM2* by p53 enables a negative feedback loop to keep p53 levels down if the DNA damage is repairable. However if the DNA damage is beyond repair, excessive p53 levels will lead to the apoptotic

response. *MDM2* $^{-/-}$ mice display excessive p53 levels and are embryonic lethal day 5.5 (Luna et al. 1995). When p53 is deleted in these mice (*MDM2* $^{-/-}$, *TP53* $^{-/-}$) they are viable, again supporting that overexpression of p53 triggers an apoptotic response and that p53 is the major target of MDM2. The role of p21 in inhibiting CDK4 is described in greater detail in **Chapter 4**.

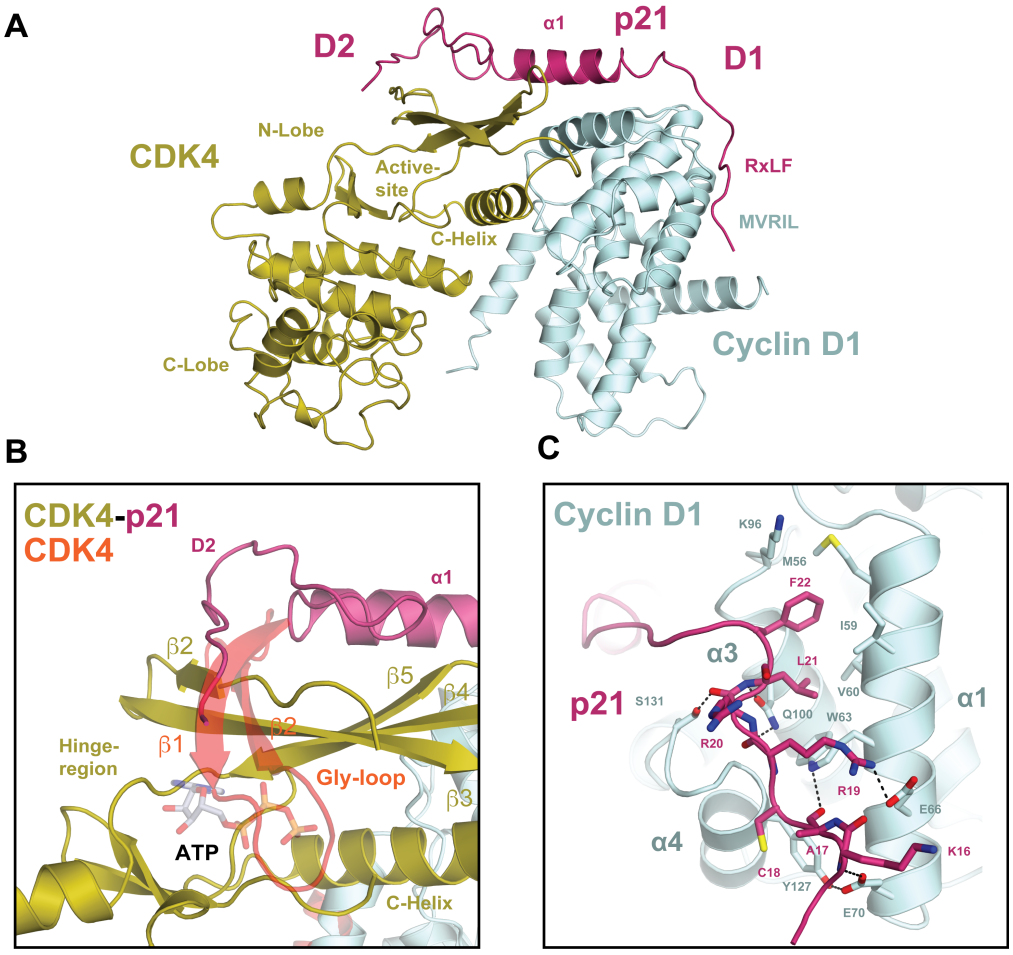

Figure 1.5. The p53 effector protein p21 binds to and inactivates CDK4. (A) Overall structure of p21 (magenta) bound to CDK4 (gold) and cyclin D1 (cyan). (B) p21 D2 domain pulls the Gly-loop out of the CDK4 active site inhibiting ATP binding. The Gly-loop is required for stabilizing the phosphates in ATP. (C) Substrates recognized by CDK4 maintain an RxL motif downstream of their serine/threonine phosphorylation site that binds to the MVRIL site on α1 of cyclin D1. p21 uses an RxLF motif to block substrate binding to cyclin D1. p21 R19 forms a salt bridge interaction with E66 on cyclin D1. L2 and F22 form van der Wals interactions with K96, M56, I59, V60 and W63 on cyclin D1.

1.1.6 B-Myb and FoxM1 activate G_2/M genes

During late S phase, a second set of cell cycle dependent genes are transcribed to prepare for mitosis. The activators of mitotic genes are B-Myb and FoxM1 (Sadasivam and DeCaprio 2013). B-Myb first associates with the chromatin complex MuvB during S phase to

initiate transcription, and FoxM1 is subsequently recruited in late S phase to achieve maximum transcriptional activation (Sadasivam et al. 2012). Knocking out either *MYBL2* or *FOXM1* in mice is embryonic lethal due to low levels of kinesins, polo-like-kinase, auora kinase, and mad2, which are key motor components of spindle assembly and cytokinesis (Tanaka et al. 1999)(Krupczak-Hollis et al. 2004). Additionally, B-Myb and FoxM1 activate transcription of cyclins to maintain sustained proliferative signaling. Overexpression of the Myb and Forkhead box protein families is correlated with poor prognosis in breast, lung and colon cancers (Myatt and Lam 2007; Musa et al. 2017). The role of B-Myb in the cell cycle and its role in MuvB function is described in greater detail in **Chapter 3**.

1.1.7 Mitosis and translocations in cancer

The final stage of the cell cycle is mitosis. This process involves the condensation and arrangement of chromosomes to be properly separated into two daughter cells through cytokinesis (Cooper 2000). Walther Flemming was the first to provide a cohesive description of mitosis in 1874 through the staining of chromosomes ("colored bodies") using the dyes haematoxylin and haematein (Paweletz 2001). Following Flemming's observations, Theodor Boveri hypothesized in 1914 that rearrangements of chromosomes during cell division is the source of tumor transformation (Hardy and Zacharias 2005). Peter Nowell proved Boveri's hypothesis to be correct when he identified the Philadelphia chromosome in 1960 (Koretzky 2007). Nowell found that reciprocal translocation of chromosomes 9 and 22 created a fusion gene, *BCR-ABL*, that is a driver of chronic myeloid leukemia (CML). The Bcr-Abl fusion converts Abl into a constitutively activated tyrosine kinase that can phosphorylate p21 and p27 switching their function from inhibitors of CDKs to activators (Hukkelhoven et al. 2012)(Chu et al. 2007)(James et al. 2008). This results in loss of the p53-p21 response as well as inactivation of Rb through non-inhibited CDK4/6 and CDK2. The activity of Bcr-Abl has also been linked to activation of Myc (Cilloni and Saglio 2012). Fusions of cell-cycle transcription factors have since been discovered, such as *MYB-NFIB* and *MYBL1-NFIB*

(Medsker et al. 2016) in adenoid cystic carcinoma (ACC). The Myb-NFIB fusion protein is a de-repressed transcriptional activator of mitotic genes. The role of Abl activated p21 and p27 in CDK4 regulation is described in greater detail in **Chapter 4**.

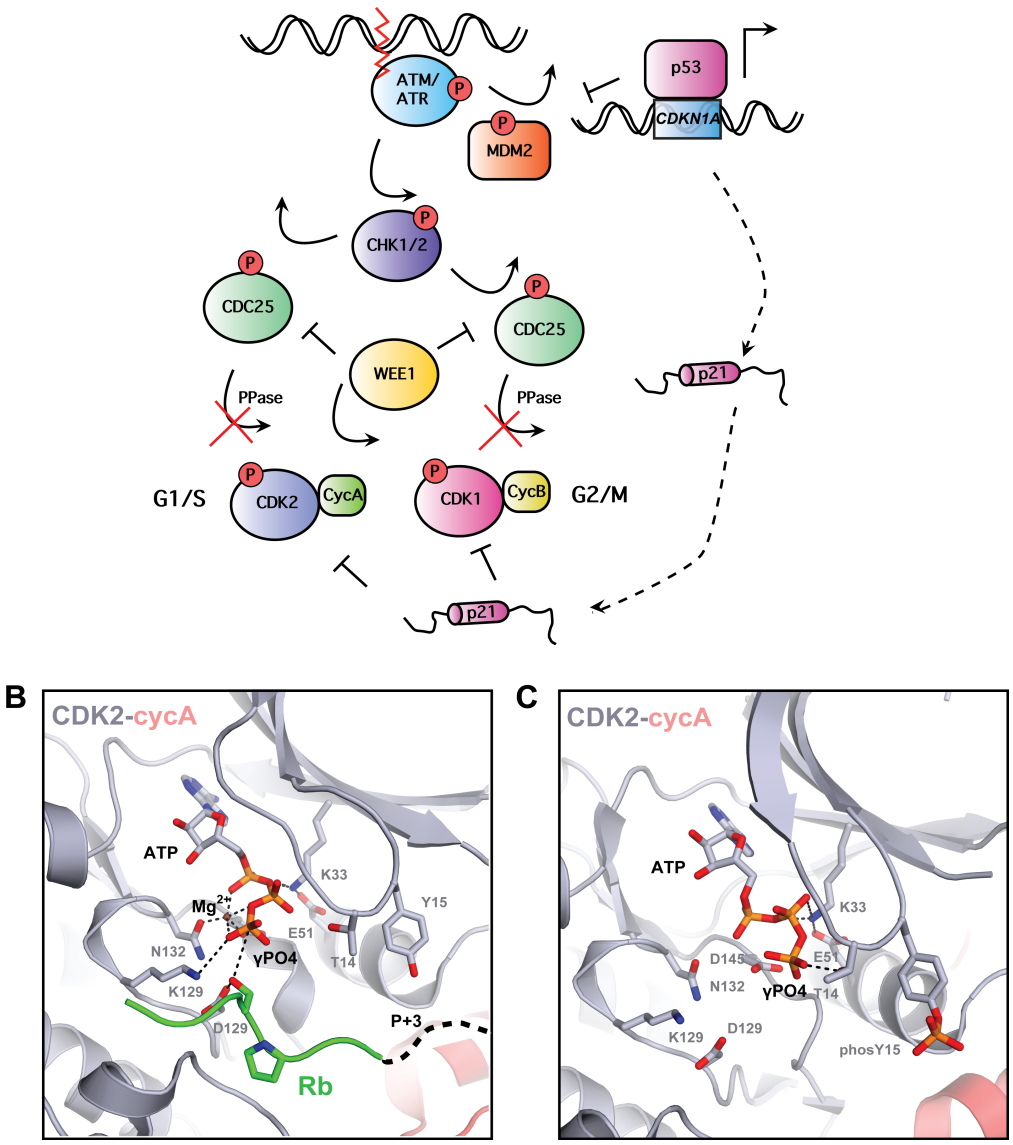

Figure 1.6. The DNA damage response results in sustained tyrosine phosphorylation and inhibition of CDK2/CDK1. (A) ATM or ATR kinases are activated in response to DNA damage. Once activated ATM/ATR phosphorylate and inactivate MDM2, resulting in stability of p53 levels. ATM/ATR also activate CHK1/2, which in turn phosphorylate and inactivate CDC25 phosphatase. With CDC25 inactivated, the tyrosine phosphorylation of CDK2 and CDK1 by Wee1 is stabilized and the cells are arrested. (B) (PDB ID: 1QMZ) Active CDK2-cyclin A2 complex coordinates ATP and a consensus SPxxK CDK substrate for phosphotransfer. (C) (PDB ID: 2CJM) When tyrosine Y15 is phosphorylated by Wee1, the Gly-loop conformation changes where T14 forms a hydrogen bound with the gamma-phosphate of ATP, pulling it away from the substrate serine and inhibiting phosphorylation. The phosY15 also sterically clashes with the substrate P+3 residue, leading to inhibition of substrate binding. Dephosphorylation of Y15 by CDC25 is required to restore activity of the kinase.

1.1.8 Conclusions

Altogether, the loss of cell cycle control through p53 and pRb inactivation represents an unsolved problem in the cancer biology field. There are currently no FDA approved inhibitors that restore wild-type p53 activity in cancer cells. There is however an ongoing phase III clinical trail (ClinicalTrials.gov Identifier: NCT02545283) for an MDM2 inhibitor, Idasanutlin (Ding et al. 2013), for the treatment of acute myeloid leukemia. The mechanism of action of the drug is to inhibit the p53 transactivation domain interaction with MDM2 (ElSawy et al. 2013). There are however skeptics of an MDM2-p53 inhibitor that address concerns involving the response of wild-type p53 to the drug (Lowe 2013). The majority of cancers have p53 DNA binding mutations that cannot activate *CDKN1A* and therefore the stabilization of a mutant p53 by blocking MDM2 would have no effect. This stabilization may also lead to apoptosis in healthy cells that maintain wide-type p53, which was observed in the *MDM2* knockout mouse (Luna et al. 1995). However, the drug could prove useful in the subset of cancers with MDM2 overexpression through *MDM2* amplification such as sarcomas and melanoma (Ohshima et al. 2017).

Strategies for restoring Rb function through therapeutics have evolved over the last few decades through the improvement of selectivity with CDK inhibitors. The FDA approval of third generation CDK4/6 specific ATP inhibitors (palbociclib, ribociclib and abemaciclib) for ER-positive HER2-negative breast cancer has led to an explosion of clinical trials using CDK4/6 inhibitors to target many types of cancer (Sherr et al. 2016). There are also efforts in motion to develop CDK2 specific inhibitors (Anscombe et al. 2015). The concept of targeting CDKs in cancer existed decades ago, however the first and second generation of inhibitors (roscovitine, flavinol and dinaciclib) targeted most members of the CDK family, and therefore inhibited physiological pathways outside of cell cycle regulation. As a result, these pan-CDK inhibitors affected CDK9 transcription associated kinase, which led to cellular cytotoxicity (Otto and Sicinski 2017). The targeting of CDK4/6 works well in Rb-positive cells, however

when Rb is lost there is no alternative. In addition, a common resistance mechanism is the activation of CDK2 through amplification of *CCNE1*, which drives the formation of active CDK2-cyclin E complexes and are not inhibited by CDK4/6 inhibitors (Herrera-abreu et al. 2016)(Ohshima et al. 2017).

In this dissertation, I describe the mechanism of DREAM and Myb-MuvB assembly in **Chapters 2 and 3**. Targeting Myb-MuvB to restore DREAM complex suppression of cell cycle dependent genes could be a viable strategy in cancers that become resistant to CDK4/6 inhibitors or in tumors that have lost Rb. In **Chapter 4** I describe how phosphorylated p27 and p21 allosterically activate CDK4, and confer resistance to CDK4/6 inhibitors. The development of CDK4-cyclin D-p27/p21 inhibitors could prove useful in cancers that have high tyrosine kinase activity and p27/p21 expression. Alternatively, targeting tyrosine kinases in combination with CDK4/6 could prevent p27/p21 phosphorylation and CDK4/6-cyclin D dimer activity.

1.2 References

Anscombe E, Meschini E, Mora-Vidal R, Martin MP, Staunton D, Geitmann M, Danielson UH, Stanley WA, Wang LZ, Reuillon T, et al. 2015. Identification and Characterization of an Irreversible Inhibitor of CDK2. *Chem Biol* **22**: 1159–1164. http://dx.doi.org/10.1016/j.chembiol.2015.07.018.

Bryant KL, Mancias JD, Kimmelman AC, Der CJ. 2014. KRAS: Feeding pancreatic cancer proliferation. *Trends Biochem Sci* **39**: 91–100. http://dx.doi.org/10.1016/j.tibs.2013.12.004.

Burke JR, Hura GL, Rubin SM. 2012. Structures of inactive retinoblastoma protein reveal multiple mechanisms for cell cycle control. 1156–1166.

Cerqueira A, Hunt S, Tardy C, Newton K, Santamarı D, Dubus P, Malumbres M, Barbacid M, Ca JF. 2007. Cdk1 is sufficient to drive the mammalian cell cycle. **448**: 811–816.

Chen D, Pacal M, Wenzel P, Knoepfler PS, Leone G, Bremner R. 2009. Division and apoptosis of E2f-deficient retinal progenitors. *Nature* **462**: 925–929. http://dx.doi.org/10.1038/nature08544.

Chu I, Sun J, Arnaout A, Kahn H, Hanna W, Narod S, Sun P, Tan CK, Hengst L, Slingerland J. 2007. p27 Phosphorylation by Src Regulates Inhibition of Cyclin E-Cdk2. *Cell* **128**: 281–294.

Cilloni D, Saglio G. 2012. Molecular pathways: BCR-ABL. *Clin Cancer Res* **18**: 930–937.

Cobrinik D, Lee MH, Hannon G, Lee DCM, Hannon G, Mulligan G, Bronson RT, Dyson N, Harlow E, Beach D, et al. 1996. Shared role of the pRB-related pl30 and pi07 proteins in limb development. 1633–1644.

Cooper G. 2000. *The Cell: A Molecular Approach*. 2nd ed.

Dannenberg JH, Schuijff L, Dekker M, Van Der Valk M, Te Riele H. 2004. Tissue-specific tumor suppressor activity of retinoblastoma gene homologs p107 and p130. *Genes Dev* **18**: 2952–2962.

Dawson MA. 2017. The cancer epigenome: Concepts, challenges, and therapeutic opportunities. *Science (80-)* **1**: 379–385. http://science.sciencemag.org/content/355/6330/1147/tab-pdf.

Deniz Ö, Flores O, Aldea M, Soler-López M, Orozco M. 2016. Nucleosome architecture throughout the cell cycle. *Sci Rep* **6**: 1–11. http://dx.doi.org/10.1038/srep19729.

Dick F a, Rubin SM. 2013a. Molecular mechanisms underlying RB protein function. *Nat Rev Mol Cell Biol* **14**: 297–306. http://www.ncbi.nlm.nih.gov/pubmed/23594950 (Accessed August 15, 2013).

Dick FA, Rubin SM. 2013b. Molecular mechanisms underlying RB protein function. *Nat Rev Mol Cell Biol* **14**: 297–306. http://dx.doi.org/10.1038/nrm3567.

Ding Q, Zhang Z, Liu JJ, Jiang N, Zhang J, Ross TM, Chu XJ, Bartkovitz D, Podlaski F, Janson C, et al. 2013. Discovery of RG7388, a potent and selective p53-MDM2 inhibitor in clinical development. *J Med Chem* **56**: 5979–5983.

Donehower LA, Harvey M, Slagle BL, McArthur MJ, Montgomery CA, Butel JS, Bradley A. 1992. Mice deficient for p53 are developmentally normal but susceptible to spontaneous tumours. *Nature* **356**: 215–221. http://www.nature.com/doifinder/10.1038/356215a0.

ElSawy KM, Verma CS, Joseph TL, Lane DP, Twarock R, Caves LSD. 2013. On the interaction mechanisms of a p53 peptide and nutlin with the MDM2 and MDMX proteins: A Brownian dynamics study. *Cell Cycle* **12**: 394–404.

Fischer M. 2017. Census and evaluation of p53 target genes. *Oncogene* **36**: 3943–3956. http://dx.doi.org/10.1038/onc.2016.502.

Fischer M, Steiner L, Engeland K. 2014. The transcription factor p53: Not a repressor, solely an activator. *Cell Cycle* **13**: 3037–3058.

Fletcher O, Easton D, Anderson K, Gilham C, Jay M, Peto J. 2004. Lifetime risks of common cancers among retinoblastoma survivors. *J Natl Cancer Inst* **96**: 357–363.

Foster DA, Yellen P, Xu L, Saqcena M. 2011. Regulation of G1 cell cycle progression: Distinguishing the restriction point from a nutrient-sensing cell growth checkpoint(s). *Genes and Cancer* **1**: 1124–1131.

Gil J, Peters G. 2006. Regulation of the INK4b-ARF-INK4a tumour suppressor locus: All for

one or one for all. *Nat Rev Mol Cell Biol* **7**: 667–677.

Goetsch PD, Garrigues JM, Strome S. 2017. Loss of the Caenorhabditis elegans pocket protein LIN-35 reveals MuvB's innate function as the repressor of DREAM target genes. *PLoS Genet* **13**: 1–25.

Guiley KZ, Liban T, Felthousen J, Ramanan P, Litovchick L, Rubin SM. 2015. Structural mechanisms of DREAM complex assembly and regulation. *Genes Dev* **120**: 1–9.

Hanahan D, Weinberg RA. 2000. The hallmarks of cancer. *Cell* **100**: 57–70. http://www.ncbi.nlm.nih.gov/pubmed/10647931.

Hanahan D, Weinberg R a. 2011. Hallmarks of cancer: The next generation. *Cell* **144**: 646–674. http://dx.doi.org/10.1016/j.cell.2011.02.013.

Hardy PA, Zacharias H. 2005. Reappraisal of the Hansemann e Boveri hypothesis on the origin of tumors. **29**.

Herrera-abreu MT, Palafox M, Asghar U, Rivas MA, Cutts RJ, Garcia-murillas I, Pearson A, Guzman M, Elliott R, Rodriguez O, et al. 2016. Early Adaptation and Acquired Resistance to CDK4 / 6 Inhibition in Estrogen Receptor – Positive Breast Cancer.

Hukkelhoven E, Liu Y, Yehs N, Ciznadijas D, Blain SW, Koffs A. 2012. Tyrosine phosphorylation of the p21 cyclin-dependent kinase inhibitor facilitates the development of proneural glioma. *J Biol Chem* **287**: 38523–38530.

Jacks T, Fazeli A, Schmitt EM, Bronson RT, Goodell MA, Weinberg RA. 1992. Effects of an Rb mutation in the mouse. *Nature* **359**: 295–300.

Jackson PK. 2008. BenchMarks The Hunt for Cyclin. 199–202.

James MK, Ray A, Leznova D, Blain SW. 2008. Differential modification of p27Kip1 controls its cyclin D-cdk4 inhibitory activity. *Mol Cell Biol* **28**: 498–510.

Jeffrey P, Russo A, Polyak K, Gibbs E. 1995. Mechanism of CDK activation revealed by the structure of a cyclinA-CDK2 complex. *Nature*. http://www.chem.uwec.edu/Webpapers2005/twarosed/sources/1FIN_journal.pdf (Accessed June 24, 2014).

Jiang H, Karnezis AN, Tao M, Guida PM, Zhu L. 2000. pRB and p107 have distinct effects when expressed in pRB-deficient tumor cells at physiologically relevant levels. *Oncogene* **19**: 3878–87. http://www.ncbi.nlm.nih.gov/pubmed/10951581.

Jiang L, Sheikh MS, Huang Y. 2010. Decision Making by p53: Life versus Death. *Mol Cell Pharmacol* **2**: 69–77. http://www.pubmedcentral.nih.gov/articlerender.fcgi?artid=2877278&tool=pmcentrez&rendertype=abstract.

Kandoth C, Mclellan MD, Vandin F, Ye K, Niu B, Lu C, Xie M, Zhang Q, Mcmichael JF, Wyczalkowski MA, et al. 2013. Mutational landscape and significance across 12 major cancer types. *Nature* **502**: 333–339.

Kastenhuber ER, Lowe SW. 2017. Putting p53 in Context. *Cell* **170**: 1062–1078. http://dx.doi.org/10.1016/j.cell.2017.08.028.

Kleinerman RA, Tucker MA, Tarone RE, Abramson DH, Seddon JM, Stovall M, Li FP, Fraumeni JF. 2005. Risk of new cancers after radiotherapy in long-term survivors of retinoblastoma: An extended follow-up. *J Clin Oncol* **23**: 2272–2279.

Knudson a G. 2001. Two genetic hits (more or less) to cancer. *Nat Rev Cancer* **1**: 157–162.

Knudson AG. 1971. Mutation and Cancer : Statistical Study of Retinoblastoma. **68**: 820–823.

Koretzky G a. 2007. Review series introduction The legacy of the Philadelphia chromosome. *J Clin Invest* **117**: 2030–2032.

Krupczak-Hollis K, Wang X, Kalinichenko V V., Gusarova GA, Wang IC, Dennewitz MB, Yoder HM, Kiyokawa H, Kaestner KH, Costa RH. 2004. The mouse Forkhead Box m1 transcription factor is essential for hepatoblast mitosis and development of intrahepatic bile ducts and vessels during liver morphogenesis. *Dev Biol* **276**: 74–88.

Lane AN, Fan TWM. 2015. Regulation of mammalian nucleotide metabolism and biosynthesis. *Nucleic Acids Res* **43**: 2466–2485.

Lane S, Farlie P, Watson R. 1997. B-Myb function can be markedly enhanced by cyclin A-dependent kinase and protein truncation.

Lee MG, Nurse P. 1987. Complementation used to clone a human homologue of the fission yeast cell cycle control gene cdc2. *Nature* **327**: 31–5.

Lee W, Tillo D, Bray N, Morse RH, Davis RW, Hughes TR, Nislow C. 2007. A high-resolution atlas of nucleosome occupancy in yeast. *Nat Genet* **39**: 1235–1244.

Leone G, Sears R, Huang E, Rempel R, Nuckolls F, Park CH, Giangrande P, Wu L, Saavedra HI, Field SJ, et al. 2001. Myc requires distinct E2F activities to induce S phase and apoptosis. *Mol Cell* **8**: 105–113.

Liban TJ, Medina EM, Tripathi S, Sengupta S, Henry RW, Buchler NE. 2017. Conservation and divergence of C-terminal domain structure in the retinoblastoma protein family.

Linzer DIH, Levine AJ. 1979. Characterization of a 54K Dalton cellular SV40 tumor antigen present in SV40-transformed cells and uninfected embryonal carcinoma cells. *Cell* **17**: 43–52.

Litovchick L, Sadasivam S, Florens L, et al. 2007. Evolutionarily Conserved Multisubunit RBL2/p130 and E2F4 Protein Complex Represses Human Cell Cycle-Dependent Genes in Quiescence. *Mol Cell* **3**: 539–551. http://www.sciencedirect.com/science/article/pii/S1097276507002511 (Accessed October 29, 2013).

Liu H, Tang X, Srivastava A, Pécot T, Daniel P, Hemmelgarn B, Reyes S, Fackler N, Bajwa A, Kladney R, et al. 2015. Redeployment of Myc and E2f1 – 3 drives Rb -deficient cell cycles. **17**.

Liu Y, Chen S, Wang S, Soares F, Fischer M, Meng F, Du Z, Lin C, Meyer C, DeCaprio JA, et al. 2017. Transcriptional landscape of the human cell cycle. *Proc Natl Acad Sci* **114**: 3473–3478. http://www.pnas.org/lookup/doi/10.1073/pnas.1617636114.

Lloyd AC. 2013. XThe regulation of cell size. *Cell* **154**: 1194–1205. http://dx.doi.org/10.1016/j.cell.2013.08.053.

Lowary PT, Widom J. 1998. New DNA sequence rules for high affinity binding to histone octamer and sequence-directed nucleosome positioning. *J Mol Biol* **276**: 19–42.

Lowe D. 2013. Overselling p53 Drugs. http://blogs.sciencemag.org/pipeline/archives/2013/01/03/overselling_p53_drugs.

Luger K, Mäder AW, Richmond RK, Sargent DF, Richmond TJ. 1997. Crystal structure of the nucleosome core particle at 2.8 Å resolution. *Nature* **389**: 251–260.

Luna RM de O, Wagner DS, Lozano G. 1995. Rescue of early embroyonic lethality in mdm2-deficient mice by deletion of p53. *Nature*.

Malkin D, Li F, Strong L, Fraumeni J, Nelson C, Kim D, Kassel J, Gryka M, Bischoff F, Tainsky M, et al. 1990. Germ line p53 mutations in a familial syndrome of breast cancer, sarcomas, and other neoplasms. *Science (80-)* **250**: 1233–1238. http://www.sciencemag.org/cgi/doi/10.1126/science.1978757.

Malumbres M, Barbacid M. 2009. Cell cycle, CDKs and cancer: A changing paradigm. *Nat Rev Cancer* **9**: 153–166.

Marceau AH, Felthousen JG, Goetsch PD, Iness AN, Lee H-W, Tripathi SM, Strome S, Litovchick L, Rubin SM. 2016. Structural basis for LIN54 recognition of CHR elements in cell cycle-regulated promoters. *Nat Commun* **7**: 12301. http://www.nature.com/doifinder/10.1038/ncomms12301.

Martı J, Flores JM, Garcı P, Serrano M. 2001. Tumor Susceptibility of p21 Waf1 / Cip1 - deficient Mice 1. 6234–6238.

Medsker B, Forno E, Simhan H, Juan C, Sciences R. 2016. An oncogenic MYB feedback loop drives alternate cell fates in adenoid cystic carcinoma. *Nat Genet* **70**: 773–779.

Mesri EA, Feitelson MA, Munger K. 2014. Human viral oncogenesis: A cancer hallmarks analysis. *Cell Host Microbe* **15**: 266–282. http://dx.doi.org/10.1016/j.chom.2014.02.011.
Munger K, Gwin TK, Mclaughlin-drubin M. 2013. p16 in HPV-associated cancers. **4**.

Musa J, Aynaud M-M, Mirabeau O, Delattre O, Grünewald TG. 2017. MYBL2 (B-Myb): a central regulator of cell proliferation, cell survival and differentiation involved in tumorigenesis. *Cell Death Dis* **8**: e2895. http://www.nature.com/doifinder/10.1038/cddis.2017.244.

Myatt SS, Lam EW-F-F. 2007. The emerging roles of forkhead box (Fox) proteins in cancer. *Nat Rev Cancer* **7**: 847–59. http://www.nature.com/doifinder/10.1038/nrc2223%0Ahttp://dx.doi.org/10.1038/nrc2223.

Ohshima K, Hatakeyama K, Nagashima T, Watanabe Y, Kanto K, Doi Y, Ide T, Shimoda Y,

Tanabe T, Ohnami S, et al. 2017. Integrated analysis of gene expression and copy number identified potential cancer driver genes with amplification-dependent overexpression in 1,454 solid tumors. *Sci Rep* **7**: 1–13. http://dx.doi.org/10.1038/s41598-017-00219-3.

Ohtani N, Zebedee Z, Huot TJG, Stinson JA, Sugimoto M, Ohashi Y, Sharrocks AD, Peters G, Hara E. 2001. Opposing effects of Ets and Id proteins on p16INK4a expression during cellular senescence. *Nature* **409**: 1067–1070. http://www.nature.com/doifinder/10.1038/35059131.

Otto T, Sicinski P. 2017. Cell cycle proteins as promising targets in cancer therapy. *Nat Rev Cancer* **17**: 93–115. http://dx.doi.org/10.1038/nrc.2016.138.

Pardee AB, Li CJ, Reddy GPV, Kaelin WG, Ann B. 2004. Concepts nd es Bio sci en Do No t D ist r. 1091–1094.

Park SJ, Woo SJ, Park KH. 2014. Incidence of retinoblastoma and survival rate of retinoblastoma patients in Korea using the Korean National Cancer Registry Database (1993-2010). *Investig Ophthalmol Vis Sci* **55**: 2816–2821.

Paweletz N. 2001. Walther Flemming : pioneer of mitosis research. **2**: 72–75.

Poppy Roworth A, Ghari F, La Thangue NB. 2015. To live or let die – complexity within the E2F1 pathway. *Mol Cell Oncol* **2**: e970480. https://www.tandfonline.com/doi/full/10.4161/23723548.2014.970480.

Ressler S, Bartkova J, Niederegger H, Bartek J, Scharffetter-Kochanek K, Jansen-Dürr P, Wlaschek M. 2006. p16INK4A is a robust in vivo biomarker of cellular aging in human skin. *Aging Cell* **5**: 379–389.

Russo AA, Jeffrey PD, Patten AK, Massagué J, Pavletich NP. 1996. Crystal structure of the p27(Kip1) cyclin-dependent-kinase inhibitor bound to the cyclin A-Cdk2 complex. *Nature* **382**: 325–331.

Sadasivam S, DeCaprio JA. 2013. The DREAM complex: Master coordinator of cell cycle-dependent gene expression. *Nat Rev Cancer* **13**: 585–595.

Sadasivam S, Duan S, DeCaprio JA. 2012. The MuvB complex sequentially recruits B-Myb and FoxM1 to promote mitotic gene expression. *Genes Dev* **26**: 474–489.

Saville MK, Watson RJ. 1998. The cell-cycle regulated transcription factor B-Myb is phosphorylated by cyclin A/Cdk2 at sites that enhance its transactivation properties. *Oncogene* **17**: 2679–2689.

Schmitges FW, Prusty AB, Faty M, Stützer A, Lingaraju GM, Aiwazian J, Sack R, Hess D, Li L, Zhou S, et al. 2011. Histone Methylation by PRC2 Is Inhibited by Active Chromatin Marks. *Mol Cell* **42**: 330–341.

Schubert S, Horstmann S, Bartusel T, Klempnauer KH. 2004. The cooperation of B-Myb with the coactivator p300 is orchestrated by cyclins A and D1. *Oncogene* **23**: 1392–1404. http://www.ncbi.nlm.nih.gov/entrez/query.fcgi?cmd=Retrieve&db=PubMed&dopt=Citation&list_uids=14973551.

Sherr CJ, Beach D, Shapiro GI. 2016. Targeting CDK4 and CDK6: From discovery to therapy. *Cancer Discov* **6**: 353–367.

Sherr CJ, McCormick F. 2002. The RB and p53 pathways in cancer. *Cancer Cell* **2**: 103–112.

Soares LM, He PC, Chun Y, Suh H, Kim TS, Buratowski S. 2017. Determinants of Histone H3K4 Methylation Patterns. *Mol Cell* **68**: 773–785.e6. https://doi.org/10.1016/j.molcel.2017.10.013.

Tanaka Y, Patestos NP, Maekawa T, Ishii S. 1999. B-myb is required for inner cell mass formation at an early stage of development. *J Biol Chem* **274**: 28067–28070.

Tyner SD. 2002. P53 Mutant Mice That Display Early Aging-Associated Phenotypes. *Nature* **415**: 45–53. http://dx.doi.org/10.1038/415045a.

Vogelstein BB, Hughes MDH, Kimmel S, Cancer C. 2010. p53 : The Most Frequently Altered Gene in Human Cancers. 1–6.

Wang J, Jia ST, Jia S. 2016. New Insights into the Regulation of Heterochromatin. *Trends Genet* **32**: 284–294. http://dx.doi.org/10.1016/j.tig.2016.02.005.

Wirt SE, Sage J. 2010. P107 in the public eye: An Rb understudy and more. *Cell Div* **5**: 1–13.

Yuan G, Liu Y, Dion MF, Slack MD, Wu LF, Altschuler SJ, Oliver J. 2005. Genome-Scale Identification of Nucleosome Positions in S . Cerevisiae. 626–631.

Zetterberg A, Larsson O, Wiman KG. 1995. What is the restriction point? *Curr Opin Cell Biol* **7**: 835–842.

Zhang Q, Vo N, Goodman RH. 2000. Histone binding protein RbAp48 interacts with a complex of CREB binding protein and phosphorylated CREB. *Mol Cell Biol* **20**: 4970–8. http://www.pubmedcentral.nih.gov/articlerender.fcgi?artid=85947&tool=pmcentrez&rendertype=abstract.

Zhao R, Choi BY, Lee MH, Bode AM, Dong Z. 2016. Implications of Genetic and Epigenetic Alterations of CDKN2A (p16INK4a) in Cancer. *EBioMedicine* **8**: 30–39. http://dx.doi.org/10.1016/j.ebiom.2016.04.017.

Chapter 2: Structural Mechanisms of DREAM Complex Assembly and Regulation

2.1 Introduction

Cell cycle exit is a critical process for differentiation and tumor prevention, and cancer cells often have lesions in pathways that control temporary (quiescence) or permanent (senescence) exit. Understanding fundamental mechanisms of cell cycle exit is critical for understanding development and for ultimately designing therapeutic strategies that manipulate exit pathways for halting tumor proliferation. Quiescence has recently been shown to be dependent on the highly conserved protein complex known as DREAM (Litovchick et al. 2007; Litovchick et al. 2011; Sadasivam and DeCaprio 2013). Genetics experiments in model organisms reveal an essential role for DREAM components in differentiation, cell proliferation, and tumor suppression (Korenjak et al. 2004; Lewis et al. 2004; Harrison et al. 2006; Litovchick et al. 2007; van den Heuvel and Dyson 2008; Reichert et al. 2010). DREAM deficient mice die shortly after birth with bone developmental defects that result from aberrant chondrocyte differentiation (Forristal et al. 2014). In human cell culture, DREAM is assembled upon serum starvation in an experimental state of quiescence, and disruption of the DREAM complex drives cells back into the cell cycle despite environmental cues to arrest (Pilkinton et al. 2007; Schmit et al. 2007; Litovchick et al. 2011).

Chromatin immunoprecipitation (ChIP) has located DREAM proteins at a majority of E2F and cell cycle homology regions (CHR) promoters in human cells, and gene expression analysis has implicated DREAM as a repressor of cell cycle genes (Litovchick et al. 2007; Schmit et al. 2007; Muller et al. 2012). The mechanism of how DREAM regulates transcription has not been elucidated, but it is clear that its central components scaffold a number of key cell cycle transcription factors including E2F4/5, B-Myb, FoxM1, and the Rb tumor suppressor family paralogs p107 and p130 (Korenjak et al. 2004; Lewis et al. 2004; Litovchick et al. 2007; Schmit et al. 2007; Sadasivam et al. 2012). DREAM was originally isolated through biochemical purification in flies and worms, and in each case the complex

contained multi-vulval class B protein homologs LIN9, LIN37, LIN52, LIN54, and RBAP48 (mammalian protein names), which together are called the MuvB subcomplex (Korenjak et al. 2004; Lewis et al. 2004; Harrison et al. 2006; van den Heuvel and Dyson 2008). The biochemical functions of these proteins are unknown, with the exception of RBAP48 and LIN54, which bind histones and DNA respectively (van den Heuvel and Dyson 2008; Sadasivam and DeCaprio 2013).

In mammalian cells, MuvB associates with p130-E2F4/5 to form DREAM in G_0 and early G_1, and it associates with B-Myb during S phase to form the Myb-MuvB (MMB) complex (Pilkinton et al. 2007; Schmit et al. 2007; Litovchick et al. 2011; Sadasivam et al. 2012). While DREAM represses gene expression, MMB activates late cell cycle genes during S phase and G2 both with and without FoxM1 (Georlette et al. 2007; Litovchick et al. 2007; Pilkinton et al. 2007; Schmit et al. 2007; Wen et al. 2008; Sadasivam et al. 2012). MuvB thus has an intriguing role in unifying cell cycle dependent gene expression, however the mechanisms by which DREAM and MMB-FoxM1 are assembled and regulated to carry out their specific functions are not well understood. DREAM formation requires the phosphorylation of MuvB protein LIN52 at serine residue 28 (phosS28) by the DYRK1A kinase (Litovchick et al. 2011). “Delta DREAM” mice that lack p130 and carry a p107 mutant allele incapable of binding MuvB display an identical phenotype to p107/p130 double knockout mice, suggesting an intimate relationship between the pocket proteins and MuvB proteins during cell cycle arrest (Forristal et al. 2014). While there are some reports of MuvB binding Rb (Gagrica et al. 2004; Korenjak et al. 2004), other evidence indicates that the DREAM complex only assembles with either p107 or p130 (Litovchick et al. 2007; Pilkinton et al. 2007; Schmit et al. 2007; Forristal et al. 2014). p130 expression levels are high during quiescence, and p130 is an established biomarker at this stage of the cell cycle in which DREAM is a repressor of gene expression (Smith et al. 1996; Henley and Dick 2012). Loss of p130 results in upregulated expression of p107 and subsequent recruitment of p107 to

MuvB (Litovchick et al. 2007; Forristal et al. 2014). MuvB dissociation from pocket proteins coincides with Cyclin-dependent kinase (Cdk) activity (Pilkinton et al. 2007), suggesting that Cdk phosphorylation of p107 and p130 may inhibit DREAM formation in cycling cells. Knowledge of the molecular architecture of the MuvB complex, how MuvB binds different transcription factors, and how these associations are manipulated throughout the cell cycle is important for understanding such fundamental processes as entry into quiescence and mitotic cell cycle control.

Here we describe the structural mechanisms of DREAM assembly following DYRK1A phosphorylation and DREAM inhibition by either oncogenic viral proteins or Cdk phosphorylation. We find that phosphorylated LIN52 binds the pocket domain of p107 or p130 using a short sequence that is a tunable variation on the canonical 'LxCxExL' Rb-binding sequence. A crystal structure of a LIN52-p107 complex explains the requirement for phosphorylation, why the association is specific for p107/p130 and not Rb, and how DREAM is inhibited by viral proteins. The structural observations lead us to uncover a novel model for cell cycle dependent regulation of DREAM assembly in which Cdk phosphorylation of pocket proteins induces a conformation that is incompatible with LIN52 binding.

2.2 Results

2.2.1 *p107 and p130 directly associate with LIN52*

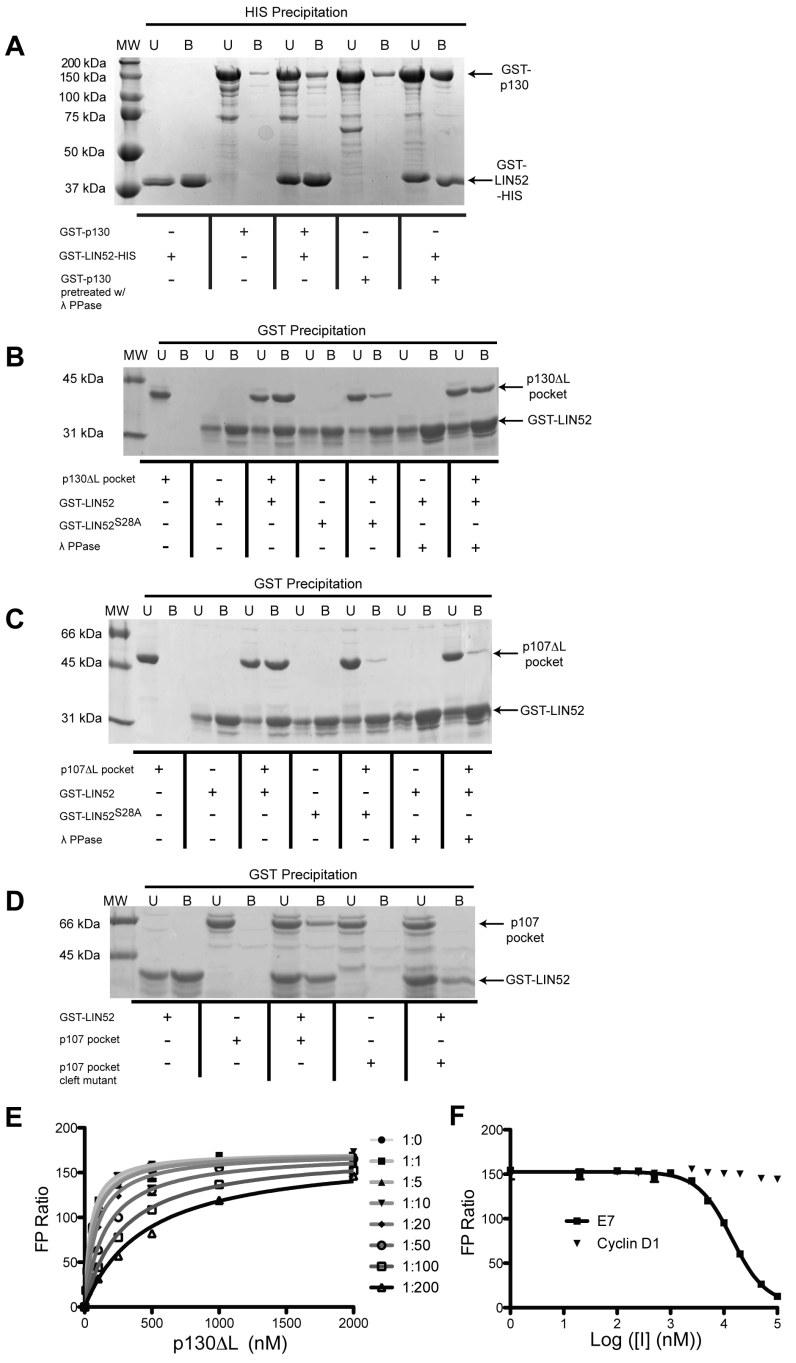

Figure 2.1. Direct association between LIN52 and p107/p130. Co-precipitation experiments performed with recombinant purified proteins. The indicated proteins were mixed, precipitated with the appropriate resin, and both unbound (U) and bound (B) fractions were analyzed using polyacrylamide gel electrophoresis and Coomassie staining. (A) Co-precipitation of the full length GST-p130 and GST-LIN52-HIS expressed in Sf9 cells

using Ni^{2+}-NTA resin. Treatment of the p130 with lambda phosphatase during purification increases the amount of p130 appearing in the bound fraction. (B) Co-precipitation of the untagged p130DL pocket domain expressed in Sf9 cells with GST-LIN52$^{13-45}$ using GS4B sepharose resin. Mutation of S28 in LIN52 or its treatment with lambda phosphatase weakens the p130DL association. (C) Same as (B) but with p107DL pocket domain. (D) Similar experiment to (B) but using p107 pocket domain (loops intact) and an LxCxE cleft (I931A, N935A, and V939A) mutant. (E) A fluorescence polarization assay demonstrating inhibition of the LIN52-p130 association by an HPV E7 peptide. 10 nM TMR-LIN52$^{12-34;phosS28}$ was mixed with increasing concentration of p130DL. Different saturation curves are at the indicated molar ratio of TMR-LIN52$^{12-34;phosS28}$ to E7$^{21-29}$ peptide. The affinity of TMR-LIN52$^{12-34;phosS28}$ in the absence of E7$^{21-29}$ is K_d = 53 ± 2 nM. (F) FP measurements made of 10 nM TMR-LIN52$^{12-34;phosS28}$ in the presence of saturating (2000 nM) p130DL and increasing concentrations of E7$^{21-29}$ peptide (squares) as the inhibitor (I). As a negative control, a peptide corresponding to the N-terminus of Cyclin D1 (residues 1-17) was used (triangles). This peptide does not associate with p130DL (Figure 2.10).

It has previously been shown that p107 and p130 co-immunoprecipitate with MuvB proteins if S28 in LIN52 is phosphorylated by DYRK1A (Litovchick et al. 2011). To determine if LIN52 directly associates with p130, we performed a series of binding experiments with recombinant, purified proteins. We first purified full length GST-LIN52-HIS and GST-p130 both expressed in Sf9 cells and found co-precipitation using Ni^{2+} affinity resin (**Fig. 2.1 A**). Electrospray mass spectrometry indicated that the LIN52 purified from Sf9 cells is phosphorylated (**Fig. 2.6 A and 2.6 B).** Given the observation that the binding appears substoichiometric, we postulated that p130 is heterogeneously phosphorylated in Sf9 cells, as previously observed for Rb (Burke et al. 2010), and that phosphorylation weakens LIN52 association. We treated p130 with lambda phosphatase during purification and observed a band shift on a Phos-tag SDS-PAGE gel (**Fig. 2.6 C)**. After treatment with and subsequent separation from phosphatase, the p130-LIN52 complex stability appears increased (**Fig. 2.1 A**).

We next tested whether phosphorylation of S28 in LIN52 is necessary for its direct interaction with pocket proteins. p130 and p107 pocket domains were expressed and purified from *E. coli* without posttranslational modifications. These constructs (p107DL and p130DL) each lack two internal loops and are similar to crystallized Rb constructs that maintain E2F and viral protein binding activity (Lee et al. 1998; Balog et al. 2011). We also purified LIN52

constructs expressed in Sf9 cells containing the N-terminal domain (residues 13-45; LIN52$^{13-45}$). We found that LIN52$^{13-45}$ is sufficient for direct association with the p130 and p107 pocket domains. An S28A mutation in LIN52$^{13-45}$ or lambda phosphatase treatment reduces binding to p130 and p107 (**Fig. 2.1 B and 2.1 C**), demonstrating the importance of S28 phosphorylation for formation of the complex.

The pocket domain contains two protein interaction interfaces--the LxCxE cleft and the E2F transactivation domain (E2F^{TD}) binding site (Lee et al. 1998; Lee et al. 2002; Xiao et al. 2003; Dick and Rubin 2013). The LxCxE cleft binds viral and endogenous proteins containing an "LxCxExf" sequence motif (x is any and f is a hydrophobic amino acid) (Jones et al. 1990; Lee et al. 1998; Singh et al. 2005). A p107 cleft mutant fails to assemble DREAM *in vivo* (Forristal et al. 2014), and we therefore hypothesized that LIN52 directly binds to the LxCxE cleft rather than the E2F^{TD} site. In support of this hypothesis, a purified p107 pocket domain cleft mutant (I931A, N935A, and V939A) fails to bind LIN52 (**Fig. 2.1 D**).

The DREAM complex is perturbed in cervical cancer cells infected with human papillomavirus type 16 (HPV16), and knockdown of the oncoprotein HPV16 E7 rescues DREAM assembly and promotes cell cycle arrest (Nor Rashid et al. 2011). To determine if HPV16 E7 can inhibit the direct LIN52 association with the p130 pocket domain, we used a fluorescence polarization (FP) competition assay. A LIN52$^{12-34;phosS28}$ peptide was labeled with a tetramethylrhodamine (TMR) dye and mixed with increasing amounts of p130DL to obtain FP saturation curves. Addition of E7$^{21-29}$ peptide to the binding reaction shifts the curves such that p130DL appears to bind with weaker affinity (**Fig. 2.1 E**). We then quantified the E7 peptide inhibition (K_i = 170 ± 50 nM) by displacing labeled LIN52$^{12-34;phosS28}$ peptide in the FP assay (**Fig. 2.1 E**). E7$^{21-29}$ contains an LxCxExL motif and inhibits LIN52 from interacting with p130, indicating that E7 disrupts DREAM by competitive inhibition at the LxCxE cleft of p130.

2.2.2 Crystal structures of LIN52-p107and E7-p107 complexes

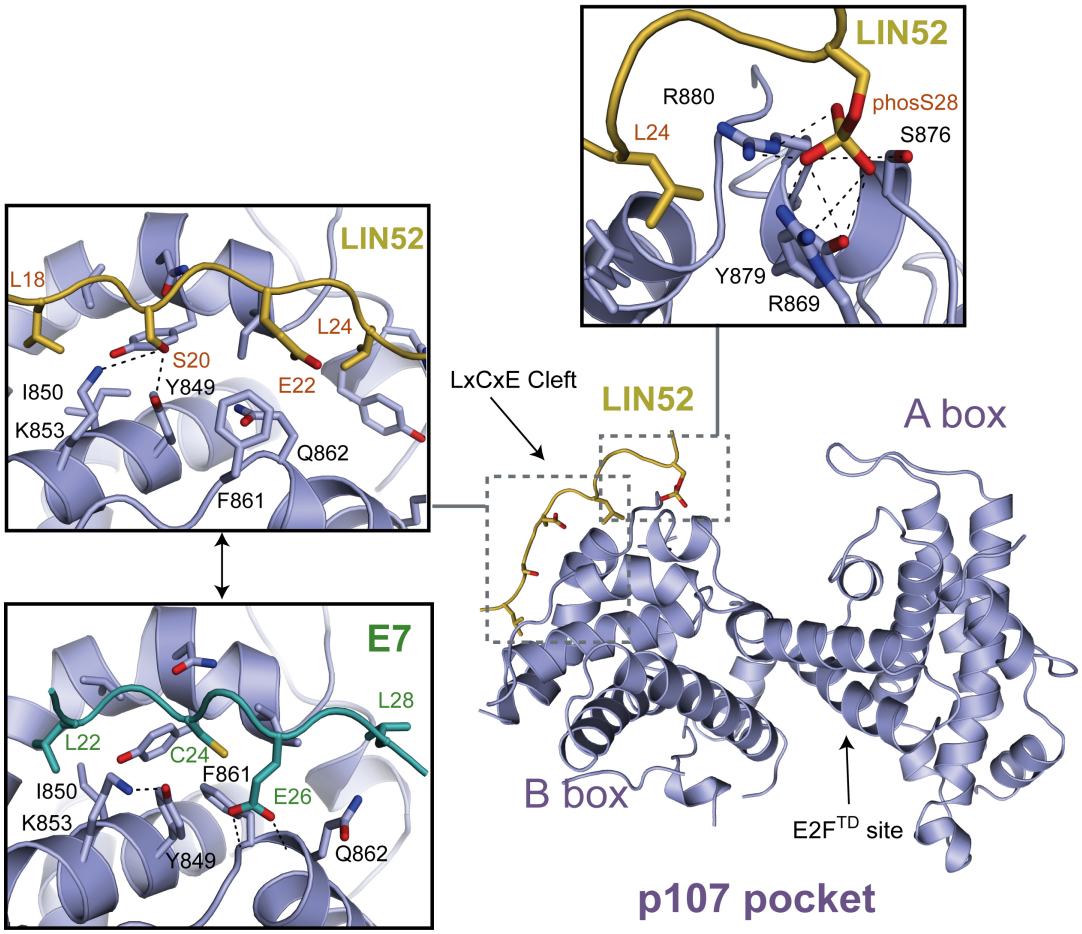

Figure 2.2. Crystal structures of the p107 pocket domain in complex with LIN52$^{12\text{-}34;phosS28}$ and E7$^{21\text{-}29}$. The LIN52 and E7 peptides both bind at the 'LxCxE' cleft (insets, left). The LIN52 association is mediated by the S28 phosphate, which contacts a p107/p130-specific binding pocket (inset top).

Table 2.1 X-ray crystallography data collection and refinement statistics for crystals containing p107DL and the indicated peptide. Values in parenthesis are for the high-resolution shell.

	E7$^{21-29}$	**LIN52$^{12-34;phosS28}$**	**LIN52$^{12-34;P29A;phosS28}$**
Data collection			
Space group	$C2_1$	$C222_1$	$C222_1$
Cell dimensions			
a, b, c	99.7, 76.6, 74.7	75.4, 101.1, 140.7	74.8, 100.5, 142.8
α, β, γ	90, 120.3, 90	90, 90, 90	90, 90, 90
Resolution (Å)	57.2 – 2.2	60.5 – 2.3	71.4 – 2.4
Total reflections	48,201	159,897	112,012
Unique reflections	21,552	24,252	21,397
I/σ	8.6 (2.1)	7.1 (2.2)	6.6 (1.8)
Completeness	93.2 % (94.4%)	99.5% (97.9%)	99.3% (97.9%)
Redundancy	2.2 (2.2)	6.6 (6.4)	5.2 (5.4)
R_{pim}	5.8% (25.2%)	7.0% (39.2%)	8.3% (44.2%)
$CC^{1/2}$	0.992 (0.759)	0.991 (0.556)	0.987 (0.472)
Refinement			
Resolution	57.2 – 2.2	60.5 – 2.3	71.4 – 2.4
Number of reflections	21,552 (2,171)	24,232 (2,297)	21,369 (2,084)
R_{work}	18.4% (21.9%)	19.9% (27.4%)	19.5% (26.9%)
R_{free}	24.0 (26.9%)	24.2% (30.0%)	24.2% (33.6%)
Number of atoms	3008	2970	3082
Protein	2877	2849	2934
Water	111	95	128
RMS deviations			
Bond lengths	0.005	0.005	0.007
Bond angles	0.87	0.93	1.23
Average B factor ($Å^2$)			
Overall	36.00	61.30	52.70
p107	34.53	59.10	50.25
Peptide	66.10	129.12	92.95
Ramachandran analysis			
Favored	97.4 %	96.0%	96.0%
Outliers	0.0 %	0.3%	0.3%

To identify the molecular interactions involved in DREAM assembly and oncoprotein-facilitated disruption, we solved the crystal structures of the p107DL pocket domain bound to a phosphorylated synthetic LIN52 peptide ($LIN52^{12\text{-}34;phosS28}$) at 2.3 Å and bound to an E7 ($E7^{21\text{-}29}$) peptide at 2.2 Å (**Fig. 2.2, Table 2.1)**. The structures reveal that the overall fold of the p107 pocket domain is similar to that of Rb, consisting of two helical subdomains called the A and B boxes. Each subdomain contains a five-helix Cyclin fold, flanked by additional helices that form the A-B interface, the LxCxE interface, or cover hydrophobic surfaces. As with previous Rb pocket domain structures (Lee et al. 1998; Lee et al. 2002; Xiao et al. 2003; Balog et al. 2011), most residues in the central loop between the two subdomains were left out of the crystallized construct, and the residues that remain are not visible in the electron density.

Structural alignment of the p107 and Rb pocket domains (PDB: 3POM) shows a root-mean square deviation in Ca position of only 1.2 Å (**Fig. 2.7 A).** While most secondary structural elements compare, relative to Rb, the p107 A box has two additional small helices (a4' and a10'). These helices consist of sequences for which the corresponding electron density in Rb is not observable. a10' occurs at the C-terminus of the A box and creates additional A-B interface contacts through packing against a11. The E7 peptide binds to the LxCxE cleft in the B-box of p107 as previously observed in the Rb-E7 complex structure (Lee et al. 1998) (**Fig. 2.2 and Fig. 2.7 B**). The similar specific contacts made are consistent with the high sequence homology between Rb and p107 within the LxCxE cleft.

In the p107DL-$LIN52^{12\text{-}34;phosS28}$ structure, LIN52 binds at the LxCxE cleft consistent with our co-precipitation experiments**.** The LIN52 peptide binds with an LxSxExL (residues 18-24) motif and makes a similar set of interactions as the E7 peptide (**Fig. 2.2, Fig. 2.3 A**). However, several striking differences arise from the presence of the more polar hydroxyl group in the LIN52 serine sidechain. S20 occupies the analogous place in the sequence as the cysteine in the canonical E7 peptide LxCxExf motif. C24 in the E7 peptide fits in a

hydrophobic pocket formed by F861 and Y849. In contrast, S20 in LIN52 makes hydrogen bonds with the K853 and Y849 sidechains. The position of both the F861 and Y849 sidechains are changed in the LIN52 complex such that the F861 phenyl ring is flipped out towards solvent. Whereas the E7 peptide E26 sidechain makes hydrogen bonds with the backbone of F861 and Q862, the LIN52 E22 sidechain is occluded from the analogous position by the flipped out F861 sidechain. These structural differences suggest that the LIN52 serine-containing motif binds with weaker affinity than the canonical E7 motif.

The S28 phosphoserine sidechain in LIN52 binds a positively charged pocket in p107 consisting of R869, S876, Y879, and R880. These p107 sidechains are highly conserved in p107 and p130 paralogs but not in Rb (**Fig. 3A**). Rb notably has F739 at the Y879 position in p107 and lacks the phenolic hydroxyl group that hydrogen bonds with the LIN52 phosphate. The lack of the phosphate-binding pocket in Rb supports and explains previous observations that the DREAM complex does not assemble with Rb (Litovchick et al. 2007; Pilkinton et al. 2007; Schmit et al. 2007; Forristal et al. 2014). The intervening amino acids between the 'LxSxExL' sequence and phosS28 loop out from the p107 domain and do not make any direct contacts (**Fig. 2**). We also solved a crystal structure of p107DL in complex with a mutant peptide ($LIN52^{12\text{-}34;P29A;phosS28}$) that binds with higher affinity (**Table 2.1 and Table 2.2**). The electron density corresponding to the LIN52 peptide is stronger in this structure and allows for observation of additional interactions between W32 in LIN52 and E863, M865, R869, and Y879 in p107 (**Fig. 2.8**).

While p107 and p130 loss in genetic models does not readily lead to tumors, there is evidence that p107 and p130 have tumor suppression function and can compensate for Rb loss in certain contexts (Dannenberg et al. 2004; Wirt and Sage 2010). The cBioPortal for Cancer Genomics catalogs a number of missense and nonsense mutations in both p107 and p130 that occur in human cancer samples (Gao et al. 2013). We found that 31 of the currently reported missense mutations for p107 are within the structured pocket domain (**Fig.**

2.9). Based on the location of these residues in our crystal structure, we predict that 21 of these 31 mutations would destabilize the protein and likely result in functional loss. Three other mutations map to the E2F binding surface based on the analogous Rb-E2F structure (Lee et al. 2002; Xiao et al. 2003). Notably, two mutations (R880I and Y934C) and an analogous p130 mutation map to the LIN52 interface, and we found that these p107 mutations weaken the LIN52$^{12\text{-}34;\text{phosS28}}$ peptide affinity (**Fig. 2.9**). These observations support the idea that p107/p130-dependent growth control, both through E2F inhibition and DREAM function, plays an important role in tumor suppression.

2.2.3 LIN52 S28 phosphorylation increases 'LxSxExL' affinity

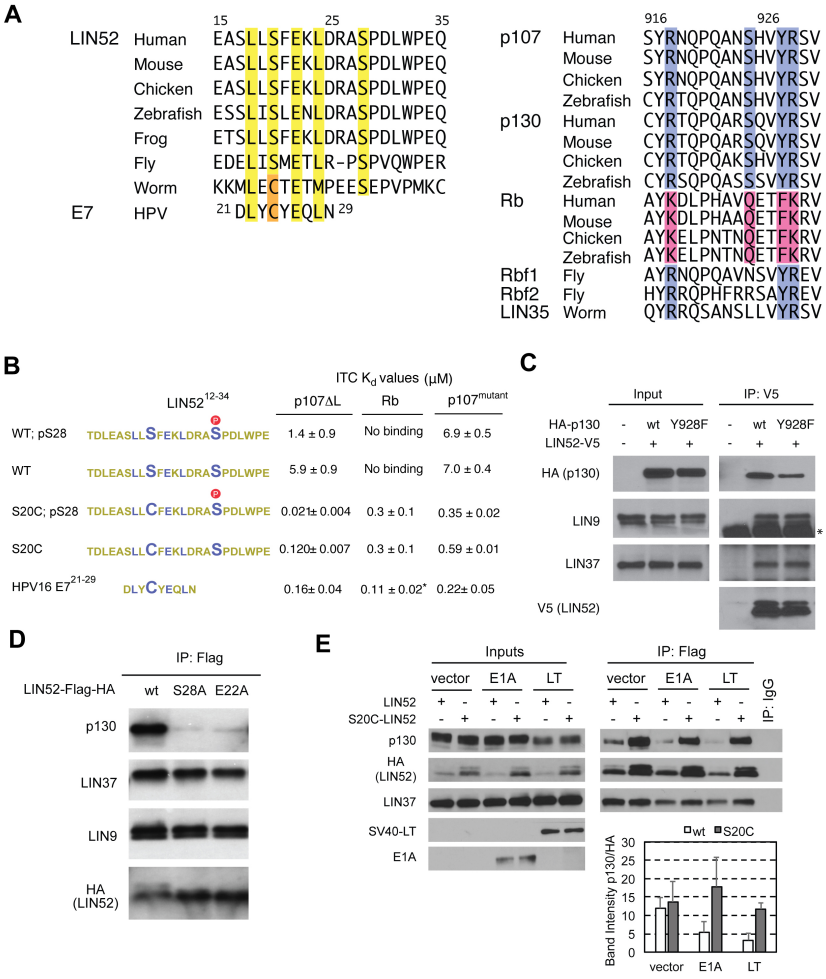

Figure 2.3. Role of the 'LxSxExL' motif and S28 phosphorylation on LIN52-p107/p130 association. (A) Alignment of LIN52 (left) and pocket protein (right) sequences. The LIN52 'LxSxExLxxxpS' motif and S28 phosphate binding residues are highlighted. (B) ITC affinity measurements of LIN52$^{12-34}$ variants and E7$^{21-29}$ binding to pocket proteins. *Value previously reported (Lee et al. 1998). (C) T98G cells were co-transfected with LIN52-V5 and the indicated HA-p130, extracts were immunoprecipitated with an anti-V5 antibody, and proteins were detected with the appropriate antibodies in a Western blot. The band in the LIN9 blot marked with an asterisk is nonspecific. (D) T98G cells stably expressing the wild-type or mutant LIN52-Flag-HA alleles were serum starved for 48 hours, and the co-immunoprecipitation was performed as in (C) except with an anti-Flag antibody. (E) As in (C), wild-type (WT) and S20C mutant LIN52-Flag-HA and viral proteins SV40 Large T antigen (LT) and adenovirus E1A were transiently expressed in cycling T98G cells as indicated. Bands intensities for the immunoprecipitated HA-LIN52 and p130 were quantified, and the p130/LIN52 ratio is plotted. Error bars are standard deviations for two different replicates of the experiment.

Table 2.2. Affinity of LIN52 peptides for the p107 pocket domain. See Figure 2.10 for exemplary ITC traces.

Peptide	p107DL Affinity (μM)
$LIN52^{12\text{-}34;phosS28}$	1.4 ± 0.8 μM
$LIN52^{12\text{-}34;E22A;phosS28}$	5.5 ± 0.3 μM
$LIN52^{12\text{-}34;L18A;phosS28}$	14.9 ± 0.1 μM
$LIN52^{12\text{-}34;L24A;phosS28}$	7.4 ± 0.9 μM
$LIN52^{12\text{-}34;+A28;phosS29}$	1.7 ± 0.3 μM
$LIN52^{12\text{-}34;-A27;phosS27}$	0.126 ± 0.002 μM
$LIN52^{12\text{-}34;P29A;phosS28}$	0.035 ± 0.003 μM

Our structural data suggest that the 'LxSxExL' sequence in LIN52 binds to the pocket domain with lower affinity than a canonical 'LxCxExL' sequence and that phosphorylation increases affinity specifically in p107 and p130 to make a more stable complex. We tested these ideas by quantitatively measuring the affinity of different LIN52 peptides using isothermal titration calorimetry (**Fig. 2.3 B, Fig. 2.10**). $LIN52^{12\text{-}34;phosS28}$ binds p107DL with an affinity of K_d = 1.4 ± 0.9 μM and the p130DL with a similar affinity of K_d = 1.0 ± 0.1 μM. An unphosphorylated $LIN52^{12\text{-}34}$ peptide binds p107DL with weaker affinity (K_d = 5.9 ± 0.9 μM). Mutation of S20 to a cysteine increases affinity for p107DL ($LIN52^{12\text{-}34;S20C}$ K_d = 0.120 ± 0.007 μM). The sensitivity of the canonical LxCxExf motif to a serine substitution has previously been observed in the case of the E7 peptide and Rb (Jones et al. 1990). We find that the $LIN52^{12\text{-}34;S20C}$ affinity for p107DL is similar to the affinity of the HPV16 $E7^{21\text{-}29}$ peptide for p107DL (K_d = 0.16 ± 0.04 μM). S28 phosphorylation in the context of the S20C mutation still increases affinity ($LIN52^{12\text{-}34;S20C;phosS28}$ K_d = 0.021 ± 0.004 μM) such that it is tighter than the wild-type phosphorylated LIN52 sequence.

No binding was observable upon mixing of either $LIN52^{12\text{-}34}$ or $LIN52^{12\text{-}34;phosS28}$ peptide with Rb. The $LIN52^{12\text{-}34;S20C}$ peptide (K_d = 0.3 ± 0.1 μM) binds Rb with similar affinity

as p107, however phosphorylation results in no additional increase in affinity ($LIN52^{12-34;S20C;phosS28}$ K_d = 0.3 ± 0.1 μM). This result corroborates the lack of a phosphate-binding pocket in Rb. We also mutated the residues in p107DL that contact LIN52 phosS28 in the crystal structure such that they resemble the Rb sequence (R869K, S876Q, Y879F, and R880K). LIN52 and $LIN52^{12-34;S20C}$ bind the Rb-like mutant ($p107^{mutant}$) with weaker affinity compared to p107DL, and phosphorylation does not enhance affinity (**Fig. 2.3**). The $E7^{21-29}$ peptide binds $p107^{mutant}$ and p107DL with similar affinity, which is consistent with a lack of interaction between E7 and the phosphate pocket.

The fact that $LIN52^{12-34}$ and $LIN52^{12-34;phosS28}$ bind $p107^{mutant}$ with greater affinity than Rb suggests that p107-specific interactions other than the phosphate-binding pocket stabilize LIN52 association. One possible explanation observed in the crystal structure is the presence of I850 in p107. I850 contacts Y849 and stabilizes the Y849 position for hydrogen bonding to S20 in LIN52 (**Fig. 2.2**). In contrast, G710 at the corresponding position in Rb cannot play the same stabilizing role and is likely a source of the lower Rb affinity for the noncanonical 'LxSxExL' motif relative to p107/p130.

We tested the significance of the p107/p130 specific phosS28-binding site for DREAM assembly in cells (**Fig. 2.3**). T98G cells were co-transfected with V5-tagged LIN52 and either wild-type HA-p130 or HA-p130 with a Y928F mutation (equivalent to Y879F in p107). LIN52-V5 was precipitated with an anti-V5 antibody, and we examined the amount of precipitated p130 by Western blot. LIN52 co-precipitated less Y928F mutant p130 protein than wild-type, supporting the requirement of an intact phosphate-binding pocket as observed in the crystal structure for DREAM assembly.

2.2.4

The 'LxSxExL' sequence motif is critical for DREAM assembly

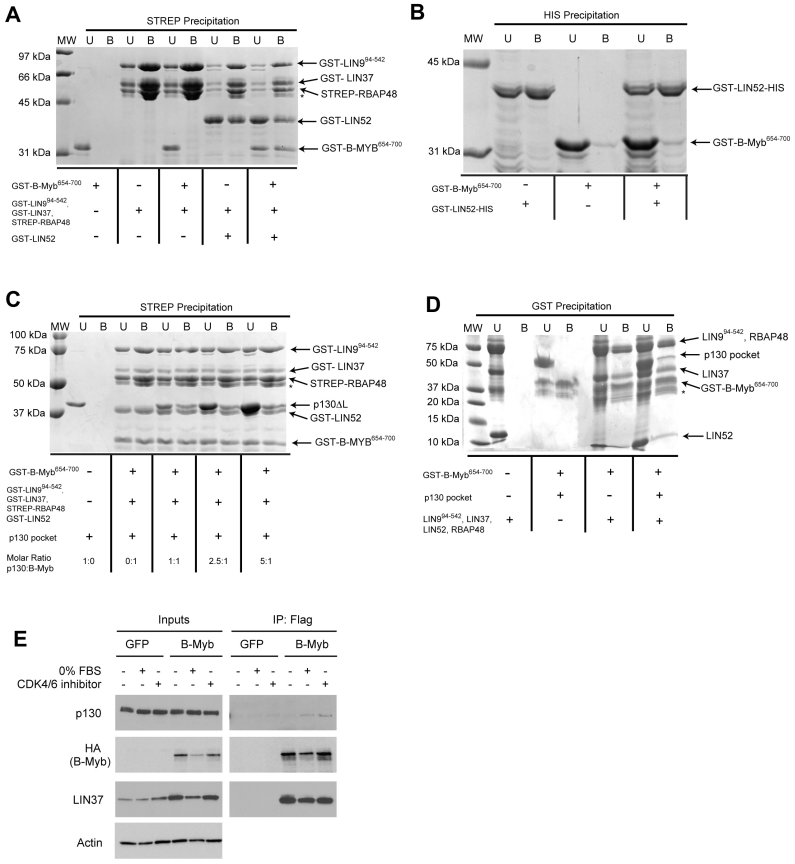

Figure 2.4. B-Myb and p130 bind distinct surfaces of MuvB. Co-precipitation experiments were conducted with recombinant proteins as in Fig. 1. (A) Streptactin co-precipitation of Step-tagged RbAP48, GST-LIN9$^{94-542}$, GST-LIN37 with GST-B-Myb$^{654-700}$ in the absence and presence of GST-LIN52 demonstrates the requirement of LIN52 for B-Myb-MuvB binding. The band marked with an asterisk is a GST-LIN9$^{94-542}$ degradation product. (B) Ni^{2+}-NTA fails to co-precipitate GST-B-Myb$^{654-700}$ with GST-LIN52-HIS alone. (C) Streptactin co-precipitation of Step-tagged RbAP48, GST-LIN9$^{94-542}$, GST-LIN37, GST-LIN52 with GST-B-Myb$^{654-700}$ in the presence of increasing amounts of p130DL. The amount of co-precipitated GST-B-Myb$^{654-700}$ does not change, demonstrating that the p130 pocket domain does not compete with B-Myb for MuvB binding. The band marked with an asterisk is a GST-LIN9$^{94-542}$ degradation product. (D) GST-B-Myb$^{654-700}$ co-precipitates the untagged p130 pocket domain only in the presence of the untagged MuvB components, indicating both B-Myb and p130 can simultaneously bind MuvB. The band marked with an asterisk are degradation products of GST-B-Myb$^{654-700}$. (E) Association of p130 and MuvB with ectopically expressed B-Myb. BJ-hTERT fibroblasts stably expressing HA-Flag tagged GFP (control) or B-Myb were incubated for 24h in complete medium, in the medium without FBS, or in medium containing CDK4/6 inhibitor. Proteins of interest were detected by Western blot in the cell extracts (Inputs) and in the anti-Flag pull-downs (IP:FLAG).

To explore further the important elements of the LIN52 'LxSxExL' binding motif, we measured the affinity of different LIN52$^{12\text{-}34}$ peptides for the p107 pocket domain using the ITC assay (**Table 2.2 and Figure 2.5**). Both the L18A (K_d = 14.9 ± 0.1 μM) and L24A (K_d = 7.4 ± 0.9 μM) consensus mutations in LIN52 reduce affinity. Although E22 in LIN52 does not make any interactions with p107 in the crystal structure (**Fig. 2.2**), we also find that an E22A mutation (K_d = 5.5 ± 0.1 μM) reduces affinity 4-fold compared to wild-type (K_d = 1.4 ± 0.8 μM). We suggest that in solution there is an additional alternate conformation in equilibrium that resembles the E7 peptide conformation but is less stable because of the buried S20 hydroxyl group.

We also measured the effects of moving the position of phosS28 relative to the 'LxSxExL' motif. Addition of an alanine to the intervening three residues results in similar affinity (LIN52$^{12\text{-}34;+A28;phosS29}$; K_d = 1.7 ± 0.3 μM), while the peptide with A27 deleted binds with 10-fold tighter affinity (LIN52$^{12\text{-}34;-A27;phosS27}$; K_d = 0.126 ± 0.002 μM). This observation is consistent with a lack of interactions between the intervening sequence and pocket domain (**Fig. 2.2**). The tighter affinity of the shorter sequence may result from a reduced entropic penalty for binding. Many kinases phosphorylate substrates bearing an (S/T)P motif, which include DYRK1A and the CDKs (Ubersax and Ferrell 2007). We tested a LIN52 phosS28 P29A mutant to determine if p107 binding is also dependent upon this motif. The mutant has a higher affinity (LIN52$^{12\text{-}34;P29A;phosS28}$; K_d = 0.035 ± 0.003 μM), than wild-type, suggesting that the proline is required for kinase recognition of S28 but is not preferred at this position for pocket binding.

To determine if the p130 pocket association with the LIN52 'LxSxExL' motif is required for DREAM assembly in cells, we generated LIN52-HA-FLAG mutants stably expressed in T98G cells. We then immunoprecipitated the FLAG sequence and examined the co-precipitation of p130 by Western blot. When either E22 or S28 is mutated in LIN52,

p130 binding is diminished while binding of the MuvB proteins LIN37 and LIN9 is preserved (**Fig. 2.3**). We also tested the stabilizing effect of an S20C mutant on the LIN52-p130 complex by co-precipitation (**Fig. 2.3**). The LIN52-HA-FLAG S20C mutant expresses at a higher level than wild-type but does not co-precipitate a relative greater amount of p130. However, when co-expressed with either E1A or large T-antigen viral proteins, both of which contain 'LxCxExL' sequences, LIN52 S20C does co-precipitate a relative greater amount of p130 than wild-type. We conclude that the wild-type sequence is sufficient to co-precipitate p130 but when challenged with high affinity viral proteins, the increase in affinity from the S20C mutation allows LIN52 to better compete with E1A and large T-antigen for p130 binding. This result emphasizes how the weaker 'LxSxExL' motif in LIN52, even with the addition of S28 phosphorylation, enables DREAM disassembly by competitor viral oncoproteins.

2.2.5 B-Myb requires LIN52 to bind to MuvB but does not compete with p130

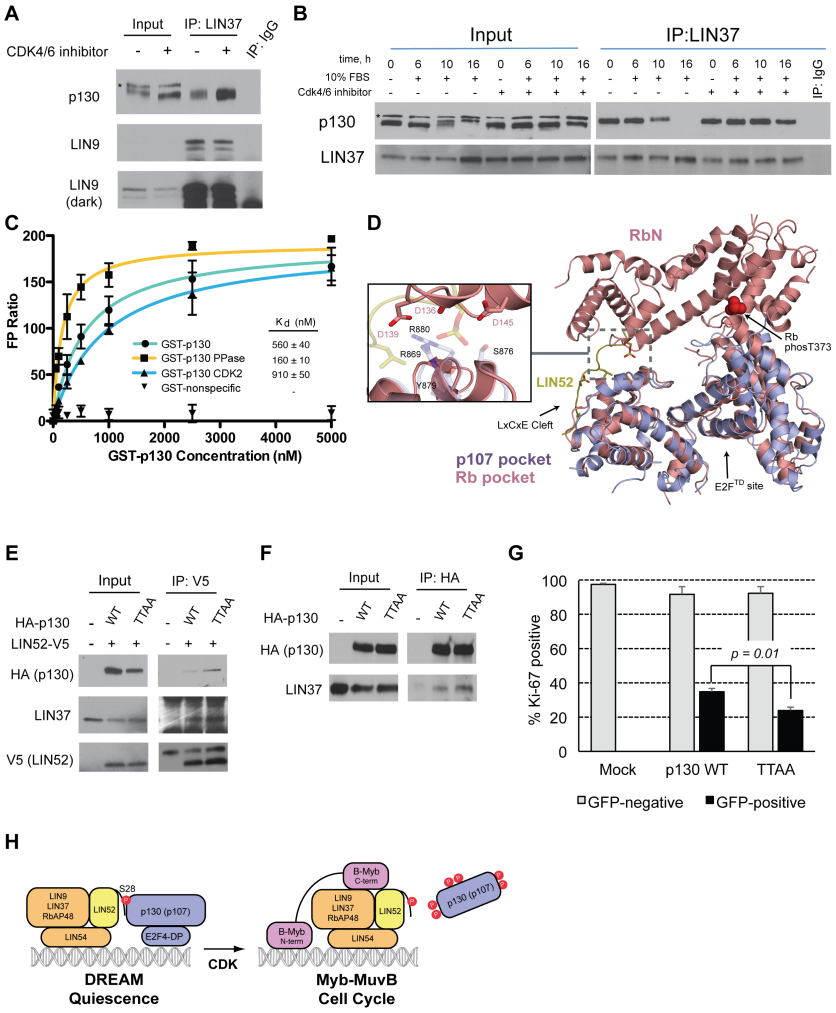

Figure 2.5. p130 phosphorylation weakens LIN52 binding and DREAM activity
(A) T98G cells were incubated for 24h in the presence or absence of CDK4/6 inhibitor. Binding of p130 to LIN37 was determined by co-immunoprecipitation with an anti-LIN37 antibody and detection of proteins in a Western blot. The band marked with an asterisk in the p130 input blot is a nonspecific band. (B)T98G cells were serum starved for 72 hours and then released with addition of 10% FBS in the absence or presence of the Cdk4/6 inhibitor palbociclib. After harvesting cells at the indicated time points, extracts were immunoprecipitated with an anti-LIN37 antibody and probed for LIN37 and p130. The band marked with an asterisk in the p130 input blot is a nonspecific band. (C) Fluorescence polarization binding assay of TMR-labeled LIN52$^{12\text{-}34;\text{phosS28}}$ to GST-p130. The GST-p130 is purified from sf9 cells and used untreated (green, circles), treated with lambda phosphatase (yellow, squares), and treated with Cdk2 kinase (blue, triangles). Purified GST alone was used as a negative control (inverted triangles). The expected effect of enzyme treatment is corroborated with a Phos-tag gel (Supplemental Figure 1C). (D) Overlay of the LIN52$^{12\text{-}34;\text{phosS28}}$-p107 structure and phosphorylated Rb$^{55\text{-}787}$ structure (PDB: 4ELJ). Residues in p107 that bind the S28 phosphate in LIN52 (rendered as transparent blue sticks) are analogous to residues in the Rb pocket domain that bind the docked RbN domain (pink) when Rb is phosphorylated. (E) U2-OS cells

were transfected with LIN52-V5 and the wild-type or T401A/T417A (TTAA) mutant HA-p130. Extracts were immunoprecipitated with anti-V5 antibody and the indicated proteins were detected by Western blot. (F) Same as (E) except an anti-HA antibody was used for immunoprecipitation. (G) U2OS cells were co-transfected with the wild-type or T410A/T417A (TTAA) mutant of p130 and GFP as tracer. The expression of Ki-67 was determined by indirect immunofluorescence cell staining at 48 h post-transfection. The graph shows the average values and standard deviations (error bars) of 3 replicate experiments in which at least 100 cells were counted per condition. The p-value evaluating statistical significance was calculated using a two-tailed student's t-test. (H) Model for DREAM complex disassembly and Myb-MuvB complex assembly upon Cdk activation.

We next investigated the determinants of B-Myb binding to MuvB in order to compare the mechanisms of DREAM and MMB assembly. The evolutionarily conserved MuvB proteins in the *Drosophila melanogaster* Dream complex were found to interact with the C-terminus of B-Myb (Andrejka et al. 2011). To test whether this association is direct and conserved in the human proteins, we performed a series of precipitation experiments with recombinant B-Myb and MuvB proteins from Sf9 cells (**Fig. 2.4**). We reconstituted the core MuvB subcomplex by co-expressing GST-LIN9$^{94-542}$, which lacks its poorly conserved and putative unstructured N-terminus, along with full-length GST-LIN37, Strep-RBAP48, and GST-LIN52 as indicated. The purified complexes were then co-precipitated in the presence of the C-terminus of B-Myb (GST-B-Myb$^{654-700}$). We find that GST-B-Myb$^{654-700}$ binds the MuvB subcomplex only in the presence of LIN52 (**Fig. 2.4**). However, full-length GST-LIN52-HIS, which is sufficient to co-precipitates p130 (Fig. 1A), is not sufficient to co-precipitate GST-B-Myb$^{654-700}$ (**Fig. 2.4**). We conclude that LIN52 is necessary but not sufficient for B-Myb binding. The requirement for LIN52 could result from direct B-Myb-LIN52 contacts or because LIN52 is necessary for a properly structured MuvB core.

We next tested whether p130 and B-Myb compete for access to MuvB or whether they can both simultaneously bind. We find that Strep-tagged RbAP48, together with the other components of the MuvB subcomplex, co-precipitates both GST-B-Myb$^{654-700}$ and GST-p130 pocket when all components are mixed in the same solution (**Fig. 2.4**). Increasing the

amount of GST-p130 does not change the amount of GST-B-Myb$^{654-700}$ that co-precipitates, consistent with a lack of competition (**Fig. 2.4**). We also find that GST-B-Myb$^{654-700}$ co-precipitates p130 pocket if and only if the components of MuvB are present, demonstrating the presence of a complex that contains B-Myb$^{654-700}$, p130 pocket, and MuvB all together (**Fig. 2.4**). Based on these observations that p130 and B-Myb can simultaneously bind MuvB and that they have different requirements for binding, we conclude that they have non-overlapping binding sites on the MuvB core. In order to demonstrate that full-length p130 and B-Myb associate together with MuvB in cells, we precipitated HA-Flag-B-Myb that is stably expressed in BJ-hTERT fibroblasts (**Fig. 2.4**). We observe co-precipitation of endogenous LIN37 and p130 under conditions that support DREAM assembly, including serum starvation and Cdk4/6 inhibition with palbociclib (PD-0332991, Pfizer, Inc.). Although we cannot rule out a direct association between full-length p130 and B-Myb in this experiment, the data are consistent with B-Myb co-precipitating p130 through a common MuvB core.

2.2.6 CDK phosphorylation promotes DREAM disassembly

Components of the MuvB complex fail to associate with p107 and p130 in cycling cells, however the mechanism of DREAM inhibition upon exit from quiescence has not been elucidated. Considering that LIN52 is found phosphorylated and unphosphorylated at S28 when bound to B-Myb during S phase (Litovchick et al. 2011), dephosphorylation of LIN52 S28 is unlikely the primary mechanism promoting DREAM disassembly. Our result that B-Myb and p130 bind MuvB simultaneously also argues against a competitive mechanism for DREAM disassembly whereby upon expression, B-Myb displaces p130 from MuvB. Noting the coincident timing of Cdk activation and DREAM disassembly (Pilkinton et al. 2007), we tested directly whether Cdk activity correlated with p130 binding to MuvB. We find that the MuvB component LIN37 can co-precipitate a greater amount of p130 from the extracts of cycling T98G cells in the presence of the Cdk4/6 inhibitor (**Fig. 2.5**). To observe the effect of

Cdk inhibition on DREAM disassembly upon cell cycle entry, we released T98G cells from serum starvation and found that LIN37 co-precipitation of p130 persists to a greater extent in the presence of the Cdk4/6 inhibitor (**Fig. 2.5**). In the absence of inhibitor, the loss of p130 co-precipitation, beginning at 10 hours, correlates with the disappearance of the hypophosphorylated p130 form (lower band in gel). These results demonstrate that Cdk activity in cells inhibits p130-MuvB association.

We asked whether Cyclin D1 could inhibit DREAM assembly by directly competing with the LIN52 interaction at the p130 LxCxE cleft. Cyclin D1 was previously proposed to bind the LxCxE cleft in the Rb pocket domain (Dowdy et al. 1993). However, we found in our FP assay (**Fig. 2.1**) that a Cyclin D1 peptide does not displace LIN52 form p130DL. We also titrated the Cyclin D1 peptide bearing its 'LxCxExE' motif into p107DL and p130DL in the ITC assay and found no observable binding (**Fig. 2.10**), suggesting the Cyclin D1 sequence does not directly associate with the pocket domain. These results are supported by our ITC data and previous reports (Singh et al. 2005) that a hydrophobic residue is necessary at the downstream glutamic acid position in Cyclin D1.

We hypothesized that Cdk phosphorylation of p130/p107 inhibits the LIN52 interaction with the p130/p107 pocket domain. In support of this mechanism, we found that lambda phosphatase treatment of the partially phosphorylated p130 purified from Sf9 cells increased LIN52-p130 complex stability in a qualitative co-precipitation assay (**Fig. 2.1**). We quantified the effect of p130 phosphorylation on LIN52 binding using the fluorescence polarization (FP) assay described in **Fig. 2.1**. The TMR-LIN52$^{12\text{-}34;\text{phosS28}}$ peptide was mixed with increasing amounts of GST-p130 purified from Sf9 cells without treatment, with phosphatase treatment, and with kinase treatment. While phosphatase treatment increases the affinity 3.5 fold, Cdk2 phosphorylation decreases the affinity nearly 2-fold, demonstrating that p130 phosphorylation weakens LIN52 binding (**Fig. 5C**). The observation of a change in

affinity upon treatment with either enzyme reflects the partial phosphorylation of GST-p130 purified from Sf9 cells.

Our structural observation that phosphorylated LIN52 binds p107/p130 at the 'LxCxE' cleft suggests that Cdk phosphorylation events resulting in occlusion of the 'LxCxE'-site would inhibit DREAM assembly. Studies of inactive Rb have revealed phosphorylation-induced structural changes that block the 'LxCxE' cleft (Rubin et al. 2005; Burke et al. 2012; Rubin 2013). We considered one mechanism in which phosphorylation of conserved sites in the linker between the N-terminal (RbN) and pocket domains results in RbN-pocket docking (Burke et al. 2012). Alignment of the phosphorylated Rb structure with the p107-LIN52 complex suggests that an analogous closed conformation in p107/p130 would inhibit LIN52 binding **(Fig. 5D)**. In the Rb structure, residues in RbN form hydrogen bonds and salt bridge interactions with Rb pocket residues; the homologous residues in the p107 pocket domain contact the LIN52 S28 phosphate in the structure presented here.

To determine whether CDK phosphorylation disrupts the DREAM complex through phosphorylation of sites in the putative p107/p130 interdomain linker, we examined the effect of p130 T401A and T417A mutation on MuvB binding in cycling U2OS cells. We expressed LIN52 together with p130 wild-type and phosphosite mutant and found that LIN52 co-precipitates a greater amount of the T401A/T417A double mutant (**Fig. 5E**). We also found that the p130 double mutant can co-precipitate a great amount of endogenous LIN37 than wild-type (**Fig. 5F**). In order to test the functional consequences of mutating Cdk sites, we transfected U2OS cells with wild-type p130 and the T401A/T417A phosphosite mutant and examined proliferation of cells using S-phase-specific Ki-67 staining similar to as previously described (Canhoto et al. 2000). We find that the T401A/T417A mutant induces a more potent growth arrest than wild-type, which is consistent with stabilization of the DREAM complex (**Fig. 5G)**. T401 and T417 phosphorylation has also been shown to be relevant for

regulation of E2F4 activity (Farkas et al. 2002). Mutation of these sites may also influence p130-E2F4 affinity and contribute to the observed growth arrest by stabilizing E2F binding.

2.3 Discussion

Our structural and binding data support a model in which the DREAM complex is mediated by the direct association of LIN52 with the p107/p130 pocket (**Fig. 5H**). Assembly is promoted by DYRK1A phosphorylation of S28 in LIN52, while disassembly is induced by Cdk phosphorylation of sites in p107/p130 that promote structural changes to occlude the LIN52 binding surface. B-Myb binding is dependent on LIN52 and other members of the MuvB core and can occur simultaneously with p107/p130 binding in our assays with recombinant protein and in cells under conditions in which B-Myb is ectopically expressed and p130 is known to be hypophosphorylated. The fact that B-Myb and p130 are not found together in complexes purified from mammalian cells is likely due to the coincidence of B-Myb expression and p130 phosphorylation in those cells (Litovchick et al. 2007). Complexes have been purified from Drosophila cells containing both Myb and Rbf and may point to a distinct mechanism of regulation in lower metazoans. The *D. melanogaster* Rbf sequences notably lack conserved phosphorylation sites equivalent to T401 and T417 in p130, which further points to their importance in disassociating p130 from MuvB.

LIN52 accesses the 'LxCxE' cleft of the pocket domain using a non-canonical and non-optimal 'LxSxExL' motif in combination with phosphorylation at S28. The weak affinity of the 'LxSxExL' sequence sensitizes the association to regulatory phosphorylation by DYRK1A. Kinase phosphorylation acts as a switch, because it increases LIN52 binding to submicromolar affinity. We note that in contrast to higher orthologs, *C. elegans* LIN52 maintains the canonical, tight-binding LxCxE motif and lacks the equivalent DYRK1A consensus surrounding the S28 residue. We predict that DREAM in *C. elegans* is not regulated equivalently by phosphorylation, and LIN52 and LIN35 constitutively form a stable

complex. The LIN52 sequence in *D. melanogaster* resembles our LIN52$^{12\text{-}34;DA27;phosS27}$ peptide, suggesting Drosophila Rbf proteins and LIN52 also form a highly stable, phosphorylation-dependent interaction.

The requirement for LIN52 phosphorylation is an important source of specificity for p107 and p130 in DREAM assembly. Unlike Rb, the p107 and p130 pocket domains contain the proper phosphate-binding site. Phylogenetic sequence analysis of pocket proteins suggests that Rb appears more recently than p107 and p130, which are closer in sequence to pocket proteins such as LIN35 and Rbf in lower metazoans (van den Heuvel and Dyson 2008; Sadasivam and DeCaprio 2013). It is not clear then why Rb evolved such that it does not bind MuvB, although one possibility is that the LxCxE cleft in Rb must be reserved for some alternate unique function.

Despite their diverse cellular roles, the universal biochemical function of pocket proteins is to assemble protein complexes (Cobrinik 2005; Dick and Rubin 2013). It is estimated that several hundred proteins interact with Rb and its pocket protein paralogs, and the 'LxCxE' cleft has been described as the key interface for these complexes (Morris and Dyson 2001). The crystal structure presented here of the p107-LIN52 complex provides the first structural insights into how cellular proteins contact the cleft. It implicates the 'LxSxExLxxxpS' sequence as a novel binding motif that can be regulated by phosphorylation. We searched the Scansite 3 server (Obenauer et al. 2003) to identify other potential p107/p130 binding partners that use this motif and the motifs identified in our binding studies that bind the novel phosphate-binding pocket. We identified 203 proteins that matched our motifs, although only 13 are known to be phosphorylated on the consensus serine (Supplemental Table 1).

Cdk phosphorylation has been well characterized as a mechanism for inactivating pocket proteins, and both structural and functional studies have implicated the effects of phosphorylation on inhibiting pocket protein interactions (Cobrinik 2005; Rubin 2013). Our

results here further support phosphorylation of p107/p130 as a mechanism of inactivating the DREAM complex by dissociating pocket proteins from the MuvB core. Mutation of conserved Cdk sites T401 and T417 enhances the growth arrest properties of p130 and stabilizes the DREAM complex (**Fig. 5**). Structural and sequence comparison between p107/p130 and Rb suggests that a conserved closed conformation that occludes the 'LxCxE' cleft is induced by phosphorylation. We note that additional Cdk sites in p107/p130 may contribute to inhibition of LIN52 binding and that phosphorylation may also contribute to DREAM dissociation by inhibiting p107/p130 association with E2F proteins.

It has been suspected that cancer cells can in certain contexts avert the effect of cytotoxic treatments by entering quiescence. As an important mediator of cell cycle exit, DREAM may be an important additional target during chemotherapy. For example, cells from gastrointestinal stromal tumors enter quiescence following treatment with imatinib, and inhibition of DREAM assembly through genetic knockdown alternatively induces apoptosis (Boichuk et al. 2013). Our structural characterization of LIN52 association with p107 suggests that inhibitors of protein interactions at the LxCxE cleft in pocket proteins would likely block DREAM function *in vivo*. It is encouraging that only a short peptide corresponding to the E7 sequence is sufficient for inhibition of LIN52 association *in vitro* (**Fig. 2.1 F**), and small molecule inhibitors of the E7 LxCxE-Rb interaction have been reported (Fera et al. 2012). Discovery of more potent chemical inhibitors of LxCxE-pocket binding may prove to be a viable strategy for preventing cancer cells from escaping to quiescence as a mechanism for surviving therapeutic treatment.

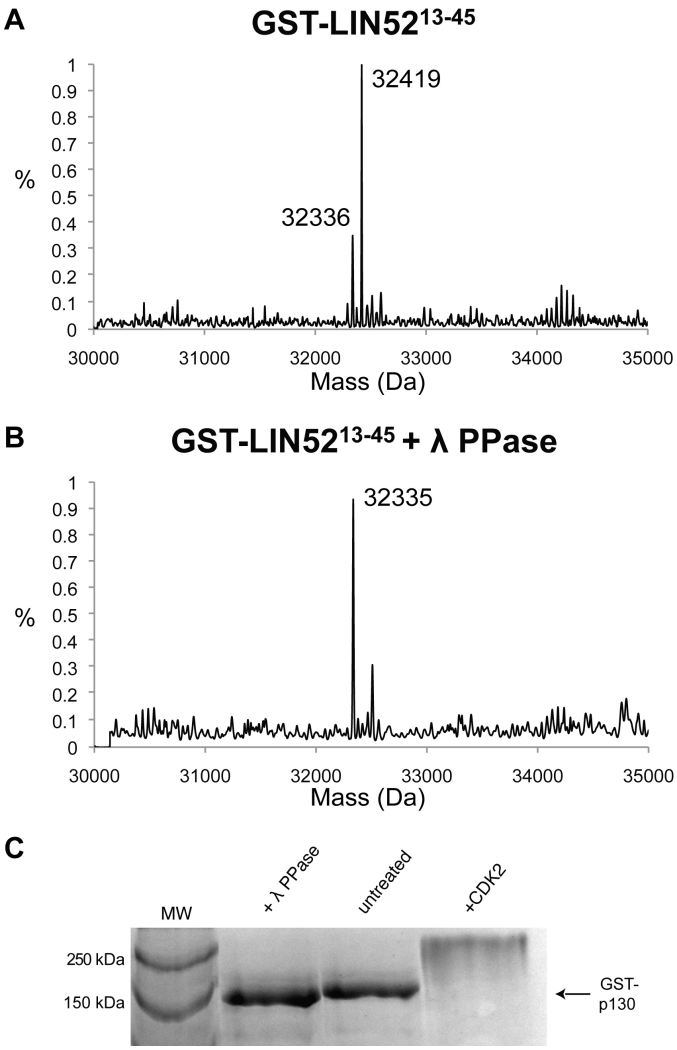

Figure 2.6. LIN52 and p130 expressed in Sf9 cells are phosphorylated. Electrospray mass spectrometry measurements of the LIN52 molecular weight before (A) and after (B) lambda phosphatase treatment shows recombinant LIN52 is phosphorylated in Sf9 cells. The change in mass is consistent with removal of one phosphate (~80 Daltons). (C) Phos-Tag SDS-PAGE gel showing GST-p130 purified from Sf9 cells with and without enzyme treatment. The anticipated effects of lambda phosphatase and Cdk2 kinase treatment on GST-p130 are observed as band shifts on the gel. The middle position of the untreated band suggests that GST-p130 purified from Sf9 cells is partially phosphorylated.

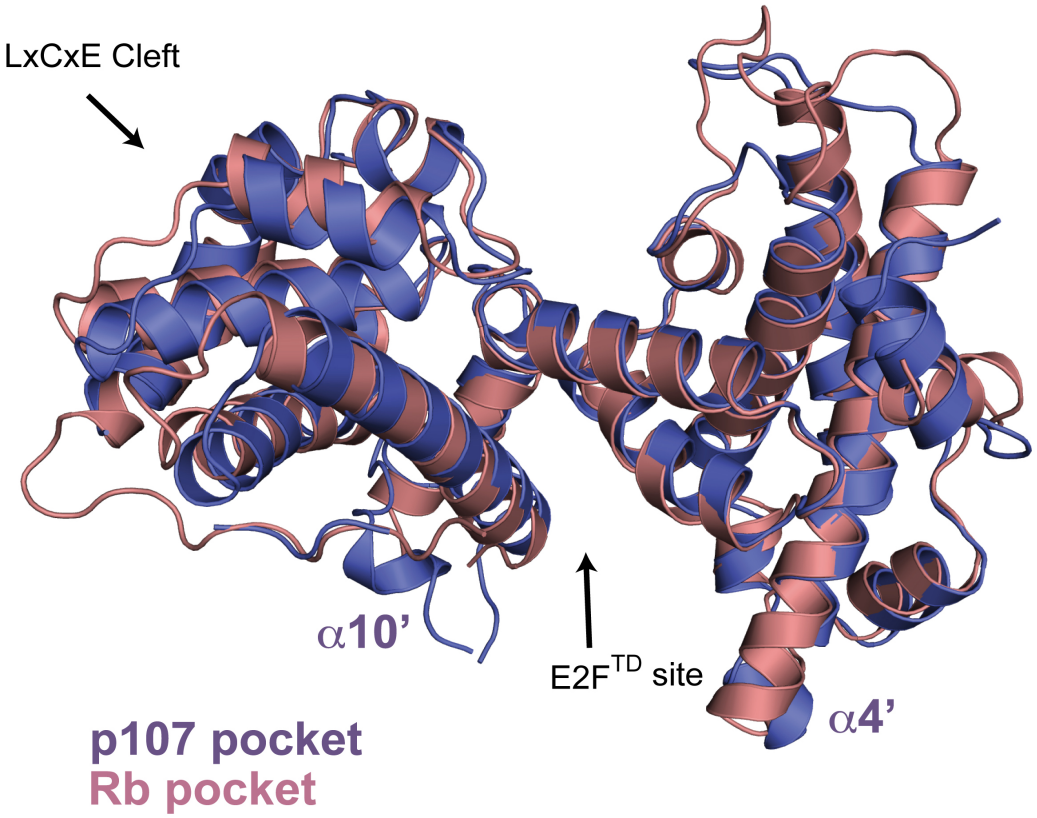

Figure 2.7. Comparison of the p107 and Rb structures. (A) Overlay of the pocket domains constructed by aligning Ca positions of the p107-E7 structure and the unliganded Rb structure (PDB ID: 3POM). (B) Overlay of the E7 'LxCxExL' peptide bound to p107 (teal) and Rb (green). The image was constructed by aligning the pocket domains of the p107-E7 structure and the Rb-E7 structure (PDB ID: 1GUX).

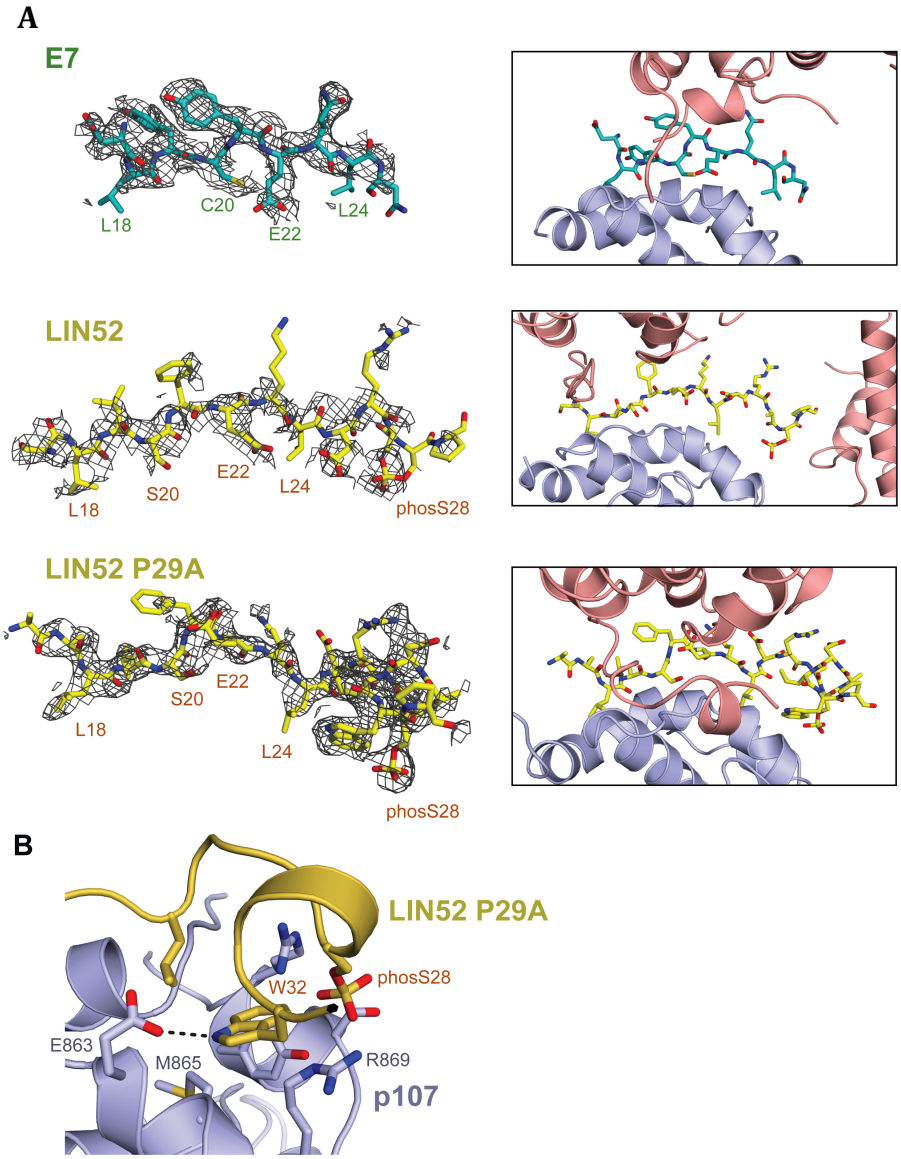

Figure 2.8. Electron density surrounding the E7$^{21-29}$, LIN52$^{12-34;phosS28}$, and LIN52$^{12-34;P29A;phosS28}$ peptides

(A) The peptides are shown together with their corresponding electron density to demonstrate how the diffraction data support each structural model. The mesh corresponds to an mf_o-Df_c simulated-annealing omit map contoured at 1.5 σ. The weaker density of the LIN52 peptide relative to the E7 peptide is reflected by the higher average B-fator (Table 1) and is likely due to a lower occupancy. The LIN52 peptide binds with 10-fold weaker affinity, and its affinity may be further weakened by the presence of the 1.7 M ammonium sulfate in the crystallization solution. In order to achieve stronger density and corroborate the LIN52 structural model, we soaked p107DL- LIN52$^{12-34;phosS28}$ crystals with 20-fold molar excess of the LIN52$^{12-34;P29A;phosS28}$

peptide. The mutant peptide binds with fifty-fold higher affinity than the wild-type peptide (Table 2). To the right, crystal packing around each peptide is shown for the three structures. (B) Additional interactions observed in the p107DL-LIN52$^{12\text{-}34;P29A;phosS28}$ structure. The stronger electron density shows the presence of additional residues C-terminal to P29 in LIN52 that form a single turn of an a-helix. W32 in LIN52 fits into a pocket in p107DL formed by E863, M865, R869, and Y879. In addition to van der Waals contacts between the hydrophobic sidechains, R869 is positioned to make a cation-pi interaction with the tryptophan ring, and there is a hydrogen bond between the tryptophan indole hydrogen and the sidechain of E863. We note that the glutamate at this position in p107 is an asparagine in p130 but is a lysine in Rb, so this interaction may be another source of specificity of p107/p130 in DREAM. Given the conservation of W32 and the binding residues in p107, we believe these interactions also take place in wild-type LIN52, but the presence of the proline weakens the affinity of the overall association. The reasons for the tighter affinity of the A29 mutant compared to the P29 wild-type are not certain considering that prolines are commonly found in the first turn of helices.

A

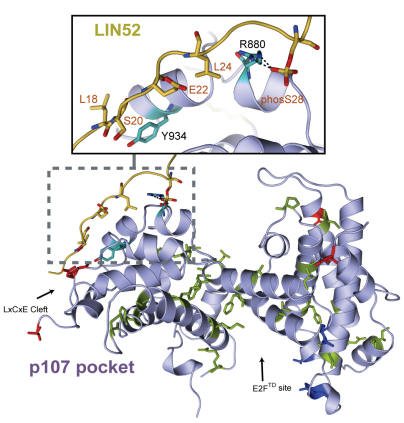

B

Mutation	Structural position	Possible outcome
Q392K	Surface	Unknown
I413T	Internal	Loss of hydrophobic interactions in core; protein destabilized
N422S	Internal	Loss of helix capping hydrogen bond; protein destabilized
I427F	Internal	Disrupt hydrophobic packing in core; protein destabilized
C439Y	Internal	Disrupt hydrophobic packing in core; protein destabilized
Q440E	Surface	Unknown
M476I	Internal	Loss of hydrophobic interactions in core; protein destabilized
R481Q	E2F Interface	Loss of E2F affinity
V490I	E2F Interface	Loss of E2F affinity
H498N	Internal	Loss of internal hydrogen bonds; protein destabilized
I508S	Internal	Loss of hydrophobic interactions in core; protein destabilized
P516L	Internal	Disrupt hydrophobic packing in core; protein destabilized
F531L	Internal	Loss of hydrophobic interactions in core; protein destabilized
R542C/H/S	E2F Interface	Loss of E2F affinity
E545D	Surface	Unknown
I558T	Internal	Loss of hydrophobic interactions in core; protein destabilized
W568C	Internal	Loss of hydrophobic interactions in core; protein destabilized
D571N	Internal	Loss of salt bridge stabilizing turn; protein destabilized
R784I	Internal	Loss of internal hydrogen bonds; protein destabilized
K794N	Internal	Loss of internal salt bridge; protein destabilized
R802C	Internal	Loss of internal salt bridge; protein destabilized
C807Y	Internal	Disrupt hydrophobic packing in core; protein destabilized
R817Q	Internal	Loss of internal hydrogen bonds; protein destabilized
F826L	Internal	Loss of aromatic stacking interactions; protein destabilized
D837G	Internal	Loss of internal salt bridge; protein destabilized
R838S	Internal	Loss of internal hydrogen bonds; protein destabilized
R859I	Surface	Unknown
R880I	LIN52 Interface	Loss of phosphate binding interaction; LIN52 affinity loss
Y934C	LIN52 Interface	Loss of hydrogen bond; LIN52 affinity loss
D950N	Internal	Loss of internal hydrogen bonds; protein destabilized
A952V	Surface	Unknown

C

p107ΔL	LIN52$^{12\text{-}34;phosS28}$ K_d
WT	1.4 ± 0.9 μM
R880I	6.3 ± 0.4 μM
Y934C	3.3 ± 0.3 μM

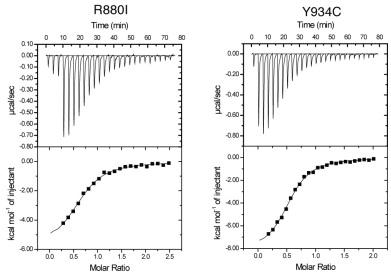

Figure 2.9. Location of missense mutations in p107 that occur in human cancer. **(**A) Mutations catalogued in the cBioPortal in the cBioPortal for Cancer Genomics are rendered in stick representation and are colored according to whether they are on the surface (red), internal (green), at the E2F interface (blue), or the LIN52 interface (cyan). (B) Table of mutations and their predicted biochemical effects. (C) Isothermal titration calorimetry measurements of the affinity of LIN52$^{12\text{-}34;phosS28}$ for p107DL with mutations at the LIN52 interface. The ITC data for the R880I and Y934C mutants are shown here, and the data for wild-type p107DL are shown in Figure 2.9 A.

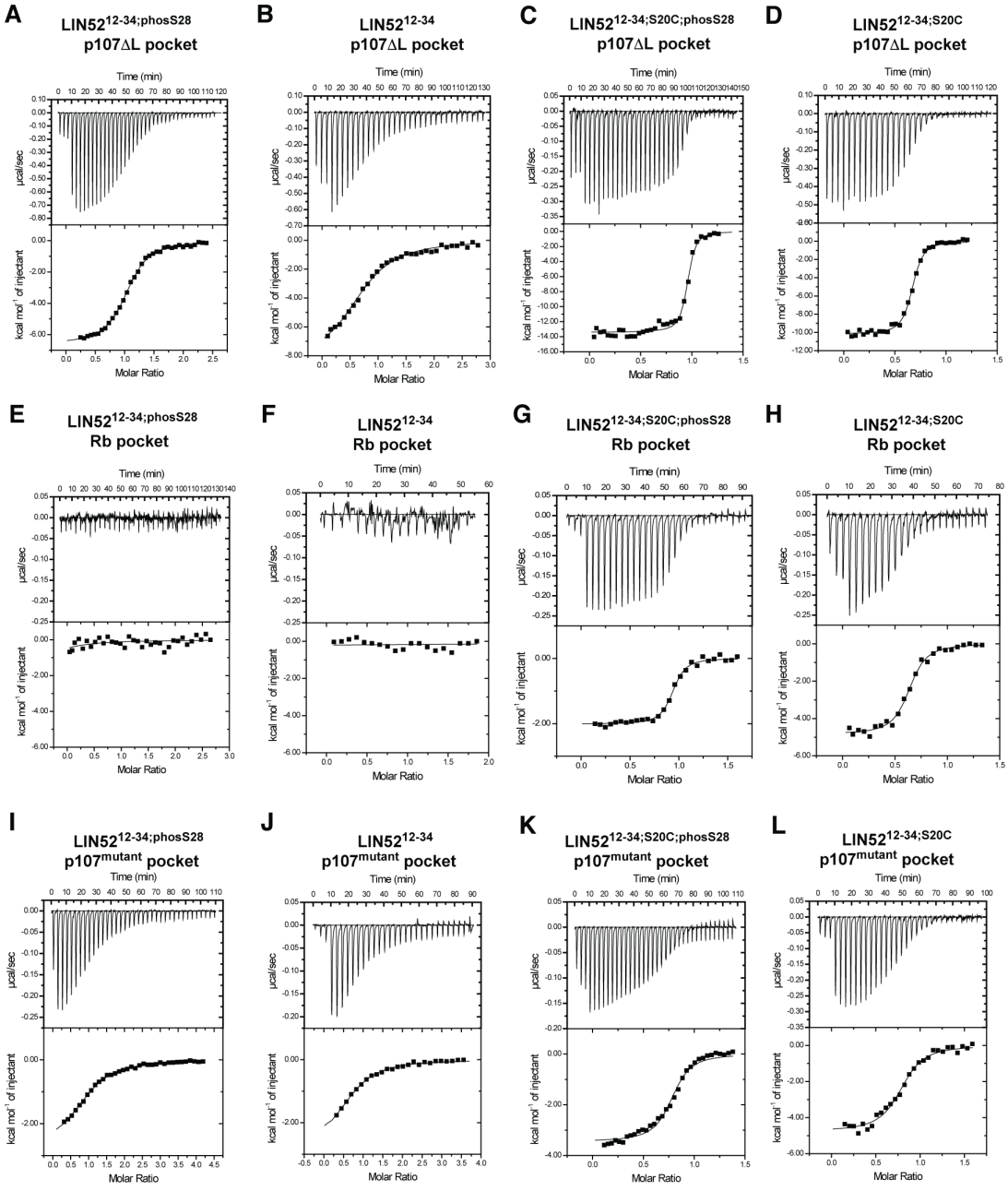
A
LIN52^12-34;phosS28
p107ΔL pocket
B
LIN52^12-34
p107ΔL pocket
C
LIN52^12-34;S20C;phosS28
p107ΔL pocket
D
LIN52^12-34;S20C
p107ΔL pocket
E
LIN52^12-34;phosS28
Rb pocket
F
LIN52^12-34
Rb pocket
G
LIN52^12-34;S20C;phosS28
Rb pocket
H
LIN52^12-34;S20C
Rb pocket
I
LIN52^12-34;phosS28
p107^mutant pocket
J
LIN52^12-34
p107^mutant pocket
K
LIN52^12-34;S20C;phosS28
p107^mutant pocket
L
LIN52^12-34;S20C
p107^mutant pocket
Time (min)
µcal/sec
kcal mol⁻¹ of injectant
Molar Ratio

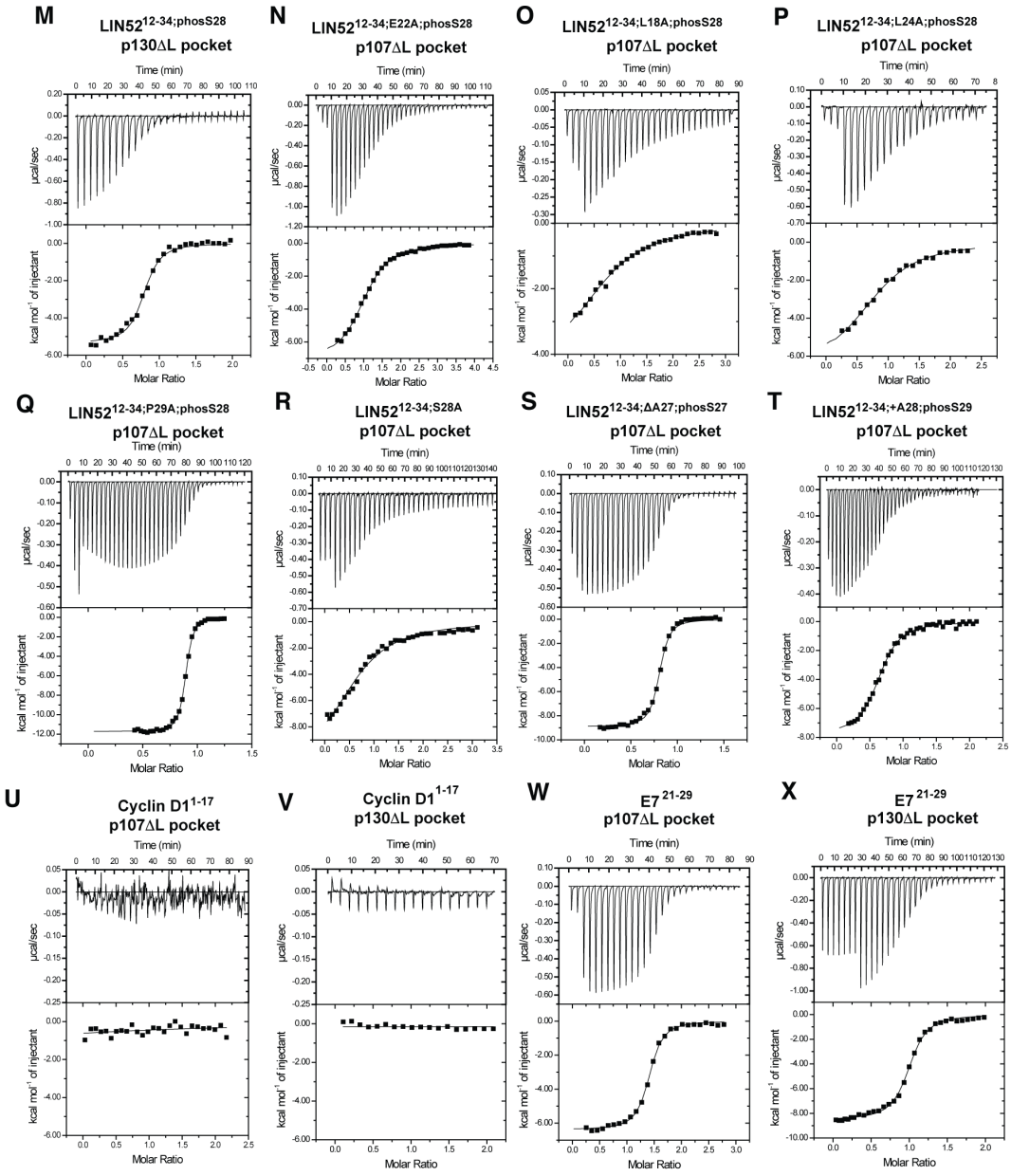
M
LIN52^12-34;phosS28
p130ΔL pocket
N
LIN52^12-34;E22A;phosS28
p107ΔL pocket
O
LIN52^12-34;L18A;phosS28
p107ΔL pocket
P
LIN52^12-34;L24A;phosS28
p107ΔL pocket
Q
LIN52^12-34;P29A;phosS28
p107ΔL pocket
R
LIN52^12-34;S28A
p107ΔL pocket
S
LIN52^12-34;ΔA27;phosS27
p107ΔL pocket
T
LIN52^12-34;+A28;phosS29
p107ΔL pocket
U
Cyclin D1^1-17
p107ΔL pocket
V
Cyclin D1^1-17
p130ΔL pocket
W
E7^21-29
p107ΔL pocket
X
E7^21-29
p130ΔL pocket
Time (min)
µcal/sec
kcal mol-1 of injectant
Molar Ratio

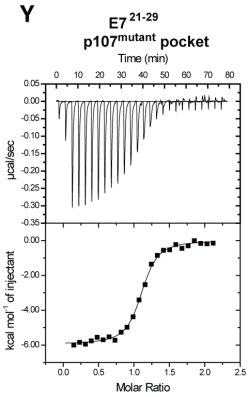

Figure 2.10. Representative isothermal titration calorimetry data.

2.4 Materials and Methods

2.4.1 Protein expression, purification, and phosphorylation

Human Rb pocket with its loop deleted (residues N380-G581; K643-R787), p107 pocket (T391-Q972), p107DL (T391-T599; N780-I887; K924-Q972) and p130 DL (H424-D632; N828-K935; E999-Q1049) were expressed and purified from E. coli BL21 cells as GST fusion proteins. Cells were induced with 1 mM IPTG and grown overnight at 20°C. Lysates were first purified by GS4B affinity chromatography. The elution fraction was then subjected to TEV protease cleavage and dialyzed overnight in 25 mM Tris, 200mM NaCl, 1 mM DTT, 0.5 mM EDTA pH 8.0. The protein was then passed over GS4B affinity resin again to remove free GST, concentrated, and stored in a buffer containing 20 mM Tris, 200mM NaCl, 1 mM DTT, and 20% glycerol pH 8.0.

LIN52, LIN37, RBBP48, LIN9, B-Myb and full-length p130 were expressed and purified from Sf9 cells (Expression Systems, Davis CA) using baculovirus vectors. Proteins were purified as described above, and the GST-free samples were passed over a Superdex-200 column that was equilibrated in the dialysis buffer following TEV cleavage. p130 was phosphatase treated with 1% lambda phosphatase by mass using the manufacturer protocol (New England Biolabs). Cdk2 treatment was performed as described (Burke et al. 2010), except the Cdk2 activator Speedy was used instead of a Cyclin activator. Following treatment, GST-p130 was separated from the enzymes using a Superdex 200 column.

The LIN52$^{12\text{-}34;phosS28}$ and E7$^{21\text{-}29}$ peptides used for crystallization were synthesized by BioPeptide LLC., San Diego CA. The LIN52$^{12\text{-}34;P29A;phosS28}$ peptide and all other peptides used for ITC and the FP assay were synthesized by GenScript Inc. Piscataway NJ.

2.4.2 Isothermal Titration Calorimetry

Proteins were prepared for ITC by dialyzing overnight at 4°C in a buffer containing 100 mM NaCl, 20 mM Tris-HCl, and 1mM beta-mercaptoethanol (pH 8.0). Using a Micro-Cal VP-ITC

calorimeter, typical binding experiments involved injecting 0.5-1 mM peptide into a 20-40 mM solution of p107 or Rb at 25°C. Binding constants were generated by fitting the data to a one-site binding model using Origin software. The error associated with the reported dissociation constants reflect the standard deviation calculated from 2-4 separate binding experiments.

2.4.3 Immunoprecipitation and Western Blotting

Immunoprecipitation was carried out as previously described (Cecchini and Dick, 2011). To generate extracts C33A cells were plated at $6x10^6$ cells per 15 cm plate and transfected with 40µg of either CMV-FLAG-$p107^{WT}$ or CMV-FLAG-$p107^{6x\text{-}FL}$, 20µg of either CMV-HA-E2F2 or CMV-HA-E2F4 and 20µg CMV-HA-DP1. Extracts were then normalized for transfection efficiency and immunoprecipitated using anti-FLAG M2 (Sigma). Immunoblotting was carried out using anti-FLAG M2 (Sigma) and anti-HA 3F10 (Roche).

2.4.4 Luciferase Reporter Assays

AOS2 cells were plated at $7.5x10^5$ cells per well in a six well plate and transfected 24h later. Cells were transfected in triplicate with Fugene HD according to manufacturer's instructions (Fugene HD + 100µl DMEM). All transfections included the following: 100ng of pE2F4B-Luc reporter plasmid, 200ng CMV-βGal, 15 ng of CMV-HA-E2F2, and 15ng of CMV-HA-DP1. E2F-repression assays also included either 0, 50 ng, 100 ng, 150 ng, or 200 ng of CMV-FLAG-$p107^{WT}$ or CMV-FLAG-$p107^{6x\text{-}FL}$. CMV-CD20 was added to normalize p107 and CD20 plasmids to 200ng. Luciferase and βGal assays were performed as previously described (Dick et al. 2000), and luciferase activity was normalized to βGal from the same transfected extract.

2.4.5 Crystallization, data collection, structure determination, and model refinement

p107DL was prepared for crystallization by elution from a Superdex 75 (GE Healthcare) column in a buffer containing 25 mM Tris, 500 mM NaCl, and 5 mM DTT, pH 8.0. LIN52$^{12\text{-}34;phosS28}$ was added in 3-fold molar excess to 14 mg/mL p107DL, and E7$^{21\text{-}29}$ was added in 2-fold molar excess to 12 mg/mL p107DL. After incubation on ice for 30 minutes, both complexes were crystallized by sitting-drop vapor diffusion at 4°C. Plates formed after two weeks in 100 mM MES pH 6.5, 1.6 M $(NH_4)_2SO_4$, and 4% PEG 400 for the LIN52$^{12\text{-}34;phosS28}$ complex and in 100 mM HEPES pH 7.5, 1.7 M $(NH_4)_2SO_4$, and 4% PEG 400 for the E7$^{21\text{-}29}$ complex. Crystals were frozen in the proper well buffer with 20% ethylene glycol. Some crystals containing the LIN52$^{12\text{-}34;phosS28}$ peptide were soaked with 20-fold molar excess of the P29A mutant peptide before freezing.

Data were collected at the Advanced Photon Source, Argonne National Laboratory at Beamline 23-IDB. Diffraction spots were integrated using MOSFLM (Leslie 2006), and data were merged and scaled using Scala (Bailey 1994). Phases were first solved for the E7$^{21\text{-}29}$ complex by molecular replacement using PHASER (Mccoy et al. 2007). A homology model of p107DL, which was constructed using the Rb pocket domain (PDB code: 3POM), was used as a search model. p107DL complexes with LIN52 peptides were then solved using the E7-p107 complex as a search model as the crystal form was slightly different. Peptides were built with Coot (Emsley and Cowtan 2004), and the models were refined with Phenix (Adams et al. 2010). Coordinates and structure factors have been deposited in the PDB for the structures with the E7$^{21\text{-}29}$, LIN52$^{12\text{-}34;phosS28}$, and LIN52$^{12\text{-}34;P29A;phosS28}$ peptides under accession codes 4YOZ, 4YOS, and 4YOO, respectively.

2.4.6 Fluorescence Polarization Assay

TMR-LIN52$^{12\text{-}34;phosS28}$ was mixed at 10 nM with p130DL GST-p130 in a buffer containing 40 mM Tris, 150 mM NaCl, 1 mM DTT, 0.1% Tween, pH 8.0. 20 mL of the

reaction was used for the measurement in a 384-well plate well. FP measurements were made in triplicate using a Perkin-Elmer EnVision plate reader, and reported FP values were determined using instrument software. Error bars in the plots show standard deviations for the three measurements of each point, while the reported errors in K_d and K_I are errors derived from curve fits. We note that absolute K_d measurements were typically tighter using the FP assay compared to ITC and suggest that this difference may be due to the presence of the dye in the peptide or other subtle differences in experimental conditions.

2.5 References

Adams PD, Afonine PV, Bunkoczi G, Chen VB, Davis IW, Echols N, Headd JJ, Hung LW, Kapral GJ, Grosse-Kunstleve RW et al. 2010. PHENIX: a comprehensive Python-based system for macromolecular structure solution. *Acta Crystallogr D Biol Crystallogr* **66**: 213-221.

Andrejka L, Wen H, Ashton J, Grant M, Iori K, Wang A, Manak JR, Lipsick JS. 2011. Animal-specific C-terminal domain links myeloblastosis oncoprotein (Myb) to an ancient repressor complex. *Proc Natl Acad Sci U S A* **108**: 17438-17443.

Bailey S. 1994. The Ccp4 Suite - Programs for Protein Crystallography. *Acta Crystallographica Section D-Biological Crystallography* **50**: 760-763.

Balog ER, Burke JR, Hura GL, Rubin SM. 2011. Crystal structure of the unliganded retinoblastoma protein pocket domain. *Proteins* **79**: 2010-2014.

Boichuk S, Parry JA, Makielski KR, Litovchick L, Baron JL, Zewe JP, Wozniak A, Mehalek KR, Korzeniewski N, Seneviratne DS et al. 2013. The DREAM complex mediates GIST cell quiescence and is a novel therapeutic target to enhance imatinib-induced apoptosis. *Cancer Res* **73**: 5120-5129.

Burke JR, Deshong AJ, Pelton JG, Rubin SM. 2010. Phosphorylation-induced conformational changes in the retinoblastoma protein inhibit E2F transactivation domain binding. *J Biol Chem* **285**: 16286-16293.

Burke JR, Hura GL, Rubin SM. 2012. Structures of inactive retinoblastoma protein reveal multiple mechanisms for cell cycle control. *Genes Dev* **26**: 1156-1166.

Canhoto AJ, Chestukhin A, Litovchick L, DeCaprio JA. 2000. Phosphorylation of the retinoblastoma-related protein p130 in growth-arrested cells. *Oncogene* **19**: 5116-5122.

Cobrinik D. 2005. Pocket proteins and cell cycle control. *Oncogene* **24**: 2796-2809.

Dannenberg JH, Schuijff L, Dekker M, van der Valk M, te Riele H. 2004. Tissue-specific tumor suppressor activity of retinoblastoma gene homologs p107 and p130. *Genes Dev* **18**: 2952-2962.

Dick FA, Rubin SM. 2013. Molecular mechanisms underlying RB protein function. *Nat Rev Mol Cell Biol* **14**: 297-306.

Dowdy SF, Hinds PW, Louie K, Reed SI, Arnold A, Weinberg RA. 1993. Physical interaction of the retinoblastoma protein with human D cyclins. *Cell* **73**: 499-511.

Emsley P, Cowtan K. 2004. Coot: model-building tools for molecular graphics. *Acta Crystallogr D Biol Crystallogr* **60**: 2126-2132.

Farkas T, Hansen K, Holm K, Lukas J, Bartek J. 2002. Distinct phosphorylation events regulate p130- and p107-mediated repression of E2F-4. *J Biol Chem* **277**: 26741-26752.

Fera D, Schultz DC, Hodawadekar S, Reichman M, Donover PS, Melvin J, Troutman S, Kissil JL, Huryn DM, Marmorstein R. 2012. Identification and characterization of small molecule antagonists of pRb inactivation by viral oncoproteins. *Chem Biol* **19**: 518-528.

Forristal C, Henley SA, MacDonald JI, Bush JR, Ort C, Passos DT, Talluri S, Ishak CA, Thwaites MJ, Norley CJ et al. 2014. Loss of the Mammalian DREAM Complex Deregulates Chondrocyte Proliferation. *Mol Cell Biol* **34**: 2221-2234.

Gagrica S, Hauser S, Kolfschoten I, Osterloh L, Agami R, Gaubatz S. 2004. Inhibition of oncogenic transformation by mammalian Lin-9, a pRB-associated protein. *EMBO J* **23**: 4627-4638.

Gao J, Aksoy BA, Dogrusoz U, Dresdner G, Gross B, Sumer SO, Sun Y, Jacobsen A, Sinha R, Larsson E et al. 2013. Integrative analysis of complex cancer genomics and clinical profiles using the cBioPortal. *Sci Signal* **6**: pl1.

Georlette D, Ahn S, MacAlpine DM, Cheung E, Lewis PW, Beall EL, Bell SP, Speed T, Manak JR, Botchan MR. 2007. Genomic profiling and expression studies reveal both positive and negative activities for the Drosophila Myb MuvB/dREAM complex in proliferating cells. *Genes Dev* **21**: 2880-2896.

Harrison MM, Ceol CJ, Lu X, Horvitz HR. 2006. Some C. elegans class B synthetic multivulva proteins encode a conserved LIN-35 Rb-containing complex distinct from a NuRD-like complex. *Proc Natl Acad Sci U S A* **103**: 16782-16787.

Henley SA, Dick FA. 2012. The retinoblastoma family of proteins and their regulatory functions in the mammalian cell division cycle. *Cell Div* **7**: 10.

Jones RE, Wegrzyn RJ, Patrick DR, Balishin NL, Vuocolo GA, Riemen MW, Defeo-Jones D, Garsky VM, Heimbrook DC, Oliff A. 1990. Identification of HPV-16 E7 peptides that are potent antagonists of E7 binding to the retinoblastoma suppressor protein. *J Biol Chem* **265**: 12782-12785.

Korenjak M, Taylor-Harding B, Binne UK, Satterlee JS, Stevaux O, Aasland R, White-Cooper H, Dyson N, Brehm A. 2004. Native E2F/RBF complexes contain Myb-interacting proteins and repress transcription of developmentally controlled E2F target genes. *Cell* **119**: 181-193.

Lee C, Chang JH, Lee HS, Cho Y. 2002. Structural basis for the recognition of the E2F transactivation domain by the retinoblastoma tumor suppressor. *Genes Dev* **16**: 3199-3212.

Lee JO, Russo AA, Pavletich NP. 1998. Structure of the retinoblastoma tumour-suppressor pocket domain bound to a peptide from HPV E7. *Nature* **391**: 859-865.

Leslie AG. 2006. The integration of macromolecular diffraction data. *Acta Crystallogr D Biol Crystallogr* **62**: 48-57.

Lewis PW, Beall EL, Fleischer TC, Georlette D, Link AJ, Botchan MR. 2004. Identification of a Drosophila Myb-E2F2/RBF transcriptional repressor complex. *Genes Dev* **18**: 2929-2940.

Litovchick L, Florens LA, Swanson SK, Washburn MP, DeCaprio JA. 2011. DYRK1A protein kinase promotes quiescence and senescence through DREAM complex assembly. *Genes Dev* **25**: 801-813.

Litovchick L, Sadasivam S, Florens L, Zhu X, Swanson SK, Velmurugan S, Chen R, Washburn MP, Liu XS, DeCaprio JA. 2007. Evolutionarily conserved multisubunit RBL2/p130 and E2F4 protein complex represses human cell cycle-dependent genes in quiescence. *Mol Cell* **26**: 539-551.

Mccoy AJ, Grosse-Kunstleve RW, Adams PD, Winn MD, Storoni LC, Read RJ. 2007. Phaser crystallographic software. *J Appl Crystallogr* **40**: 658-674.

Morris EJ, Dyson NJ. 2001. Retinoblastoma protein partners. *Adv Cancer Res* **82**: 1-54.

Muller GA, Quaas M, Schumann M, Krause E, Padi M, Fischer M, Litovchick L, DeCaprio JA, Engeland K. 2012. The CHR promoter element controls cell cycle-dependent gene transcription and binds the DREAM and MMB complexes. *Nucleic Acids Res* **40**: 1561-1578.

Nor Rashid N, Yusof R, Watson RJ. 2011. Disruption of repressive p130-DREAM complexes by human papillomavirus 16 E6/E7 oncoproteins is required for cell-cycle progression in cervical cancer cells. *J Gen Virol* **92**: 2620-2627.

Obenauer JC, Cantley LC, Yaffe MB. 2003. Scansite 2.0: Proteome-wide prediction of cell signaling interactions using short sequence motifs. *Nucleic Acids Res* **31**: 3635-3641.

Pilkinton M, Sandoval R, Colamonici OR. 2007. Mammalian Mip/LIN-9 interacts with either the p107, p130/E2F4 repressor complex or B-Myb in a cell cycle-phase-dependent context distinct from the Drosophila dREAM complex. *Oncogene* **26**: 7535-7543.

Reichert N, Wurster S, Ulrich T, Schmitt K, Hauser S, Probst L, Gotz R, Ceteci F, Moll R, Rapp U et al. 2010. Lin9, a subunit of the mammalian DREAM complex, is essential

for embryonic development, for survival of adult mice, and for tumor suppression. *Mol Cell Biol* **30**: 2896-2908.

Rubin SM. 2013. Deciphering the retinoblastoma protein phosphorylation code. *Trends Biochem Sci* **38**: 12-19.

Rubin SM, Gall AL, Zheng N, Pavletich NP. 2005. Structure of the Rb C-terminal domain bound to E2F1-DP1: a mechanism for phosphorylation-induced E2F release. *Cell* **123**: 1093-1106.

Sadasivam S, DeCaprio JA. 2013. The DREAM complex: master coordinator of cell cycle-dependent gene expression. *Nat Rev Cancer* **13**: 585-595.

Sadasivam S, Duan S, DeCaprio JA. 2012. The MuvB complex sequentially recruits B-Myb and FoxM1 to promote mitotic gene expression. *Genes Dev* **26**: 474-489.

Schmit F, Korenjak M, Mannefeld M, Schmitt K, Franke C, von Eyss B, Gagrica S, Hanel F, Brehm A, Gaubatz S. 2007. LINC, a human complex that is related to pRB-containing complexes in invertebrates regulates the expression of G2/M genes. *Cell Cycle* **6**: 1903-1913.

Singh M, Krajewski M, Mikolajka A, Holak TA. 2005. Molecular determinants for the complex formation between the retinoblastoma protein and LXCXE sequences. *J Biol Chem* **280**: 37868-37876.

Smith EJ, Leone G, DeGregori J, Jakoi L, Nevins JR. 1996. The accumulation of an E2F-p130 transcriptional repressor distinguishes a G0 cell state from a G1 cell state. *Mol Cell Biol* **16**: 6965-6976.

Ubersax JA, Ferrell JE, Jr. 2007. Mechanisms of specificity in protein phosphorylation. *Nat Rev Mol Cell Biol* **8**: 530-541.

van den Heuvel S, Dyson NJ. 2008. Conserved functions of the pRB and E2F families. *Nat Rev Mol Cell Biol* **9**: 713-724.

Wen H, Andrejka L, Ashton J, Karess R, Lipsick JS. 2008. Epigenetic regulation of gene expression by Drosophila Myb and E2F2-RBF via the Myb-MuvB/dREAM complex. *Genes Dev* **22**: 601-614.

Wirt SE, Sage J. 2010. p107 in the public eye: an Rb understudy and more. *Cell Div* **5**: 9.

Xiao B, Spencer J, Clements A, Ali-Khan N, Mittnacht S, Broceno C, Burghammer M, Perrakis A, Marmorstein R, Gamblin SJ. 2003. Crystal structure of the retinoblastoma tumor suppressor protein bound to E2F and the molecular basis of its regulation. *Proc Natl Acad Sci U S A* **100**: 2363-2368.

Chapter 3: Structural mechanism of Myb-MuvB assembly

3.1 Introduction

There are three paralogous *MYB* genes in vertebrates that code for transcription factors: *MYB* (c-Myb), *MYBL1* (A-Myb) and *MYBL2* (B-Myb). *MYB* and *MYBL1* are involved in recurrent chromosomal translocations in human leukemia, adenoid cystic carcinoma, and pediatric glioma (Ramsay and Gonda 2008; Bandopadhayay et al. 2016; Ferrarotto et al. 2016). Increased levels of *MYBL2* expression have been observed in breast cancer and are a predictor of poor prognosis (Musa et al. 2017). Consistent with an essential role in proliferation, B-Myb is present in all mitotically cycling cells (Sala 2005), and *MYBL2* germline knockout mice display an early embryonic lethal phenotype (Tanaka et al. 1999). In contrast, c-Myb and A-Myb appear to be tissue and cell type-specific (Mucenski et al. 1991; Toscani et al. 1997).

The Myb protein architecture contains a DNA-binding domain, a transactivation domain, and a negative regulatory domain (NRD) (**Fig. 3.1**). The C-terminus has been referred to as the NRD because deletion of this region in all three Myb proteins promotes the activation of Myb-regulated genes in cell-based reporter assays (Sakura et al. 1989; Dubendorff et al. 1992; Takahashi et al. 1995; Lane et al. 1997). In human leukemia, adenoid cystic carcinoma, and pediatric glioma, chromosomal rearrangements create fusion proteins with truncations of the C-terminus of c-Myb or A-Myb that remove the NRD and result in increased Myb target gene expression (Ramsay and Gonda 2008; Bandopadhayay et al. 2016; Ferrarotto et al. 2016). The NRD is also absent in the transforming avian oncogene *v-MYB*, and deletion of the C-terminus of c-Myb, in a fashion similar to v-Myb, is sufficient for oncogenic activation (Ramsay and Gonda 2008).

Other evidence suggests that the C-terminus of B-Myb primarily plays an activating role. Unlike the other family members, C-terminal truncation of the *MYBL2* gene in human cancers has not been reported. The C-terminus of human B-Myb has been observed to enhance

transcriptional activation when fused to c-Myb (Oh and Reddy 1998). Moreover, the C-terminus of *Drosophila* Myb (dMyb), an ortholog of B-Myb, is essential for association with the MuvB complex and mutations in this region abolish its activity (Wen et al. 2008; Andrejka et al. 2011). These results suggest that part of the NRD may have some activating function related to Myb-MuvB (MMB) complex assembly, but further structure-function analysis of this domain is needed.

The MuvB complex cooperates with B-Myb during S-phase of the cell cycle to activate mitotic genes (Litovchick et al. 2007; Sadasivam et al. 2012). Cells require the MuvB complex and B-Myb or dMyb to undergo mitosis, as disruption of the Myb-MuvB (MMB) complex results in abnormal spindle assembly (Wen et al. 2008; Reichert et al. 2010; Andrejka et al. 2011; Sadasivam et al. 2012). Essential G2/M cell-cycle genes activated by MMB contain a cell-cycle homology region (CHR) DNA element in their promoters (Litovchick et al. 2007; Pilkinton et al. 2007; Sadasivam et al. 2012; Muller et al. 2014). The MuvB complex is assembled from five core proteins RBAP48, LIN54, LIN52, LIN37, and LIN9 (Beall et al. 2002; Lewis et al. 2004). This MuvB core binds the retinoblastoma protein paralog p130 and the transcription factor E2F4/5-DP1/2 to form the DREAM complex, which represses cell-cycle genes in quiescence and in G1 phase (Korenjak et al. 2004; Litovchick et al. 2007; Schmit et al. 2007). In S phase, MuvB dissociates from p130 and B-Myb binds to form MMB (Pilkinton et al. 2007; Sadasivam et al. 2012; Guiley et al. 2015). RBAP48 is a histone binding protein, and LIN54 directly binds the CHR DNA element in cell-cycle gene promoters (Marceau et al. 2016). LIN52 mediates MuvB association with p130 to form DREAM (Litovchick et al. 2011; Guiley et al. 2015). LIN9 and LIN37 have poorly characterized biochemical functions but are required for MuvB-regulated gene expression (Reichert et al. 2010; Mages et al. 2017).

These studies suggest that B-Myb function is linked to the MuvB complex and the CHR element, from which it can activate genes required for mitosis. Here we present the structure

of the C-terminus of B-Myb, and define its role as a MuvB-binding domain (MBD). We find that B-Myb assembles with the MuvB complex by accessing domains of LIN52 and LIN9 and that this interface mediates B-Myb recruitment to CHR promoters and B-Myb-stimulated cell proliferation. Our findings describe a conserved role for this MMB interface in cell-cycle progression and highlight a unique target for cancer therapeutics.

3.2 Results

3.2.1 Determinants for assembly of the Myb-MuvB complex

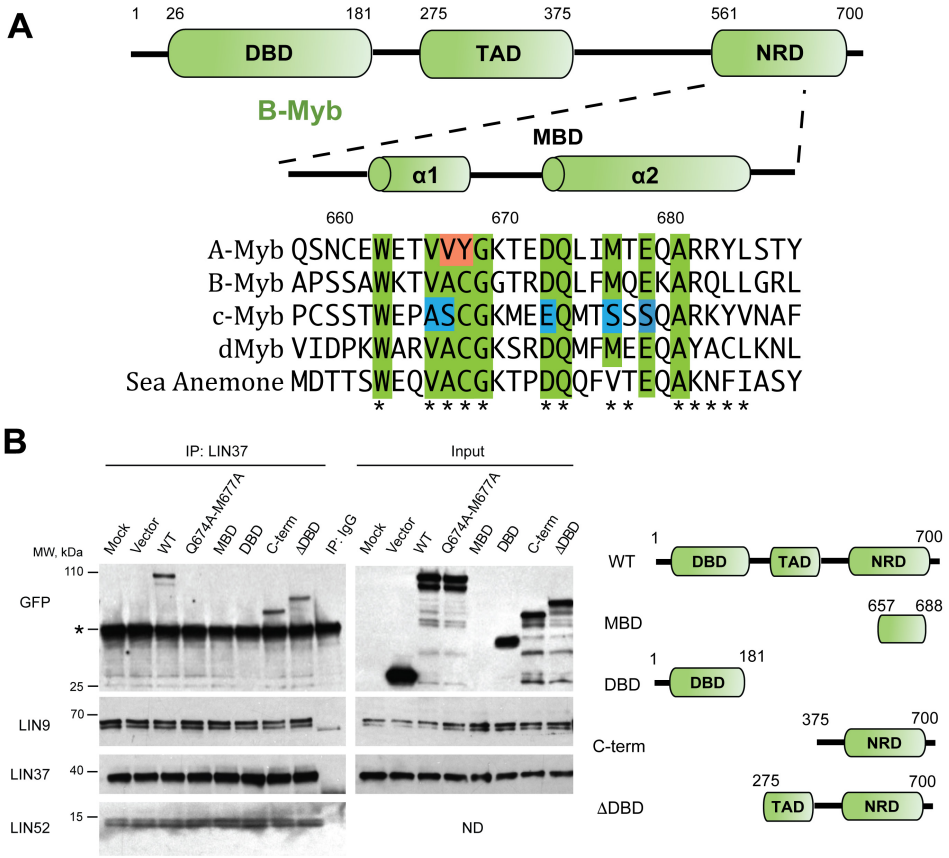

Figure 3.1 The B-Myb C-terminal domain is necessary and sufficient for MuvB association. (A) Domain architecture of Myb proteins (sequence numbering for human B-Myb), including a DNA-binding domain (DBD), transactivation domain (TAD), and a negative regulatory domain (NRD). The MuvB binding domain (MBD) investigated here is within the NRD and has the aligned sequence. The secondary structure and amino acids that interact with MuvB (asterisks) are determined from the crystal structure in this study. Amino acids that are identical in vertebrate B-Myb orthologs and Drosophila Myb (dMyb) are highlighted green, with changes at these positions in A-Myb and c-Myb shown in red and blue (**Fig. 2.6**). (B) T98G cells were transfected with plasmids encoding the indicated GFP-B-Myb fusion protein. Vector expresses GFP only. Lysates were immunoprecipitated with an anti-LIN37 antibody, and Western blots performed to assay the protein of interest. The asterisks mark immunoglobulin bands from the primary antibody.

We first identified the B-Myb domain requirements for human MMB complex assembly. Using co-immunoprecipitation assay (co-IP) in T98G cells, we found that the C-terminus of B-Myb (residues 375-700) is necessary and sufficient for association with LIN37 and other MuvB components (**Fig. 3.1**), which was similarly observed in *Drosophila* dMyb (Andrejka et al. 2011). Mutating the conserved residues Q674 and M677 was sufficient to disrupt MMB complex formation. Based on these data, the sequence conservation in the Myb C-terminus (**Fig. 3.1 and Fig. 3.6**), and our previous observation that B-Myb residues 654-700 are sufficient to bind recombinant MuvB (Guiley et al. 2015), we conclude that the C-terminus of B-Myb contains a MuvB-binding domain (MBD). A small fragment of the B-Myb C-terminus (**Fig. 3.1**, 657-688, hereafter called MBD) did not efficiently express in T98G cells, so we further explored its association with MuvB using recombinant proteins.

We reconstituted a minimal human MuvB complex *in vitro* by co-expressing five proteins in Sf9 cells (Guiley et al. 2015). This recombinant MuvB forms a stable complex with full-length recombinant B-Myb that co-elutes in size-exclusion chromatography **(Fig. 3.2**). To identify the critical MuvB domains for B-Myb association, we implemented a quantitative fluorescence polarization (FP) assay using a rhodamine-labeled synthetic MBD peptide (B-Myb residues 657-688). We found that the minimal MuvB complex binds the B-Myb MBD with high affinity (K_d = 1.2 ± 0.1 nM) (**Fig. 3.2**). LIN52 is necessary for MMB reconstitution (Guiley et al. 2015), but LIN52 alone bound MBD 150-fold weaker than the MuvB complex,

suggesting that additional MuvB proteins contribute to MBD association (**Fig. 3.2 and Fig. 3.7**). LIN9 is also required for MMB assembly in cells (Litovchick et al. 2007; Osterloh et al. 2007; Pilkinton et al. 2007). Although we could not express soluble recombinant LIN9 alone, we could purify a sub-complex including conserved regions in LIN9 (residues 349-466, LIN9$^{349-466}$) and the C-terminus of LIN52 (residues 52-116, LIN52$^{52-116}$) (**Fig. 3.8**). This sub-complex binds B-Myb MBD with similar affinity to MuvB (**Fig. 3.1 and Fig. 3.7),** suggesting that LIN9 and LIN52 form the binding interface that recruits B-Myb to the MuvB complex.

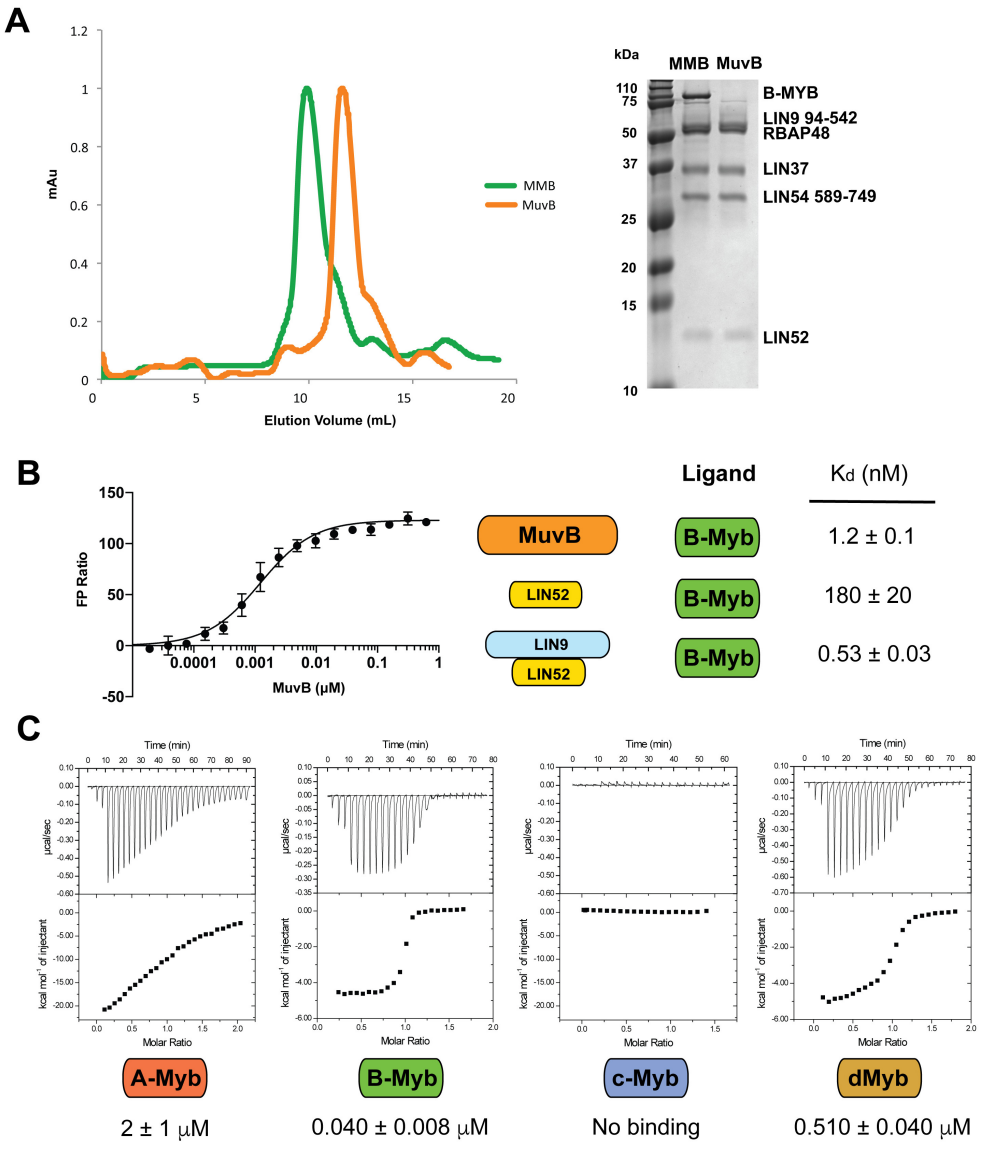

Figure 3.2 The Myb MuvB binding domain (MBD) directly binds LIN9 and LIN52. (A) Superdex 200 chromatograms and a Coomassie-stained SDS-PAGE gel showing proteins in the peak fractions. (B) FP measurements of the affinity of the indicted proteins. Data are shown for the labeled MBD peptide titrated with MuvB. (C) ITC binding measurements between LIN9$^{349-466}$-LIN52$^{52-116}$ and an MBD peptide from each indicated Myb protein. Additional raw data for FP and ITC measurements are shown in Fig. 3.8.

We assayed whether the A-Myb and c-Myb MBD sequences, which show some conservation with B-Myb (**Fig. 3.1 and Fig. 3.6**), could bind the LIN9$^{349-466}$-LIN52$^{52-116}$ sub-complex using isothermal titration calorimetry (ITC) (**Fig. 3.2**). The ITC measurement shows tight association of the B-Myb MBD, albeit with weaker affinity than in the FP assay. The A-Myb MBD associates with LIN9-LIN52 but with 50-fold weaker affinity than B-Myb, and the c-Myb MBD did not produce detectable binding (**Fig. 3.2**). The MBD sequence from *Drosophila (*dMyb), which is representative of the single Myb found in invertebrates (**Fig. 3.1 and Fig. 3.6**), binds human LIN9-LIN52 with 13-fold weaker affinity than B-Myb (**Fig. 3.2**). Alanine substitutions at M621 or Q618 in dMyb (equivalent to M677 and Q674 in B-Myb) result in loss of association in the ITC assay (**Fig. 3.7**).

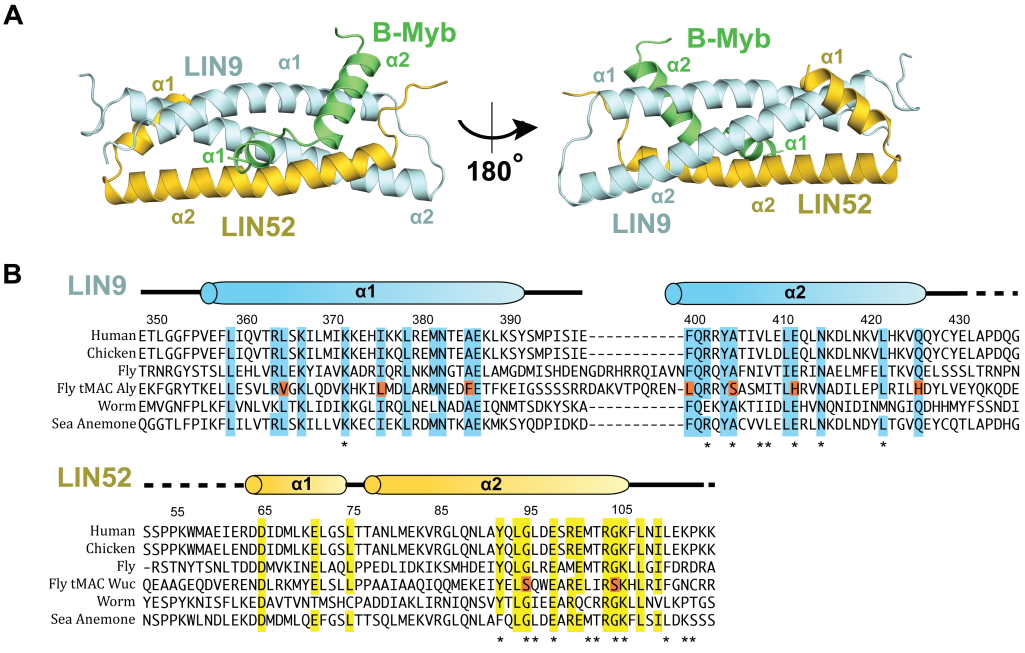

Figure 3.3 Crystal structure of the B-Myb MBD bound to the LIN9$^{349-466}$-LIN52$^{52-116}$ heterodimer. (A) Overall structure. B-Myb (green) binds the coiled-coil formed by LIN9 (cyan) and LIN52 (yellow). (B) Sequence alignments of LIN9 and LIN52 with secondary structure, conservation of primary sequence identity (colored boxes), and MBD-contacting residues (asterisks) indicated. Dashed lines are above sequences that were not included in the model due to a lack of electron density (LIN9 residues 432-466 were also not included). Substitutions in the tMAC paralogs at conserved positions in LIN9 and LIN52 are shaded orange.

3.2.2 Crystal structure reveals the Myb-MuvB interface

To resolve the molecular details of the MMB complex, we solved the crystal structure of B-Myb MBD bound to the LIN9$^{349-466}$-LIN52$^{52-116}$ sub-complex at 2.3 Å resolution (**Fig. 3.2, Table 3.1, and Fig. 3.9**). The LIN9-LIN52 heterodimer forms a three-stranded antiparallel coiled-coil as the core of the structure (**Fig. 3.3**). LIN9 contributes two helices (a1 and a2), which run antiparallel and are connected through a short linker. The third helix is from LIN52 (LIN52 a2) and is parallel with LIN9 a1. LIN52 contains a second shorter helix (a1) that covers a face of the coiled-coil near the N-termini of LIN9 a1 and LIN52 a2.

The B-Myb MBD forms two short helices that bind the coiled-coil surface formed by LIN9 a2 and LIN52 a2 (**Fig. 3.3**). The first MBD helix (MBD a1, residues 663-668) is comprised of a single turn with its axis pointing toward the center of the coiled-coil. B-Myb residues W663, V666, and A667, and C668, which are conserved in B-Myb (**Fig. 3.6**), make a number of van der Waals contacts with both LIN52 (A91, Y92, L96 and G95) and LIN9 (L418, N419, and L422) (**Fig. 3.4**). An alanine mutation of LIN52 at Y92, which inserts between B-Myb W663 and V666, reduces affinity of B-Myb 62-fold (**Fig. 3.4**). The sidechain of K372 in LIN9 a1, which is conserved in LIN9 orthologs (Fig. 3B), forms a hydrogen bond with the backbone carbonyl of A667 in B-Myb. The positive lysine likely stabilizes the negative C-terminal dipole of the MBD a1 helix (**Fig. 3.4**), and a LIN9 K372A mutation reduces B-Myb MBD affinity 6-fold (Fig. 4B). The close approach of MBD a1 to the core of the coiled-coil is possible because of the lack of a sidechain at G95 in LIN52. G95 is conserved in LIN52 (**Fig. 3.3**), and a G95S mutation reduces the affinity of the MBD 50-fold (**Fig. 3.4**).

A

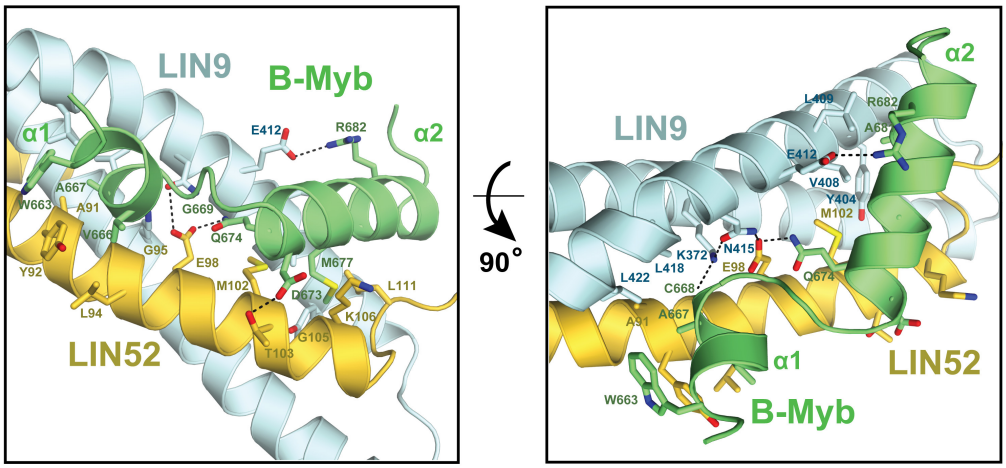

B

	LIN52	K_D (nM)	LIN9	K_D (nM)
	WT	0.52 ± 0.03	WT	0.52 ± 0.03
B-Myb α1 interactions	Y92A	32 ± 3	K372A	3.2 ± 0.3
	G95S	27 ± 3		
B-Myb α2 interactions	M102A	4.4 ± 0.2	V408A / L409A	82 ± 6
	K106A	7.2 ± 0.6	V408E	780 ± 60
	L111A	13.1 ± 0.9	E412A	8.5 ± 0.7
	G105E	36 ± 3	N415A	29 ± 3
	E98A	59 ± 5		
tMAC mutants	G105S	3.4 ± 0.3	A405S	2.3 ± 0.2

C

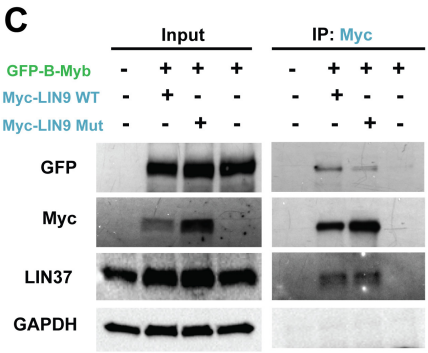

Figure 3.4 Interactions stabilizing the MBD interface with LIN9-LIN52. (A) Close-up view of interface in crystal structure. (B) FP measurements of B-Myb MBD binding affinities with $LIN9^{349-466}$-$LIN52^{52-116}$ containing the indicated mutation. Raw data are shown in Supplementary Fig. 3.2. (C) HeLa cells were transfected with plasmids encoding GFP-B-Myb and Myc-LIN9 fusion proteins as indicated. LIN9 Mut contains a V408A/L409A mutation. Lysates were immunoprecipitated with an anti-Myc antibody, and Western blots performed to assay the protein of interest. GAPDH is a loading control.

The second B-Myb MBD helix (a2) binds the N-terminus of LIN9 a2 and the C-terminus of LIN52 a2 (**Fig. 3.3 and Fig. 3.4**). This interface is primarily stabilized by interactions involving B-Myb residues Q674, M677, A681, R682, and L684 (**Fig. 3.4**). M677 docks into a hydrophobic pocket formed by M102, G105 and K106 in LIN52 and Y404 and V408 in LIN9, while A681 contacts L111 in LIN52 and A405, V408, and L409 in LIN9. R682 in MBD a2 makes a salt bridge with E412 in LIN9. We tested substitutions of several of these interacting

residues in LIN9 and LIN52 using the ITC assay, and in each case found weaker MBD association (**Fig. 3.4**). We also found that full-length LIN9 containing a V408A/L409A mutation has weaker affinity for B-Myb, but not LIN37, in a co-IP assay in HeLa cells (**Fig. 3.4**).

Q674 in the B-Myb MBD is also buried at the interface with the LIN9-LIN52 dimer. The glutamine sidechain makes hydrogen bonds with the sidechains of E98 in LIN52 and N415 in LIN9 (**Fig. 3.4**). LIN9 N415 also hydrogen bonds and positions LIN9 K372 for stabilizing MBD a1, while LIN52 E98 also hydrogen bonds with the backbone amide of G669 in B-Myb. Together these four buried polar residues (B-Myb Q674, LIN9 K372 and N415, and LIN52 E98) form a hydrogen bond network that brings together all five helices in the coiled-coil and B-Myb (**Fig. 3.4**). A LIN52 E98A mutation and LIN9 N415A mutation reduce the MBD affinity 110-fold and 58-fold respectively, supporting the importance of these interactions (**Fig. 3.4**). We note that the structure of the MBD interface with MuvB also accounts for Myb mutations studied in *Drosophila* that were deleterious to its function (**Fig. 3.10**).

3.2.3 Conservation of the Myb-MuvB association

The molecular details revealed by the structure of the MBD-LIN9-LIN52 complex explain the preference of B-Myb over other Myb family members for MuvB. A large hydrophobic residue is conserved at the M677 position in B-Myb in vertebrates and Myb in simpler metazoans, whereas a serine is substituted in human c-Myb (**Fig. 3.1**). c-Myb, which does not bind LIN9-LIN52 (**Fig. 3.2**), also lacks critical interacting residues in the MBD a1 helix (V666 and A667 in B-Myb). A-Myb also contains differences in the MBD a1 helix, which may explain its weaker affinity for MuvB. dMyb does not contain R682 in a1, which makes the salt bridge with LIN9 E412, and it also binds human LIN9-LIN52 with weaker affinity than B-Myb.

The LIN9 and LIN52 residues that are involved in B-Myb binding are conserved among a wide range of metazoans, including *C. elegans,* which does not appear to possess an animal-specific Myb homolog (**Fig. 3.3**). While some of these residues are likely conserved in *C.*

elegans to maintain the structural integrity of the MuvB complex, it may be that this site recruits an additional factor. The *Drosophila* tMAC complex contains MuvB-like proteins that are specific to the testis (Beall et al. 2007; Doggett et al. 2011). The LIN9 paralog Aly (Always early), and the LIN52 paralog Wuc (Wake-up-call) have residue substitutions specifically at regions where B-Myb interacts in our crystal structure (**Fig. 3.3**). We found using the FP assay that several of these substitutions (G95S, G105S, and A405S) weaken B-Myb affinity (**Fig. 3.4**), consistent with previous observations that tMAC does not bind and functions independently of dMyb (Beall et al. 2007).

The three *MYB* genes in mammals display distinct phenotypes in knockout studies (Mucenski et al. 1991; Toscani et al. 1997; Tanaka et al. 1999), suggesting distinct functions. Phylogenetic analysis indicates that B-Myb is the most ancient vertebrate Myb family member, and only B-Myb can functionally complement the sole Myb in *Drosophila* (Davidson et al. 2005). We found here that dMyb binds LIN9-LIN52 (**Fig. 3.2**) and that many invertebrate Myb proteins contain the critical residues in the B-Myb MBD that contact MuvB. Consistent with these observations, expression of B-Myb but neither c-Myb nor A-Myb can partially rescue a *Drosophila MYB* null mutant (Davidson et al. 2005). Together these results support the idea that the cell-cycle role of B-Myb-MuvB association is among the most conserved functions of Myb but was lost in the more recently evolved vertebrate paralogs.

3.2.4 Critical structural roles for LIN9 and LIN52 in mediating MuvB function

We performed two assays in proliferating HeLa cells to test the consequences of disrupting the MBD-MuvB interface on B-Myb function. As previously described (Litovchick et al. 2007; Sadasivam et al. 2012), we found using chromatin imunnoprecipitation (ChIP) that B-Myb occupies the MMB-regulated *CCNB1* promoter but not the DREAM-regulated *RBL1* (p107) promoter (**Fig. 3.5**). Importantly, we observed that a Q674A/M677A mutation in B-Myb inhibits its recruitment to *CCNB1*. We also found that expression of wild-type B-Myb increased proliferation of HeLa cells compared to a Q674A/M677A B-Myb mutant (**Fig. 3.5**).

We conclude that MBD-MuvB association is critical in these cells for B-Myb recruitment to CHR promoters, which is likely mediated through MuvB association with the CHR site (Sadasivam et al. 2012; Marceau et al. 2016), and for B-Myb function in stimulating proliferation.

3.3 Discussion

We provide here the first evidence of a direct association between B-Myb, LIN9, and LIN52 via a ternary sub-complex in MMB. The LIN52 protein also mediates assembly of the repressive DREAM complex during quiescence and G1 when phosphorylated at serine 28 by DYRK1A (Litovchick et al. 2011; Guiley et al. 2015). These findings highlight the important role of LIN52 as an adaptor protein that binds either p130 (DREAM) or B-Myb (MMB) to form the proper complex for regulating gene expression at the right time in the cell cycle (**Fig. 3.5**). The LIN52 domain that binds B-Myb in our crystal structure does not overlap with the sequence that binds p130. This observation is consistent with our finding that B-Myb and p130 do not directly compete for MuvB association (Guiley et al. 2015) and the observation that dMyb and fly p130 orthologs co-purify in the same complex (Lewis et al. 2004; Korenjak et al. 2004). We propose that the interactions between p130 and B-Myb with LIN52 are mutually exclusive in human cells because of the timing of p130 phosphorylation and B-Myb expression. Pocket protein-E2F complexes, including DREAM, have been found to repress the *MYBL2* gene until cell-cycle entry (Lam and Watson 1993; Liu et al. 1996), and DREAM dissociation through Cdk phosphorylation of p130 occurs as B-Myb levels increase (Pilkinton et al. 2007; Guiley et al. 2015).

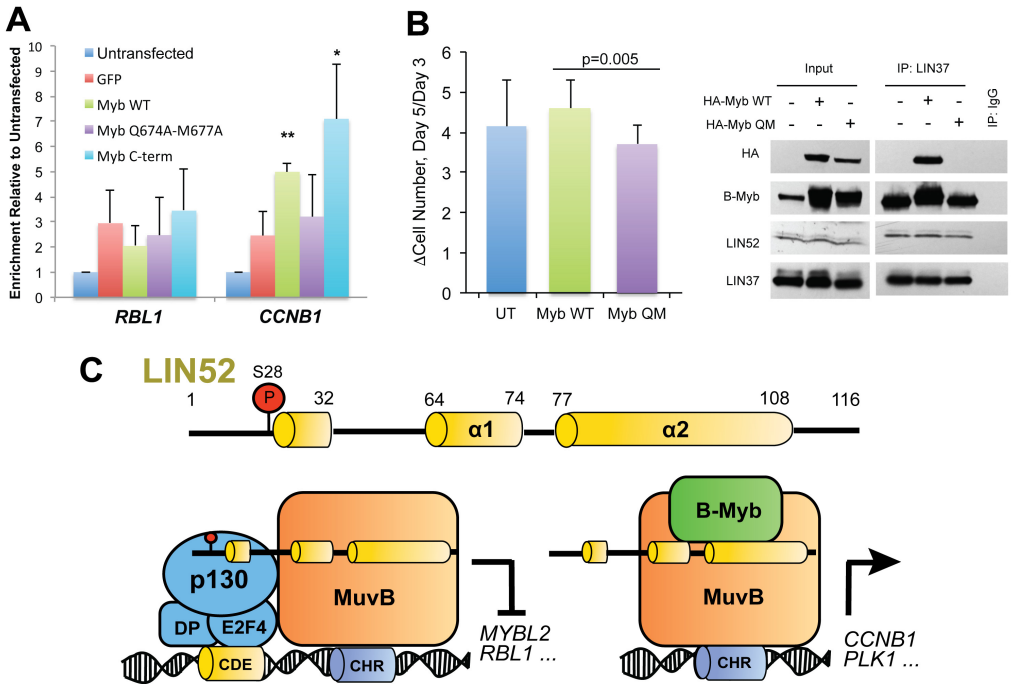

Figure 3.5 LIN52 is an adaptor protein that facilitates MuvB interactions with transcription factors. (A) Chromatin immunoprecipitation assay of transfected GFP-B-Myb and the indicated mutants in HeLa cells. Following crosslinking and immunoprecipitation with an anti-GFP antibody, qPCR was performed with primers specific to the *RBL1* and *CCNB1* promoters. The average promoter enrichment relative to untransfected cells is reported, and the error bars are standard deviations from three biological replicates. p-values were calculated for the promoter enrichment of the GFP-B-Myb fusion proteins relative to untransfected control using a two-tailed student's t-test (* $p < 0.05$, ** $p < 0.01$). (B) HeLa cells stably expressing HA-tagged wild-type or QM mutant (Q674A/M677A) B-Myb were counted at 3 and 5 days after plating. Graph shows average ± standard deviations from three biological replicates. The difference between the wild type (Myb WT) and the mutant (Myb QM)-expressing cells was statistically significant (student's t-test p=0.005). UT is untreated control. The co-IP assay confirms similar expression of the B-Myb variants and that the QM mutant B-Myb does not associate with MuvB. (C) LIN52 is an adaptor protein that facilitates DREAM and MMB assembly. (Top) Domain architecture of LIN52. S28 phosphorylation stimulates association of the LIN52 N-terminus with p130. The helices toward the C-terminus of LIN52 mediate B-Myb association. LIN52 recruits p130-E2F4-DP to form DREAM during G0/G1 (bottom left) and B-Myb to form MMB in S/G2 phase (bottom right), although the interactions are not mutually exclusive. The promoter elements that bind E2F4-DP (CDE) and MuvB (CHR) are shown.

Previous studies implicate both B-Myb/dMyb and LIN9 as essential for cell-cycle gene activation and progression through mitosis (Katzen et al. 1998; Tanaka et al. 1999; Zhu et al. 2004; Litovchick et al. 2007; Reichert et al. 2010; Sadasivam et al. 2012). Our data suggest that a critical activating function of LIN9 is the recruitment of B-Myb to CHR promoters via the MuvB complex. Similarly, the data suggest that the MBD is essential for B-Myb-mediated gene activation as the site of MuvB association (Osterloh et al. 2007; Andrejka et al. 2011). Interestingly, the C-terminus of Myb proteins, which includes the MBD, was previously considered to be part of a negative regulatory domain (Sakura et al. 1989; Dubendorff et al. 1992; Takahashi et al. 1995; Lane et al. 1997). The fact that oncogenic C-terminal truncations are exclusive to c-Myb and A-Myb, neither of which bind MuvB strongly, suggests that the C-terminal domain of those paralogs regulates transcription using additional mechanisms that are MuvB-independent.

The LIN9 and LIN52 helical bundle could serve as a therapeutic target in cancer cells that have high-levels of B-Myb expression. Decreased levels of either the MuvB complex protein LIN9 or B-Myb were effective in reducing cancer proliferation and tumor mass (Iltzsche et al. 2017; Wolter et al. 2017). Targeting this interface would disrupt the activator MMB complex and potentially restore the DREAM complex to promote quiescence and tumor dormancy (Litovchick et al. 2007; Litovchick et al. 2011). The structure of the Myb-LIN9-LIN52 interface presented here may benefit future efforts to design cell-cycle inhibitors that target the MMB complex.

Table 3.1. X-ray crystallography data collection and refinement statistics B-Myb-LIN9-LIN52.

	Native	**SeMet**
Data collection		
Space group	P 21	P 21
Cell dimensions		
a, b, c	60.8 30.8 105.4	61.2 31 105.4
α, β, γ	90, 99.9, 90	90, 99.9, 90
Resolution (Å)	59.9 – 2.3	60.3 – 2.6
R_{merge}	12.7(52.8)	20.9(107.4)
R_{pim}	5.2(21.8)	4.2(21.8)
Total reflections	106752(14701)	315076(36676)
Unique reflections	16249(2275)	12079(1444)
$CC_{1/2}$	0.99(0.89)	0.99(0.88)
I/σ	9.9 (3.3)	16.5 (3.5)
Completeness	94.9% (91.8%)	98.4% (98%)
Anomalous completeness	-	98.8(98.3)
Redundancy	6.6(6.5)	26.1(25.4)
Anomalous FOM	-	0.27
Refinement		
Resolution	2.3	
Number of reflections	16233	
R_{work}/R_{free}	0.22/0.26	
Number of atoms	2825	
Protein	2732	
Water	83	
RMS deviations		
Bond lengths	0.008	
Bond angles	1.02	
Average B factor	31.8	
Ramachandran analysis (%)		
Favored	98.5	
Outliers	0.3 (D64, chain E)	

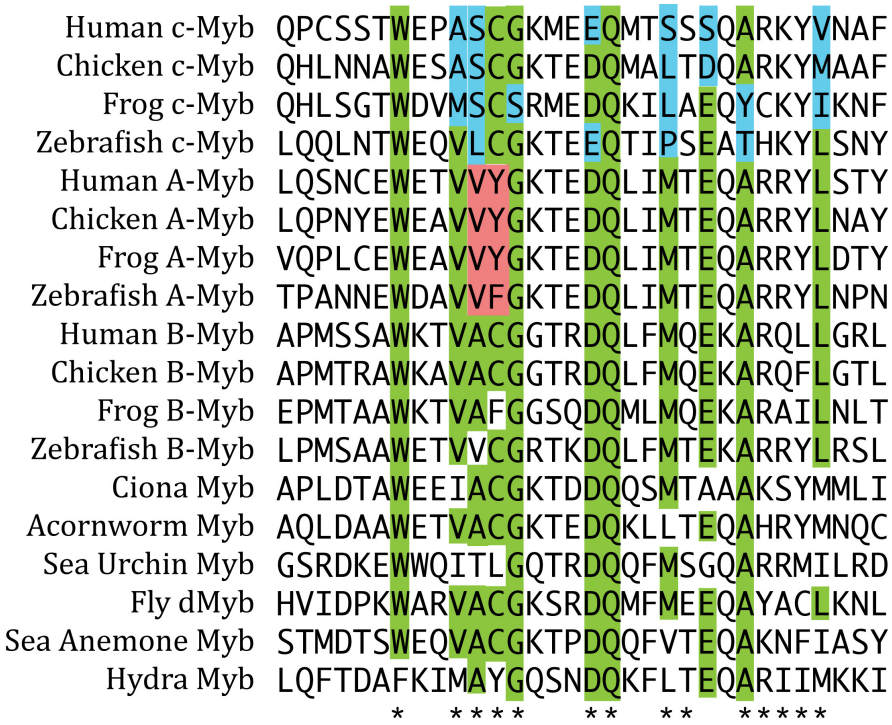

Figure 3.6 Sequence alignment of the MuvB-binding domain. Amino acids that are identical in three out of four B-Myb orthologs and dMyb are highlighted in green, with substitutions in A-Myb (red) and c-Myb (blue) noted. Asterisks indicate residues in B-Myb that make direct contact with LIN9 or LIN52 in the crystal structure.

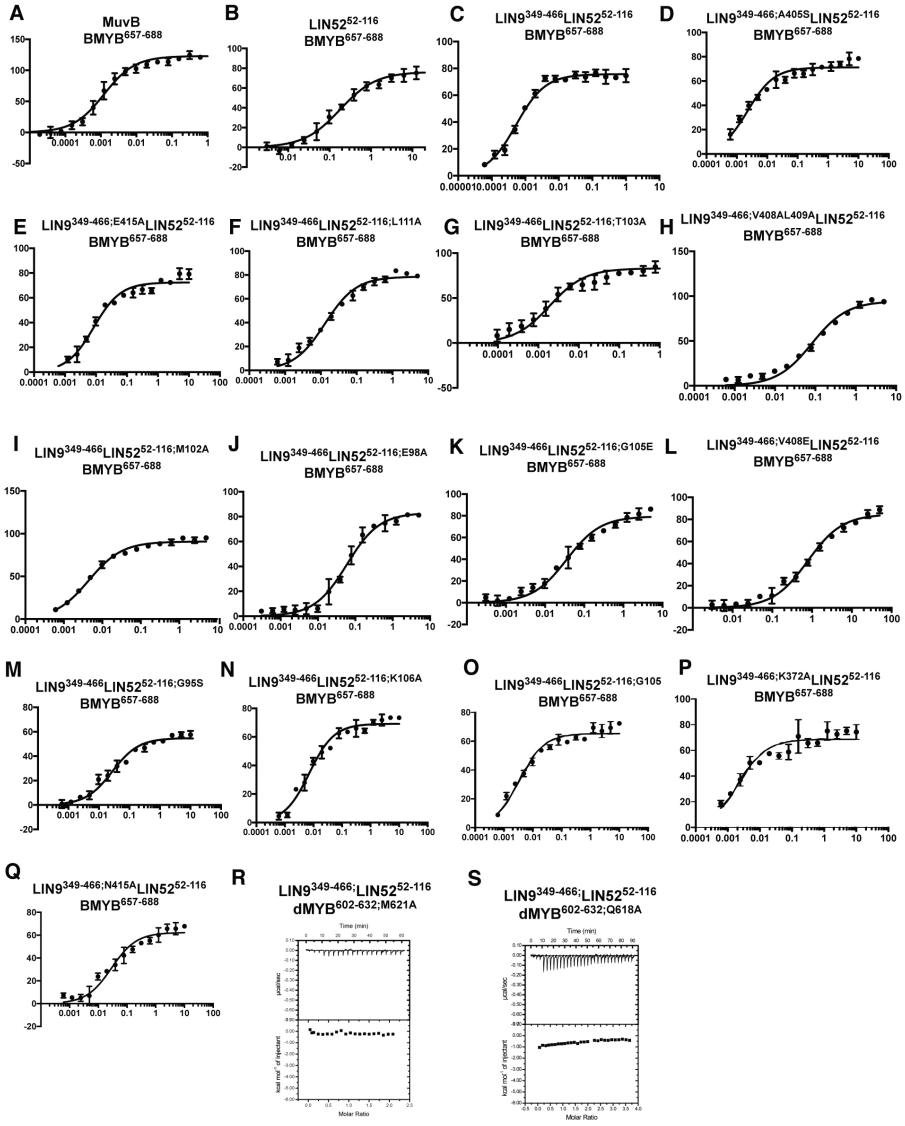

Figure 3.7 Raw data from fluorescence polarization (A-Q) and ITC (R-S) measurements of binding affinity. The FP traces represent the average from three replicates of the titration with error bars indicating the standard deviation.

3.4 Materials and Methods

3.4.1 Protein expression and peptides

Human B-Myb (residues 275-375) was expressed and purified from *E. coli* cells as a GST fusion protein. Untagged human LIN9 (349-466) was co-expressed with human GST-LIN52 (52-116). Cells were induced with 0.2 mM IPTG and grown overnight at 18°C. Proteins were first purified with glutathione affinity and anion exchange chromatography. The GST tag was cleaved with TEV protease, and the protein was passed over affinity resin again to remove free GST and concentrated.

LIN52, LIN37, RBBP48, LIN9 (94-542), LIN54 (589-749) and B-Myb were expressed in Sf9 cells (Expression Systems, Davis CA) using baculoviruses and purified as described above. The B-Myb$^{657-688}$, SeMet B-Myb$^{657-688}$ and TAMRA-B-Myb$^{657-688}$ peptides were synthesized by BioPeptide LLC., and all other peptides were synthesized by GenScript Inc.

3.4.2 Crystallization, data collection, structure determination, and model refinement

LIN52-LIN9 sub-complex was prepared for crystallization by elution from a Superdex 75 column in a buffer containing 10 mM Tris, 100 mM NaCl, and 1 mM DTT (pH 8.0). B-Myb$^{657-688}$ was added in 3-fold molar excess to 10 mg/mL LIN52-LIN9. Crystals were grown by sitting-drop vapor diffusion at 22°C in 100 mM citric acid and 5% PEG 6000 (pH 5). Crystals were frozen in 100 mM HEPES, 10% PEG 400, 20% glycerol and 1M NH_4SO_4 (pH 7). Selenomethionine derivative crystals were grown using SeMet B-Myb$^{657-688}$ in 100 mM citric acid and 5% PEG 6000 (pH 5) under Al's oil at 22°C. Streak seeding using native complex crystals was required for derivative crystal growth.

Data were collected at the Advanced Photon Source, Argonne National Laboratory at beamline 23-IDB and the Advanced Light Source, Laurence Berkeley National Laboratory at beamline 8.3.1 and 5.0.1. Diffraction spots were integrated using MOSFLM, and data were merged and scaled using Scala. Experimental phasing was solved using Phenix autosol. The

model was built with Coot, and the model was refined with Phenix. The complex crystalized with two molecules in the asymmetric unit (Supplemental Fig. 4).

3.4.3 Calorimetry

Isothermal titration calorimetry was performed with a Micro Cal VP-ITC system. Peptides and proteins were dialyzed overnight and titrated into a buffer containing 20 mM Tris, 150 mM NaCl, and 1 mM BME, pH 8.0 at 20°C. To circumvent the difficulty in accurately determining peptide concentration, data fitting was performed by fixing the complex stoichiometry to an equimolar ratio. The molecular stoichiometry observed in the crystal structure supports this assumption in the analysis.

3.4.4 Fluorescence Polarization Assay

TAMRA-labeled B-Myb$^{657-688}$ was mixed at 20 nM with MuvB, LIN52, or LIN9-LIN52 in a buffer containing 50 mM Tris, 150 mM NaCl, 1 mM DTT, 0.1% Tween, pH 8.0. 20 µL of the reaction was used for the measurement in a 384-well plate well. FP measurements were made in triplicate using a Perkin-Elmer EnVision plate reader.

3.4.5 Co-immunoprecipitation assays

Human T98G cells (ATCC #CRL 1690) were transiently transfected with pcDNA3.1 vectors encoding a GFP-only control, or GFP-tagged wild-type or mutant B-Myb alleles. HeLa cells (ATCC CCL-2™) were infected with retroviruses produced using pMSCV-Puro vectors encoding HA-tagged wild-type or mutant B-Myb, and selected using 1 µg/ml of puromycin. Cell extracts were prepared 36 hours later using EBC lysis buffer (50 mM Tris-Cl pH 7.4, 150 mM NaCl, 0.5% NP-40, protease and phosphatase inhibitor cocktails) and immunoprecipitated using anti-LIN37 antibody as previously described (Litovchick et al. 2007; Litovchick et al. 2011). Lysates were subjected to Western blot analysis using mouse

antibodies to GFP (Santa Cruz Biotech B-2, sc-9996) and p130 (BD Biosciences) as well as rabbit antibodies against LIN9, LIN37, and LIN52 (Litovchick et al. 2007; Litovchick et al. 2011). All antibodies were used at 1:1,000 dilution.

3.4.6 Chromatin immunoprecipitation assay

One million HeLa cells were transiently transfected with pcDNA3.1 vectors encoding eGFP-tagged wild-type or mutant B-Myb fusion proteins. After 36 h, the cells were cross-linked by adding 1/10 volume of 11% (v/v) formaldehyde to the culture medium, and used for chromatin isolation, immunoprecipitation and qPCR analysis using primers and conditions previously described (Marceau et al. 2016). Mouse monoclonal anti-GFP antibody (Santa Cruz B-2, sc-9996) and protein A Dynabeads™ were used for immunoprecipitation.

3.4.7 Cell proliferation assay

HeLa cell lines stably expressing HA-B-Myb wild-type or QM mutant, as well as the control untreated cells were plated in triplicate at 3,000 cells per well of a 12-well plate. Cells were trypsinized, collected, combined with trypan blue dye, and counted at days 3 and 5 after plating. Data from three independent experiments were averaged for the final analysis.

3.5 References

Andrejka L, Wen H, Ashton J, Grant M, Iori K, Wang A, Manak JR, Lipsick JS. 2011. Animal-specific C-terminal domain links myeloblastosis oncoprotein (Myb) to an ancient repressor complex. *Proc Natl Acad Sci U S A* **108**: 17438-17443.

Bandopadhayay P, Ramkissoon LA, Jain P, Bergthold G, Wala J, Zeid R, Schumacher SE, Urbanski L, O'Rourke R, Gibson WJ et al. 2016. MYB-QKI rearrangements in angiocentric glioma drive tumorigenicity through a tripartite mechanism. *Nat Genet* **48**: 273-282.

Beall EL, Lewis PW, Bell M, Rocha M, Jones DL, Botchan MR. 2007. Discovery of tMAC: a Drosophila testis-specific meiotic arrest complex paralogous to Myb-Muv B. *Genes Dev* **21**: 904-919.

Beall EL, Manak JR, Zhou S, Bell M, Lipsick JS, Botchan MR. 2002. Role for a Drosophila Myb-containing protein complex in site-specific DNA replication. *Nature* **420**: 833-837.

Davidson CJ, Tirouvanziam R, Herzenberg LA, Lipsick JS. 2005. Functional evolution of the vertebrate Myb gene family: B-Myb, but neither A-Myb nor c-Myb, complements Drosophila Myb in hemocytes. *Genetics* **169**: 215-229.

Doggett K, Jiang J, Aleti G, White-Cooper H. 2011. Wake-up-call, a lin-52 paralogue, and Always early, a lin-9 homologue physically interact, but have opposing functions in regulating testis-specific gene expression. *Dev Biol* **355**: 381-393.

Dubendorff JW, Whittaker LJ, Eltman JT, Lipsick JS. 1992. Carboxy-terminal elements of c-Myb negatively regulate transcriptional activation in cis and in trans. *Genes Dev* **6**: 2524-2535.

Ferrarotto R, Heymach JV, Glisson BS. 2016. MYB-fusions and other potential actionable targets in adenoid cystic carcinoma. *Curr Opin Oncol* **28**: 195-200.

Guiley KZ, Liban TL, Felthousen JG, Ramanan P, Litovchick L, Rubin SM. 2015. Structural mechanisms of DREAM complex assembly and regulation. *Genes Dev* **29**: 961-974.

Iltzsche F, Simon K, Stopp S, Pattschull G, Francke S, Wolter P, Hauser S, Murphy DJ, Garcia P, Rosenwald A et al. 2017. An important role for Myb-MuvB and its target gene KIF23 in a mouse model of lung adenocarcinoma. *Oncogene* **36**: 110-121.

Katzen AL, Jackson J, Harmon BP, Fung SM, Ramsay G, Bishop JM. 1998. Drosophila myb is required for the G2/M transition and maintenance of diploidy. *Genes Dev* **12**: 831-843.

Korenjak M, Taylor-Harding B, Binne UK, Satterlee JS, Stevaux O, Aasland R, White-Cooper H, Dyson N, Brehm A. 2004. Native E2F/RBF complexes contain Myb-interacting proteins and repress transcription of developmentally controlled E2F target genes. *Cell* **119**: 181-193.

Lam EW, Watson RJ. 1993. An E2F-binding site mediates cell-cycle regulated repression of mouse B-myb transcription. *EMBO J* **12**: 2705-2713.

Lane S, Farlie P, Watson R. 1997. B-Myb function can be markedly enhanced by cyclin A-dependent kinase and protein truncation. *Oncogene* **14**: 2445-2453.

Lewis PW, Beall EL, Fleischer TC, Georlette D, Link AJ, Botchan MR. 2004. Identification of a Drosophila Myb-E2F2/RBF transcriptional repressor complex. *Genes Dev* **18**: 2929-2940.

Litovchick L, Florens LA, Swanson SK, Washburn MP, DeCaprio JA. 2011. DYRK1A protein kinase promotes quiescence and senescence through DREAM complex assembly. *Genes Dev* **25**: 801-813.

Litovchick L, Sadasivam S, Florens L, Zhu X, Swanson SK, Velmurugan S, Chen R, Washburn MP, Liu XS, DeCaprio JA. 2007. Evolutionarily conserved multisubunit

RBL2/p130 and E2F4 protein complex represses human cell cycle-dependent genes in quiescence. *Mol Cell* **26**: 539-551.

Liu N, Lucibello FC, Zwicker J, Engeland K, Muller R. 1996. Cell cycle-regulated repression of B-myb transcription: cooperation of an E2F site with a contiguous corepressor element. *Nucleic Acids Res* **24**: 2905-2910.

Mages CF, Wintsche A, Bernhart SH, Muller GA. 2017. The DREAM complex through its subunit Lin37 cooperates with Rb to initiate quiescence. *Elife* **6**.

Marceau AH, Felthousen JG, Goetsch PD, Iness AN, Lee HW, Tripathi SM, Strome S, Litovchick L, Rubin SM. 2016. Structural basis for LIN54 recognition of CHR elements in cell cycle-regulated promoters. *Nat Commun* **7**: 12301.

Mucenski ML, McLain K, Kier AB, Swerdlow SH, Schreiner CM, Miller TA, Pietryga DW, Scott WJ, Jr., Potter SS. 1991. A functional c-myb gene is required for normal murine fetal hepatic hematopoiesis. *Cell* **65**: 677-689.

Muller GA, Wintsche A, Stangner K, Prohaska SJ, Stadler PF, Engeland K. 2014. The CHR site: definition and genome-wide identification of a cell cycle transcriptional element. *Nucleic Acids Res*.

Musa J, Aynaud MM, Mirabeau O, Delattre O, Grunewald TG. 2017. MYBL2 (B-Myb): a central regulator of cell proliferation, cell survival and differentiation involved in tumorigenesis. *Cell Death Dis* **8**: e2895.

Oh IH, Reddy EP. 1998. The C-terminal domain of B-Myb acts as a positive regulator of transcription and modulates its biological functions. *Mol Cell Biol* **18**: 499-511.

Osterloh L, von Eyss B, Schmit F, Rein L, Hubner D, Samans B, Hauser S, Gaubatz S. 2007. The human synMuv-like protein LIN-9 is required for transcription of G2/M genes and for entry into mitosis. *EMBO J* **26**: 144-157.

Pilkinton M, Sandoval R, Colamonici OR. 2007. Mammalian Mip/LIN-9 interacts with either the p107, p130/E2F4 repressor complex or B-Myb in a cell cycle-phase-dependent context distinct from the Drosophila dREAM complex. *Oncogene* **26**: 7535-7543.

Ramsay RG, Gonda TJ. 2008. MYB function in normal and cancer cells. *Nat Rev Cancer* **8**: 523-534.

Reichert N, Wurster S, Ulrich T, Schmitt K, Hauser S, Probst L, Gotz R, Ceteci F, Moll R, Rapp U et al. 2010. Lin9, a subunit of the mammalian DREAM complex, is essential for embryonic development, for survival of adult mice, and for tumor suppression. *Mol Cell Biol* **30**: 2896-2908.

Sadasivam S, Duan S, DeCaprio JA. 2012. The MuvB complex sequentially recruits B-Myb and FoxM1 to promote mitotic gene expression. *Genes Dev* **26**: 474-489.

Sakura H, Kanei-Ishii C, Nagase T, Nakagoshi H, Gonda TJ, Ishii S. 1989. Delineation of three functional domains of the transcriptional activator encoded by the c-myb protooncogene. *Proc Natl Acad Sci U S A* **86**: 5758-5762.

Sala A. 2005. B-MYB, a transcription factor implicated in regulating cell cycle, apoptosis and cancer. *Eur J Cancer* **41**: 2479-2484.

Schmit F, Korenjak M, Mannefeld M, Schmitt K, Franke C, von Eyss B, Gagrica S, Hanel F, Brehm A, Gaubatz S. 2007. LINC, a human complex that is related to pRB-containing complexes in invertebrates regulates the expression of G2/M genes. *Cell Cycle* **6**: 1903-1913.

Takahashi T, Nakagoshi H, Sarai A, Nomura N, Yamamoto T, Ishii S. 1995. Human A-myb gene encodes a transcriptional activator containing the negative regulatory domains. *FEBS Lett* **358**: 89-96.

Tanaka Y, Patestos NP, Maekawa T, Ishii S. 1999. B-myb is required for inner cell mass formation at an early stage of development. *J Biol Chem* **274**: 28067-28070.

Toscani A, Mettus RV, Coupland R, Simpkins H, Litvin J, Orth J, Hatton KS, Reddy EP. 1997. Arrest of spermatogenesis and defective breast development in mice lacking A-myb. *Nature* **386**: 713-717.

Wen H, Andrejka L, Ashton J, Karess R, Lipsick JS. 2008. Epigenetic regulation of gene expression by Drosophila Myb and E2F2-RBF via the Myb-MuvB/dREAM complex. *Genes Dev* **22**: 601-614.

Wolter P, Hanselmann S, Pattschull G, Schruf E, Gaubatz S. 2017. Central spindle proteins and mitotic kinesins are direct transcriptional targets of MuvB, B-MYB and FOXM1 in breast cancer cell lines and are potential targets for therapy. *Oncotarget* **8**: 11160-11172.

Zhu W, Giangrande PH, Nevins JR. 2004. E2Fs link the control of G1/S and G2/M transcription. *EMBO J* **23**: 4615-4626.

Chapter 4: p27 allosterically activates CDK4 and confers resistance to palbociclib

4.1 Introduction

The D-type cyclin family promotes the G1-S cell-cycle transition through the activation of cyclin-dependent kinases (Cdk) 4 and 6 (Cdk4/6) and subsequent inactivation of the retinoblastoma tumor suppressor protein (Rb) family (Dick and Rubin, 2013; Hunter and Pines, 1994; Malumbres, 2014). Disruption of the Cdk4/6-Rb pathway is ubiquitous in tumors and occurs typically through *CCND1* (Cyclin D1 or CycD1) amplification or loss of function of the Cdk4/6 specific inhibitor *INK4a* (p16), which drive increased Cdk4/6 activity and uncontrolled proliferation (Otto and Sicinski, 2017; Sherr et al., 2016b; Weinberg, 1995). Specific Cdk4/6 ATP-site inhibitors such as palbociclib, approved for treatment of estrogen receptor-positive breast cancer, are being tested in clinical trials for use in diverse cancer types (Finn et al., 2016; Otto and Sicinski, 2017; Sherr et al., 2016a). As the use of Cdk4/6 inhibitors as therapies increases, it becomes critical to understand the mechanisms that promote sensitivity or resistance to them.

Cdk regulation is multilayered, reflecting the need to integrate diverse growth signals to control the cell cycle, and not yet fully understood (Malumbres, 2014). Typical Cdks require cyclin binding to properly structure their catalytic site (Jeffrey et al., 1995). Cdk4-CycD is unique in that CycD binding alone does not drive an active state (Day et al., 2009; Takaki et al., 2009). At the same time, Cdk4-CycD has relatively fewer characterized substrates and seemingly poorer catalytic activity compared to Cdk2-CycA (Anders et al., 2011; Kitagawa et al., 1996; Konstantinidis et al., 1998). There are serveral cofactors that interact with Cdk4/6-CycD to modulate complex activity, assembly and localization. The Rb family members (Rb, p107 and p130), which are the best characterized substrates of Cdk4/6, contain a specific activating interaction sequence (Konstantinidis et al., 1998; Pan et al., 2001). The Hsp90-Cdc37 chaperone complex stabilizes uncomplexed Cdk4 through binding to the unfolded N-lobe of the kinase (Hallett et al., 2017; Verba et al., 2016). The INK4 family (p19, p18, p16

and p15) inhibits Cdk4/6 by obstructing cyclin binding and by pulling the activation–segment into an inactive conformation (Brotherton et al., 1998; Russo et al., 1998).

CIP (p21) and KIP (p27 and p57) proteins are also Cdk inhibitors *in vitro* and in cells under conditions of growth arrest (Harper et al., 1993; Kato et al., 1997; Ladha et al., 1998; Sherr and Roberts, 1999; Toyoshima and Hunter, 1994). Knockout mice of either p27 or p21 are highly susceptible to tumorigenesis (Fero et al., 1996; Martín-caballero et al., 2001). This tumor suppressor activity is consistent with the important roles of CIP/KIP proteins in negatively regulating the cell cycle through Cdk2 inhibition. p27 degradation is critical for licensing entry into S phase, and p21 is a key effector of p53-activated senescence (Sherr and Roberts, 1999; Sperka et al., 2012). The structural mechanism for how p27 directly inhibits Cdk2 is understood and includes insertion of a 3_{10} helix within the p27 Cdk-inhibitory domain into the Cdk2 ATP-site (Russo et al., 1996a).

In contrast, Cdk4-CycD complexes containing CIP/KIP proteins are active at times during the cell cycle (LaBaer et al., 1997a; Sherr and Roberts, 1999; Soos et al., 1996; Zhang et al., 1994), and fractions from cycling cell extracts with Cdk4-kinase activity toward Rb contain p27 (James et al., 2008). CIP/KIP proteins may promote Cdk4/6 activity by increasing complex stability or nuclear localization (Cheng et al., 1999; LaBaer et al., 1997b). The activity of Cdk4-CycD-p27 complexes requires phosphorylation of p27 by non-receptor tyrosine kinases (NRTKs) (James et al., 2008; Patel et al., 2015) (**Figure 1A**), including the breast tumor kinase (BRK/PTK6). However, whether and how p27 directly stimulates Cdk4 catalytic activity and how this activation is mediated by p27 phosphorylation are unknown.

To resolve how CIP/KIP family members both inhibit and activate Cdk4-CycD complexes, we determined the structures of Cdk4-CycD1 in complex with p27, p21 and BRK-phosphorylated p27 (phosp27). We uncovered a novel allosteric mechanism of Cdk4 activation, which explains how p27 promotes phosphorylation of Rb and especially other

substrates. We also found that p27-activated Cdk4 is resistant to inhibition by palbociclib, implicating p27 as an important mediator of palbociclib sensitivity in cancer cells.

4.2 Results

4.2.1 Crystal structures of inhibited p21-Cdk4-CycD1 and p27-Cdk4-CycD1 complexes

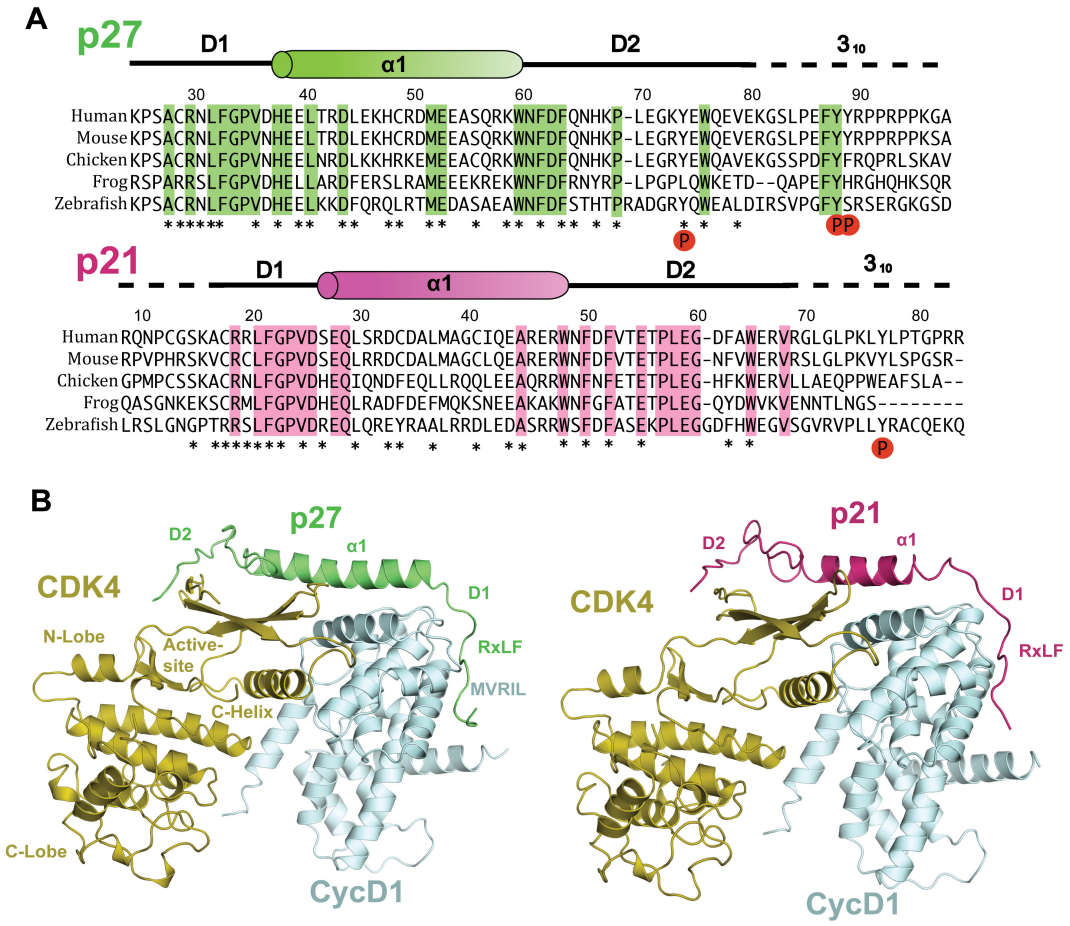

Figure 4.1. Structures of Cdk4-CycD1 complexes with CIP/KIP proteins. (A) Sequences of the kinase inhibitory domains in p27 and p21. Secondary structure assignments and interacting residues (*) identified from the crystal structures of the trimer complexes. Known tyrosine phosphorylation sites are highlighted. **(B)** Overall structure of the p27-Cdk4-CycD1 and p21-Cdk4-CycD1 complexes.

We determined the crystal structures of p21-Cdk4-CycD1 and p27-Cdk4-CycD1 complexes at 3.2 Å and 2.1 Å resolution respectively (**Figure 1 and Table S1**). We observe key differences between the trimer and Cdk4-CycD dimer structures (Day et al., 2009; Takaki et al., 2009), which explain both the inhibitory and activating mechanisms of CIP/KIP family members. We first focus on how p27 and p21 make extensive interactions with Cdk4-CycD1 to inhibit its activity. Both p21 and p27 contain a subdomain 1 (D1), which docks into a hydrophobic cleft in CycD1, and a subdomain 2 (D2), which binds the N-lobe of Cdk4 (**Figure 1**). Each CIP/KIP protein also contains a scaffolding helix (a1) that bridges the two subdomains and provides a rigid structural constraint to the relative orientation of the cyclin and kinase N-lobe domains. The structures of Cdk4 and CycD1 are similar when bound with p21 and p27 (**Figure S1**), and the trimer structures reveal two key mechanisms of inhibition (**Figure 2**).

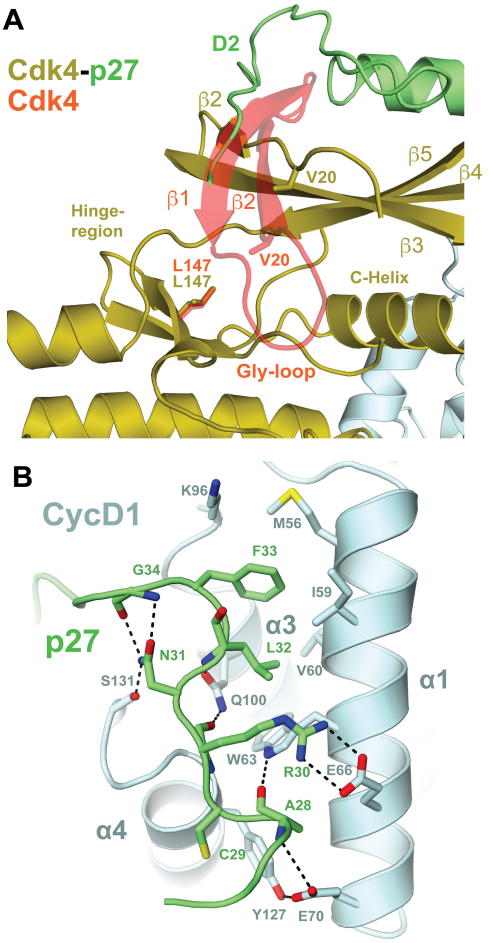

Figure 4.2. Mechanisms of Cdk4-CycD inhibition by p21 and p27. (A) Binding of the D2 region in p27 displaces the β1 strand in the Cdk4 N-lobe, which leads to disordering of the ATP-binding G loop. **(B)** Association between the p27 RxLF motif and the MVRIL cleft in CycD1 competes for substrate docking.

One inhibitory mechanism is that the p21 or p27 (p21/p27) D2 domain dislodges the glycine rich loop (Gly-loop; residues 13-19 in Cdk4) from the Cdk4 active site (**Figure 2A**).

The first strand (b1) of the Cdk4 N–lobe β-sheet is displaced by D2 of p21/p27; as a result, the first 17 residues of Cdk4, including the Gly-loop, are disordered and not present in the model. The Gly-loop coordinates the ATP phosphates and positions other Cdk4 residues (L147 and V20) that stabilize the ATP purine ring (Gibbs and Zoller, 1991; Taylor and Kornev, 2011). Thus, p21/p27 inhibits Cdk4 by disrupting the ATP-binding pocket in the active site.

The second inhibitory mechanism is that p21/p27 blocks substrate access to a critical enzyme docking site. Many Cdk-directed substrates contain an RxLF or RxLxF sequence that binds the hydrophobic cleft in cyclins known as the MRAIL site (MVRIL in Cyclin D) (Brown et al., 1999; Schulman et al., 1998). p21/p27 uses the RxLF motif in the D1 domain to bind (**Figures 2B and S1**) and therefore competes with substrate docking. For example, R30, L32, and F33 from p27 dock into a cleft in CycD1 formed by the α1 MVRIL helix, α3, and α4, and these interactions resemble those made between p27 and CycA (**Figure S2).**

A striking difference in how p27 binds Cdk4-CycD compared to Cdk2-CycA is that there is no stable interaction of the p27 3_{10} helix with the Cdk4 kinase active site (**Figures 1, 2A, and S2)** (Russo et al., 1996a). Alignment of the Cdk4 and Cdk2 structures shows that the hinge-region of Cdk4 is positioned more towards the ATP site and is in a position that would block p27 3_{10} helix association (**Figure S2**). The absence of a bound 3_{10} helix in the p27-Cdk4-CycD1 structure explains why 3_{10} helix deletion does not change the p27 IC_{50} when measuring Cdk4 directed Rb phosphorylation (Ou et al., 2011), and as explored below, it suggests a different p27 regulatory mechanism.

4.2.2 Phosphorylation of p27 activates p27-Cdk4-CycD1 complexes towards Rb and other substrates

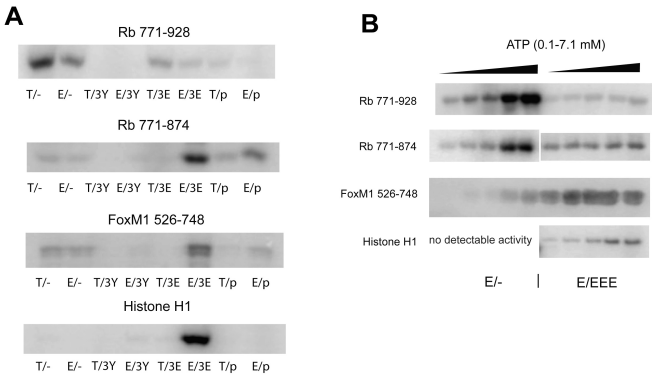

C

	E/-		E/EEE	
	K_M (μM)	k_{cat}/K_M (min^{-1})	K_M (μM)	k_{cat}/K_M (min^{-1})
Rb 771-928	1.0 ± 0.6	4 ± 2	0.04 ± 0.02	11 ± 1
Rb 771-874	3 ± 1	0.4 ± 0.2	0.10 ± 0.06	4 ± 2
FoxM1 526-748	3 ± 2	0.2 ± 0.1	0.03 ± 0.02	20 ± 20
Histone H1	no detectable activity		0.12 ± 0.02	4 ± 1

Figure 4.3. Phosphorylated p27 enhances Cdk4-CycD1 kinase activity. (A) Phosphorylation of the indicated substrate with ^{32}P-ATP. The different Cdk4-CycD1 kinase complexes are described in the main text. **(B and C)** Steady state kinase assay measuring effects of ATP concentration on initial reaction rate.

To observe the kinase activity of p27-activated Cdk4-CycD1, we purified and assayed several Cdk4 complexes: Cdk4-CycD1 dimer (called T/-), trimer with p27 (T/3Y), trimer with phosphorylated p27 (T/phos), trimer with a p27 phosphomimetic (Y74E, Y88E and Y89E; T/3E), and these same four complexes but with a phosphomimetic in the Cdk4 activation segment (Cdk4 T172E; E/-, E/3Y, E/phos and E/3E). p27 was phosphorylated with recombinant human BRK kinase and added to the Cdk4-CycD1 dimer in 3-fold molar excess to form the T/phos complex (**Figure S3**), which was then purified further to separate from BRK. A total of three p27 sites were phosphorylated (**Figure S3**), which is consistent with the presence of three tyrosines (Y74, Y88, and Y89). The other trimer complexes were purified following co-expression of all three components. We found that activation segment phosphorylation was higher in the T/- dimer (and therefore also T/phos, which was assembled from T/-) than in T/3Y and T/3E (**Figure S4**). The best characterized substrate of Cdk4/6 is the Rb protein, and a docking site along with seven Cdk phosphorylation sites have been observed in the Rb C-terminal domain (RbC, residues 771-928) (Konstantinidis et al., 1998; Pan et al., 2001). We tested Cdk4

activity toward $Rb^{771-928}$ and $Rb^{771-874}$; the latter shorter fragment lacks the docking segment. We also tested a fragment from FOXM1 ($FoxM1^{526-748}$) and histone 1 (H1) as non-Rb Cdk4 substrates (Anders et al., 2011; Kitagawa et al., 1996; Konstantinidis et al., 1998).

We found that the dimer complexes (T/- and E/-) phosphorylate $Rb^{771-874}$ and $FoxM1^{526-748}$ weakly relative to $Rb^{771-928}$, and we observed no activity toward H1 (**Figure 3A**). Addition of unphosphorylated p27 to form trimer complexes (T/3Y, E/3Y) resulted in enzyme inhibition in reactions with all substrates. We found that addition of either phosphorylated p27 or phosphomimetic p27 restored activity to the enzyme (T/3E, E/3E, T/phos, and E/phos). The highest activity was typically observed for the E/3E enzyme, which contains phosphomimetic glutamates on the activation segment and on the three phosphorylated p27 sites. Remarkably, the p27-activated enzyme complex showed strong activity toward non-Rb substrates. We observe activity toward FoxM1 and the generic substrate H1, which had been observed as a poor substrate for Cdk4/6-CycD dimer complexes (Kitagawa et al., 1996; Konstantinidis et al., 1998; Langan et al., 1989; Takaki et al., 2009).

We next performed steady-state kinetic experiments to quantify the differences between the dimer (E/-) and trimer (E/EEE) complexes' activity toward the four substrates. We examined the enzymes containing phosphomimetic mutations, because they showed the strongest activity (**Figure 3A**), and because we found slight heterogeneity in phosphorylation of the Cdk4 T172 site in our recombinant proteins (**Figure S4**). To determine the K_M of ATP, we varied ATP concentration (0.1-7.1 mM) while keeping the substrate fixed and below saturating concentration (**Figures 3B, 3C, and S5**). As previously observed, we found that the Cdk4-CycD1 dimer ATP K_M is large compared to typical Ser/Thr kinases, including Cdk2-CycA dimer (Clare et al., 2001; Knight and Shokat, 2005; Konstantinidis et al., 1998). We found that the catalytic efficiency (k_{cat}/K_M) of dimer for $Rb^{771-928}$ is ten-fold higher than for $Rb^{771-874}$ and twenty fold higher than $FoxM1^{526-748}$; dimer activity is not detectable for H1. These data support the conclusion that Cdk4-CycD1 dimer has unique activity for Rb that

requires the enzyme docking site in the far C-terminus (Konstantinidis et al., 1998; Pan et al., 2001). Notably, the ATP K_M of the p27-activated trimer is considerably reduced for all the substrates and more resembles the K_M similar of most Ser/Thr kinases (Knight and Shokat, 2005). As a result, the catalytic efficiency of the trimer toward all the substrates is greater than that of the dimer; however, unlike the preference of the dimer for Rb, the catalytic efficiency of the trimer is similar for all the substrates. Association of p27 with the MVRIL CycD site may reduce the apparent k_{cat} of ATP by inhibiting Rb docking. We conclude that phosp27 activates Cdk4-CycD by increasing ATP capture such that the trimer has broadened substrate specificity.

4.2.3 Structural Mechanisms of Cdk4-CycD activation by p27

To determine how p27 activates Cdk4-CycD, we solved the crystal structure of phosp27-Cdk4-CycD1 at 2.8 Å resolution (**Table S1)**. The structure reveals several conformational changes with respect to the Cdk4-CycD1 dimer that explain activation (Day et al., 2009). Binding of p27 rotates CycD1 toward Cdk4 (**Figures 4A**). This repositioning of the cyclin introduces a number of additional specific contacts between the a1 helix in CycD1 with the c-helix in the kinase N-lobe and a3 in the kinase C-lobe (**Figure 4B)**. Cdc37 binds to the Cdk4 C-lobe at this surface that is occluded by CycD in the p27 complex (**Figure 4C**) (Verba et al., 2016). These structural observations explain why p27 promotes Cdk4-CycD stability, assembly in the cell, and resistance to Hsp90-Cdc37 (Cheng et al., 1999; Hallett et al., 2017;

Ou et al., 2011).

We further observe that p27 induces structural changes that organize the ATP binding site. p27 binding rotates the N-lobe of Cdk4 toward CycD1 (**Figures 4D-4F**). The strands in the N-lobe β-sheet shift 4 Å such that strand 2 (S2) of the trimer complex replaces the β-strand 3 (β3) position of the dimer, β3 replaces β4 and β4 replaces β5. As a result of this β-

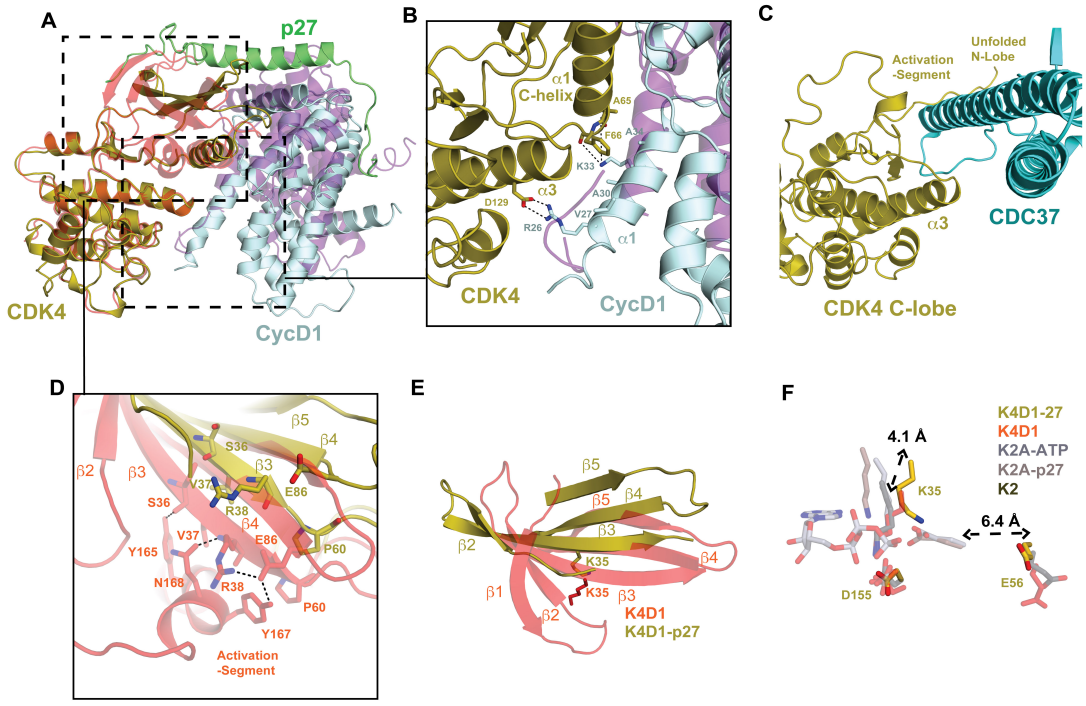

Figure 4.4. Structural mechanisms underlying p27 activation of Cdk4-CycD1 (**A**) Comparison of Cdk4-CycD1 with (gold-cyan) and without (pink-purple, PDB code: 2W96) phosp27 reveals movement of both the Cdk4 N-lobe and CycD domains relative to the Cdk4 C-lobe. **(B)** Increased interactions between CycD1 and the C-lobe in the presence of phosp27. (**C**) The Cdk4 site bound by Cdc37 is occluded by CycD1 in the p27-stabilized conformation. Movement of the N-lobe releases the activation segment **(D)** and properly positions K35 to coordinate ATP (**E and F)**.

sheet rearrangement, the catalytic lysine (K35) on β3 is pulled into a position to accept the β- and γ- phosphates of ATP (**Figure 4F**). This position of K35 is similar to the corresponding

catalytic lysine (K33) in active Cdk2-CycA and Cdk2-CycA bound to p27 (Jeffrey et al., 1995; Russo et al., 1996a). In contrast, the position of K35 in the Cdk4-CycD1 dimer is similar to Cdk2 alone, which is the inactive conformation (Schulze-Gahmen et al., 1996). This conformational change in the N-lobe does not occur when p27 binds Cdk2 and is therefore a unique allosteric activating mechanism of the CIP/KIP family specific to Cdk4 (**Figure S2**).

The removal of the activation segment from the substrate and ATP binding sites is another mechanism of p27-induced Cdk4 activation. In both the phosCdk4-CycD1 and Cdk4-CycD3 dimer crystal structures, the activation segment associates with the N-lobe of the kinase, and its closed conformation blocks substrate binding (Day et al., 2009; Takaki et al., 2009). In contrast, the activation segment is released from the active site in the phosp27-Cdk4-CycD1 trimer structure. Activation segment binding is likely destabilized as a result of the Cdk N-lobe conformational change, which breaks specific interactions between β3 and β4 and the activation segment helix (**Figure 4D**). The resultant opening of the substrate binding site compares to activation of Cdk2, in which the activation loop is pulled away from the active site through its phosphorylation and binding to CycA (Jeffrey et al., 1995; Russo et al., 1996b). In contrast to Cdk2-CycA and Cdk6-CycV (Jeffrey et al., 1995; Russo et al., 1996b; Schulze-Gahmen and Kim, 2002), we do not observe association of the activation loop with CycD1. Beyond the DFG motif, the activation segment is disordered in the phosp27-Cdk4-CycD1 structure despite its phosphorylation (**Figure S4**). Therefore, the precise structural effects of Cdk4 activation loop phosphorylation are still not clear.

Although active in solution (**Figure 3**), the phosp27-Cdk4-CycD1 trimer crystallized with the Gly-loop (disordered) and the c-helix (positioned "out" with E53 away from the active site) in what are thought to be inactive conformations. The Gly-loop likely remains disordered because p27 D2 is not completely ejected from the N-lobe in the crystal

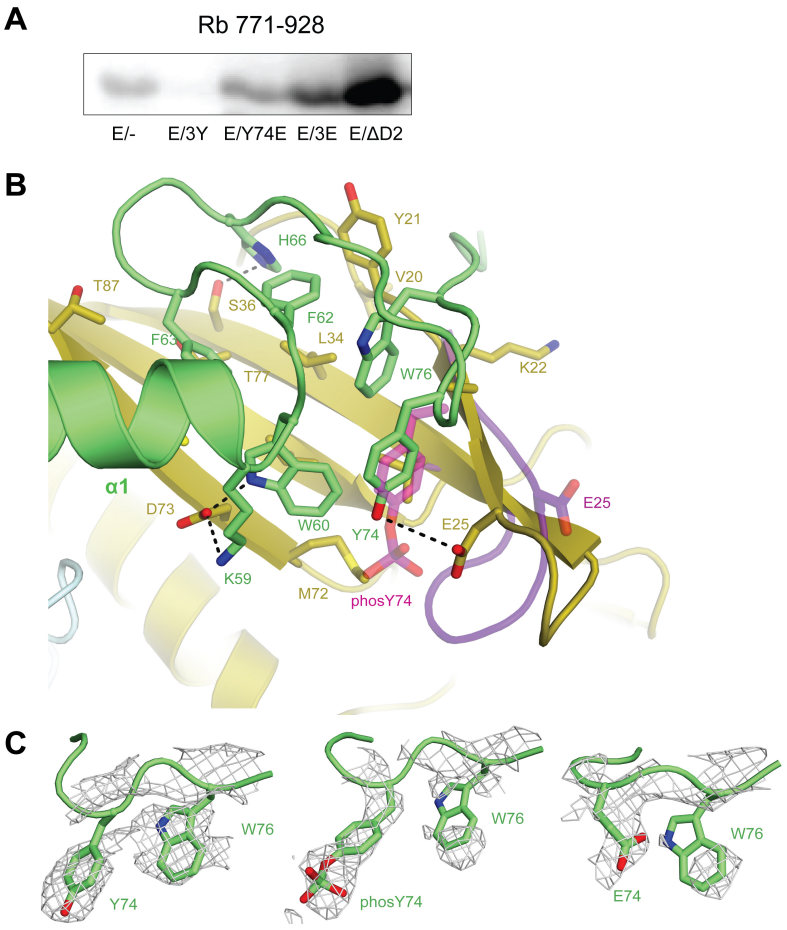

Figure 4.5. Phosphorylation of Y74 destabilizes p27 D2 association with the Cdk4 N-lobe. (**A**) ^{32}P-ATP phosphorylation of the Rb C-terminal domain using the Cdk4(T162E)-CycD1 dimer enzyme with the indicted p27 construct. E/DD2 contains p27 residues 1-60. (**B**) Comparison of trimer structures with unphosphorylated and phosphorylated Y74 in p27. (**C**) Simulated annealing omit electron density map contoured at 2s. Models and maps shown for structures with unphosphorylated (left), phosphorylated (middle), and 3E mutant p27.

despite Y74 phosphorylation (**Figure 5**). In general, cyclins activate Cdks through positioning of the c-helix (Jeffrey et al., 1995; Russo et al., 1996b; Schulze-Gahmen et al., 1996; Schulze-Gahmen and Kim, 2002). It is thought that the glutamate (E53 in Cdk4) on the c-helix is required to orient the catalytic lysine (K35 in Cdk4) for ATP coordination. Although the p27-activated trimer does not have E53 pointing toward the active site, the catalytic lysine is

placed into the correct position by the p27-induced change to the N-lobe (**Figure 4F**). Nevertheless, we found that E53 is still required for activity (**Figure S5**), perhaps to further stabilize the K35 position or perhaps to tune the K35 affinity for nucleotide to facilitate nucleotide release. Based on our structural observations, we propose that the c-helix of Cdk4 switches to the "in" conformation upon substrate binding to the active site (**Figure S4**).

4.2.4 Y74 phosphorylation relieves p27 inhibition of Cdk4-CycD1

It is clear from the structural data that the activating conformational changes induced by phosp27 are also induced by unphosphorylated p27. Therefore, the inhibited p27 trimer complex is primed for activity in that K35 positioned to coordinate ATP and the activation loop is released. However, the enzyme is held inactive by the p27 D2 subdomain, which displaces Cdk4 b1 and prevents formation of the ATP-binding G-loop. We propose that phosphorylation of p27 results in an active complex by relieving this critical p27 inhibitory function.

Y88 and Y89 are disordered in both the phosp27 and unphosphorylated crystal structures. Considering that these tyrosines do not stabilize an inhibitory association with Cdk4-CycD1, we reasoned that Y88 and Y89 phosphorylation is dispensable for enzyme activity of the trimer complex. We tested this hypothesis and indeed found that Cdk4-CycD1 assembled with p27 containing a phosphomimetic at Y74 phosphorylation (E/Y74E) has comparable activity to the enzyme assembled with phosphomimetics at all the tyrosines (E/3E) (**Figure 5A**). This result is different from the p27-inhibition mechanism in Cdk2, in which phosphorylation of p27 Y88/Y89 are necessary for ejection of the p27 3_{10} helix from the catalytic site (Grimmler et al., 2007).

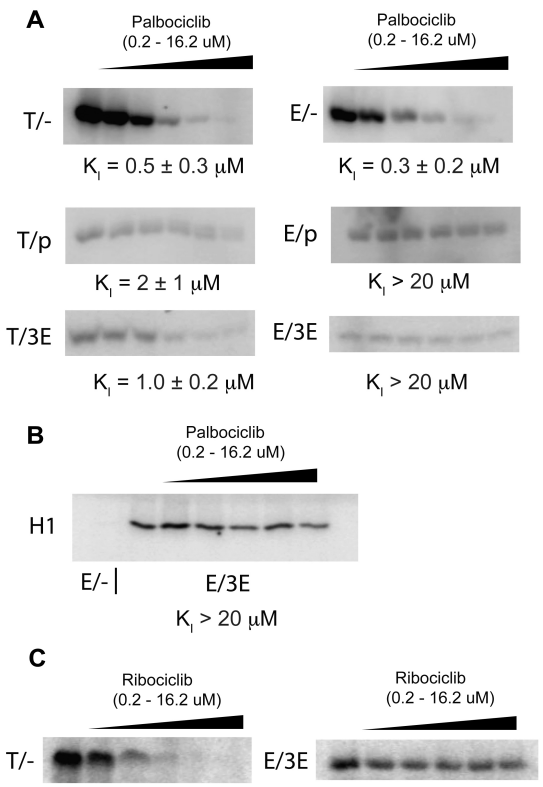

Figure 4.6. Palbociclib poorly inhibits p27-Cdk4-CycD1 kinase activity. (A) ^{32}P-ATP phosphorylation of the Rb C-terminal domain using the indicated Cdk4-CycD1 enzyme and in the presence of increasing palbociclib concentrations. Reported K_i values are averages from 3-5 replicates. (**B and C**) Same as in (A) but using histone H1 as substrate or ribociclib as the inhibitor.

In the phosp27-Cdk4-CycD1 structure, Y74 is in a similar position as in the unphosphorylated trimer, but there is clear electron density for the phosphate (**Figures 5B and 5C**). Subtle differences between the structures suggest that Y74 phosphorylation weakens the association of p27 D2 with the Cdk4 N-lobe. The loop connecting β2 and β3 of the N-lobe of the kinase loses a hydrogen bond between Y74 on p27 and E25 of Cdk4, and the loop flips to an outward conformation. van der Waals interactions between W60 on p27 and Y74 also

appear disrupted when Y74 is phosphorylated. Notably, we found that deletion of the D2 domain from p27 leads to a trimer complex that phosphorylates Rb (E/DD2 in **Figure 5A**). This result supports a model in which phosphorylation or phosphomimetics weaken the affinity of the D2 domain for Cdk4 N-lobe, allowing for the release of the Gly-loop and activation of the kinase. We additionally solved the structure of p27(3E)-Cdk4-CycD1 (**Table S1**), and we found that B-factors were higher and electron density was weaker for residues in D2 of both phosphorylated and 3E-mutated p27 (**Figure 5C**). The higher B-factors are consistent with lower D2 occupancy and higher disorder.

4.2.5 Activated p27-Cdk4-cycD1 complexes are resistant to palbociclib

The structural changes in the kinase N-lobe and ATP site that occur upon p27 binding suggest that CIP/KIP proteins may influence how Cdk4/6 responds to ATP-site inhibitors. We tested the effects of palbociclib on the enzyme activity of our reconstituted Cdk4-CycD1 complexes (T/-, E/-, T/3E, E/3E, T/phos and E/phos) (**Figure 6A**). As expected, palbociclib inhibited $Rb^{771-874}$ phosphorylation by both Cdk4-CycD1 dimers (T/- and E/-). Strikingly, the activated p27-Cdk4-cycD1 complexes (T/phos, E/phos, T/3E and E/3E) were all to some extent resistant to palbociclib inhibition. We also observe resistance to inhibition when assaying activity toward the generic substrate H1 (**Figure 6B**), and we observe a similar pattern of sensitivity and resistance to the drug ribociclib (**Figure 6C)**. We propose that the p27-induced N-lobe reorientation, which remodels the ATP-binding site, accounts for why Cdk4-specific inhibitors lose potency toward the trimer.

The kinase activity assays demonstrate that p27 activation of Cdk4-CycD1 directly confers palbociclib resistance to the enzyme. The *CDKN1B* gene coding for p27 is rarely mutated or deleted in cancer, and our analysis of p27 transcript expression in pancreatic and breast tumors suggests that p27 is often expressed (**Figures S6A and S6B).** We therefore tested in cancer cells whether p27 levels influence palbociclib sensitivity. We performed siRNA knockdown of p27 in a set of genetically characterized pancreatic cancer cell lines

(**Figure 7** and **Figure S6**). These cell lines harbor canonical genetic features of pancreatic cancer (e.g. *KRAS*, *CDKN2A*, and *TP53* mutation) and are generally deficient for p16 but express p27 (**Figures S6C and S6D**). Moreover, these cells show only modest response to palbociclib (**Figure 7A**) and contain more robust association of p27 with Cdk4 complexes than Cdk2 complexes (not shown). Importantly, we found that p27 knockdown increases sensitivity to palbociclib (**Figures 7A, S6E, and S6F**), as proliferation is more inhibited in cells transfected with p27 siRNA compared to control cells. We note that several aspects of this experiment support the hypothesis that p27 loss removes an activating function of p27. First, even in the absence of drug, proliferation is reduced in p27 siRNA transfected cells relative to control. Second, assaying by immunoblot, we found that palbociclib only inhibits Rb phosphorylation once p27 is depleted (**Figure 7B**). This result suggests that p27 present in Cdk4-CycD complexes in these cells confers resistance to palbociclib inhibition of kinase activity.

4.3 Discussion

CIP/KIP proteins were first characterized as Cdk inhibitors, particularly as potent inhibitors of Cdk2-CycA/E (Harper et al., 1993; Kato et al., 1997; Ladha et al., 1998; Sherr and Roberts, 1999; Toyoshima and Hunter, 1994). In contrast, other evidence implicated non-inhibitory roles for p21 and p27 in mediating Cdk4-CycD function, including complex stability and nuclear localization (Cheng et al., 1999; LaBaer et al., 1997b). Moreover, the observation that Cdk4-CycD tolerates the presence of p27 and that Rb-directed kinase activity in cells contains p27 led to models that Cdk4-CycD may titrate inhibitory p27 away from Cdk2 (LaBaer et al., 1997a; Sherr and Roberts, 1999; Soos et al., 1996; Zhang et al., 1994). Our data demonstrate that p27 is not merely a non-inhibitor, but it in fact allosterically activates Cdk4-CycD, remodeling the kinase to increase the catalytic efficiency of ATP processing. Our structural data demonstrate that this effect is specific to Cdk4 (vs. Cdk2) and

is induced by Y74 phosphorylation in p27. It is noteworthy that p21 contains a phenylalanine at the equivalent position as Y74 (**Figures 1A and S1**), suggesting that if p21 similarly activates Cdk4, its inhibitory association with the N-lobe must be relieved by some mechanism other than D2 tyrosine phosphorylation.

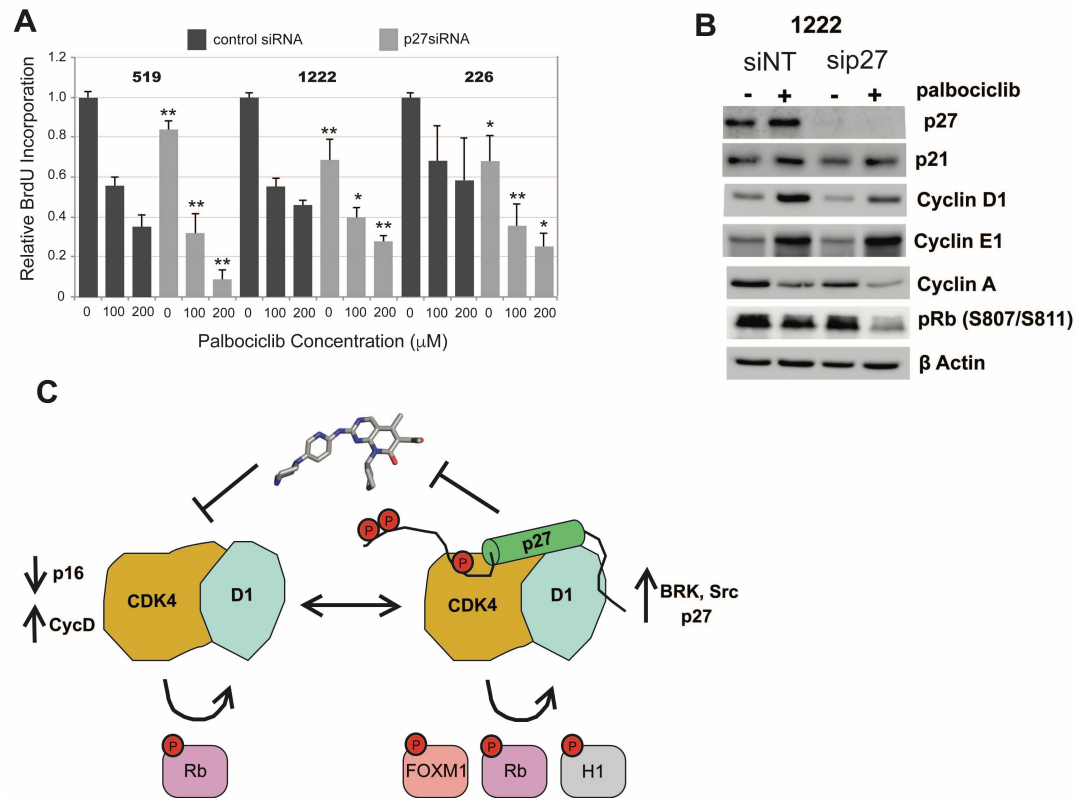

Figure 4.7. p27 is a determinant of palbociclib sensitivity in several pancreatic cancer cell lines. (**A**) The indicated cell lines were transfected with plasmids expressing control and CDKN1B (p27) siRNA and cell proliferation in the presence of the indicated palbociclib concentration was measured through detection of BrdU incorporation 72 hrs after treatment. Asterisks indicate confidence in pairwise comparisons of the experimental and control data at the same palbociclib concentration (* $p < 0.01$, ** $p < 0.001$). The p27 siRNA data normalized to zero palbociclib is shown in Fig. S7. (**B**) Western blot using antibodies recognizing the indicated proteins was performed on 1222 cell extracts 72 hrs after treatment with the indicated siRNA (not-targeting control or p27) and with 200 mM palbociclib where indicated. **(C)** Overall model for how p27 modulates Cdk4 activity and sensitivity to palbociclib.

We find that p27 activation is a mechanism to broaden Cdk4 substrate specificity. While the Cdk4-CycD1 dimer only processes ATP efficiently in the presence of Rb, the active trimer

has similar activity in the presence of all tested substrates, including the generic Cdk substrate histone H1 (**Figure 3**). The requirement of p27 for efficient non-Rb substrate phosphorylation may explain why, relative to Cdk2 for example, fewer cell-cycle substrates have been identified for Cdk4/6 and why it has been thought that Rb is a unique Cdk4/6 substrate (Kitagawa et al., 1996; Konstantinidis et al., 1998; Pan et al., 2001). In fact, other Cdk4/6 substrates have been identified more recently (Anders et al., 2011; Wang et al., 2017; Zhang et al., 2018), and it will be important to explore the role of p27 in their regulation by phosphorylation. Our observation that ATP capture by Cdk4-CycD1 in the presence of Rb is similarly low to other substrates but that catalytic efficiency is particularly high is consistent with other observations of a unique docking site in the Rb C-terminal domain (Pan et al., 2001). Thus, the unique property of Rb as a Cdk4-CycD substrate is its ability to more tightly associate with the dimer and be phosphorylated even when ATP affinity is so low. In contrast, we observe that this Rb-specific property is lost upon p27 association, which implicates a competitive association between Rb and p27 for Cdk4-CycD, perhaps at the MVRIL site.

The role of p27 as a Cdk inhibitor and negative regulator of the cell cycle has been well studied as a mechanism for p27 function as a tumor suppressor protein (Bencivenga et al., 2017; Chu et al., 2008). However, in contrast to the canonical tumor suppressor and Cdk4 inhibitor p16, p27 is rarely deleted or mutated in cancer, and p27 mRNA is typically expressed (**Figure S6**) (Bencivenga et al., 2017; Chu et al., 2008). Our observation that p27 activates Cdk4-CycD may explain and motivate discovery of roles for p27 as a positive effector of growth in cancer. The overexpression of “Src-like” tyrosine kinases (Src, Brk, etc.), a common phenotype in diverse tumors, drives cell proliferation and invasion, confers resistance to hormone therapy, and is associated with poor prognosis (Kim et al., 2009; Ostrander et al., 2010). Src-family kinase expression is known to increase p27 phosphorylation in proliferating cells (Grimmler et al., 2007; Patel et al., 2015), which leads to

p27-Cdk4-CycD activity in our assays. These observations suggest that the Cdk4-activating function of p27 may be a potential effector of oncogenic tyrosine activity in cancer. The overexpression of BRK in breast cancer cells leads to resistance to palbociclib, and it has been suggested that Brk phosphorylation of p27 may mediate this effect (Patel et al., 2015; Patel et al., 2018). Here we show that activated Cdk4-cycD1-phos27 complexes are resistant to palbociclib and ribociclib inhibition *in vitro* and that both Brk and p27 can contribute to resistance in some cell lines. This represents a unique mechanism whereby Cdk4 can evade inhibition when non-receptor tyrosine kinases are activated.

Our observation that p27-activated Cdk4-CycD is resistant to palbociclib suggests that the relative populations of Cdk4 dimer and trimer complexes may determine the sensitivity of cancer cells to Cdk4 inhibitors (**Figure 7C)**. For example, p16 loss and high CycD expression, both of which increase the levels of dimer, have been correlated with high palbociclib sensitivity (Finn et al., 2016; Otto and Sicinski, 2017; Sherr et al., 2016a). Our observation that the dimer has unique activity toward Rb compared to other substrates (**Figure 3**) perhaps explains why inhibition of Rb phosphorylation has been found to be perhaps the most critical effector for palbociclib activity (Finn et al., 2016; Otto and Sicinski, 2017; Sherr et al., 2016a). In contrast, tumor cells with wild-type levels of p16 have shown low sensitivity to palbociclib (Cen et al., 2012; Ramsey et al., 2007; Young et al., 2014), which we propose results from a low ratio of susceptible dimer to resistant trimer complexes. This model is further supported by our p27 knockdown experiment, which suggests that in certain cell types, depletion of trimer complexes increases sensitivity. We recognize that effects of p27 may be more complicated, particularly because p27 modulates both Cdk4/6 (palbociclib sensitive) and Cdk2 (palbociclib resistant) complexes. Further exploration of the different genetic contexts in which p27 confers sensitivity or resistance to ATP-site inhibitors is needed to understand and harness their therapeutic potential.

4.4 Materials and Methods

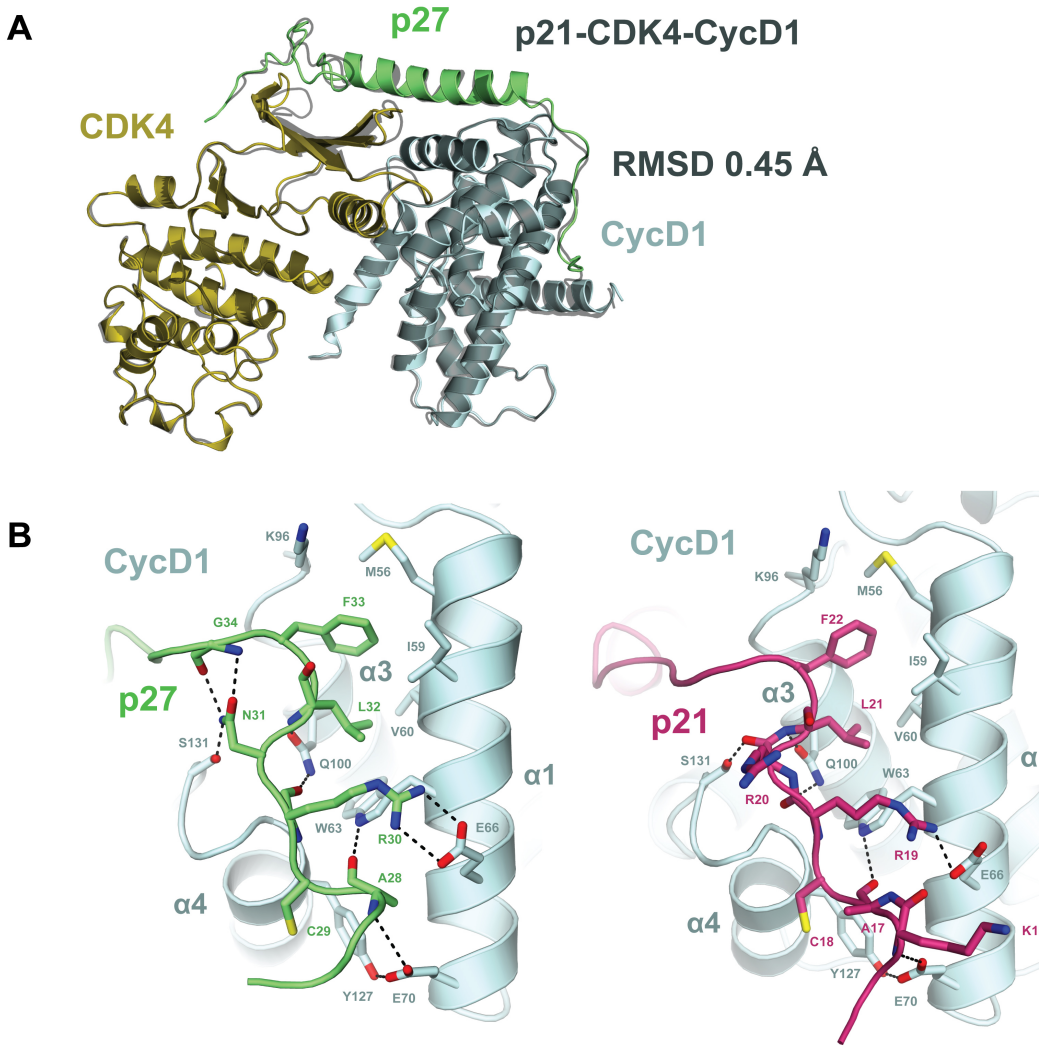

Figure 4.8. Related to Figure 1. Comparison of the p21- and p27-Cdk4-CycD1 trimer complexes. (A) Overlay of the structures highlights that the overall structure of Cdk4 and CycD are similar in the trimer complexes with a root mean square deviation of 0.45 Å for Cα atoms. **(B)** Comparison of the p27 (left, green) and p21 (right, pink) RxLF interactions with the hydrophobic cleft site in CycD1.

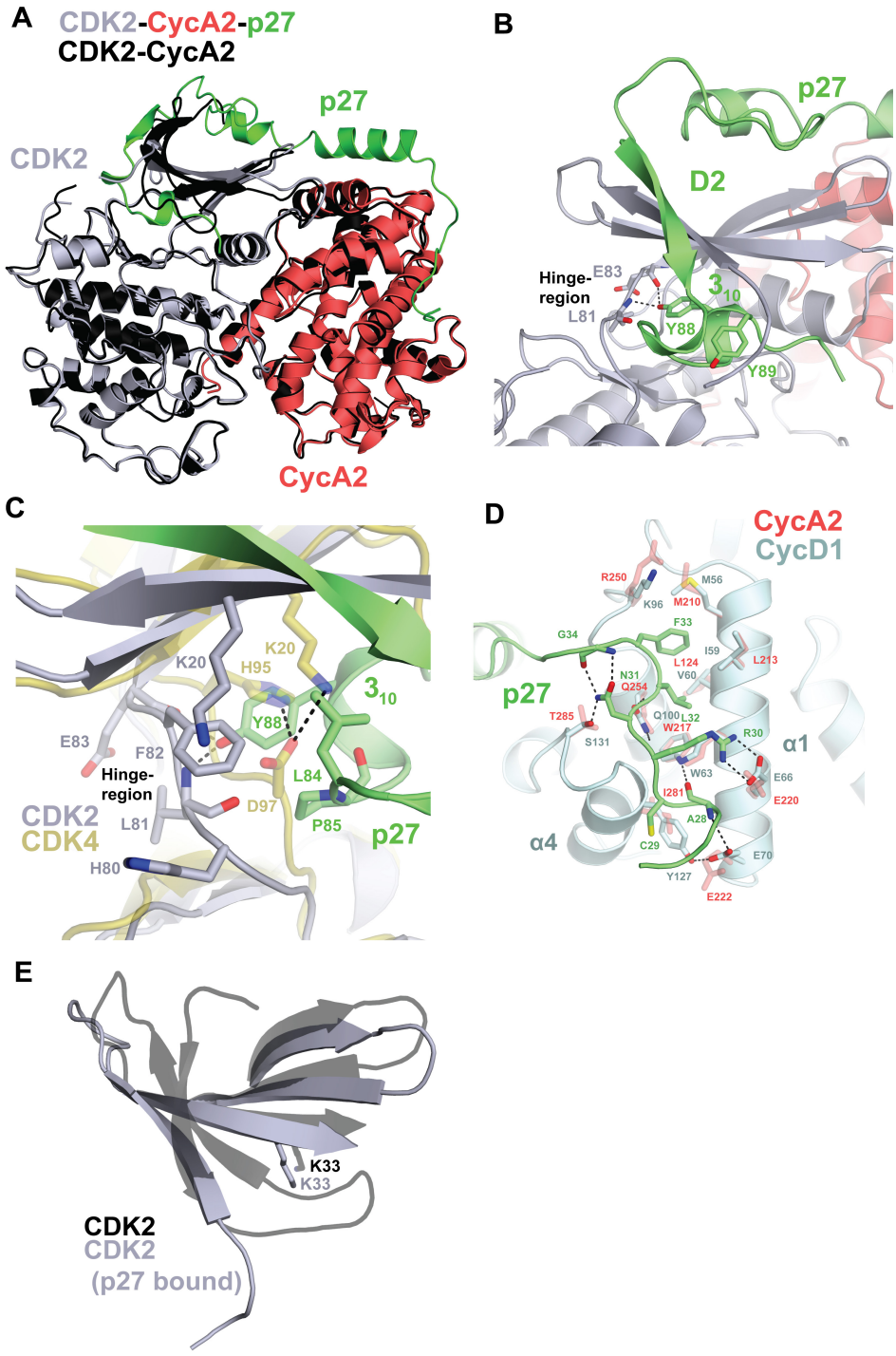

Figure 4.9. Related to Figures 2 and 4: Comparison of how p27 binds and influences the structure of Cdk4-CycD1 and Cdk2-CycA. (A) Alignment of the Cdk2-CycA2 dimer (black, PDB code: 1JST) and Cdk2-CycA2-p27 trimer (colors, PDB code: 1JSU) structures. Unlike the case for Cdk4-CycD1 (Figure 4A), association of p27 does not change the relative orientation of the Cdk and cyclin domains. (**B**) p27

binds the Cdk2 active site by inserting a small 3_{10}-helix into the ATP site. (**C**) Differences in the Cdk4 hinge region from Cdk2 suggest that 3_{10} helix insertion of p27 into the Cdk4 active site would be sterically hindered. (**D**) Comparison of p27 interactions with the hydrophobic clefts in CycD1 and CycA2. F33 and L32 on p27 dock into hydrophobic pockets in CycD1 formed by the α1 MVRIL helix. R30 on p27 forms a salt-bridge with CycD1 E66 at the N-terminus of the MVRIL helix. The CycD1 W63 indole also forms a hydrogen bond with the carbonyl of p27 A28. CycD1 Q82 forms a hydrogen bond with the carbonyl and amide of R30 and L32 respectively. S131 on CycD1 positions N31 on p27 through a hydrogen bond to form an intramolecular hydrogen-bonding network with the amide and carbonyl of G34, which stabilizes the loop conformation at the end of the RXL motif. While many of these interactions are also present between p27 and CycA, a notable difference is Y127 on α4 of the cyclin-box domain of CycD1, which hydrogen bonds and positions E70 on α1 to form a hydrogen bond with the amide of p27 A28. Y127 also makes van der Waals interactions with C29 on p27. Overall, the similar interactions with CycA and CycD explain the previous observation that D1 deletion results in a similar loss in affinity of p27 for either Cdk2-CycA or Cdk4-CycD (Ou et al., 2011). (**E**) Unlike in Cdk4, the N-lobe of Cdk2 does not undergo a conformational change upon p27 binding, except for displacement of the ATP-binding G-loop.

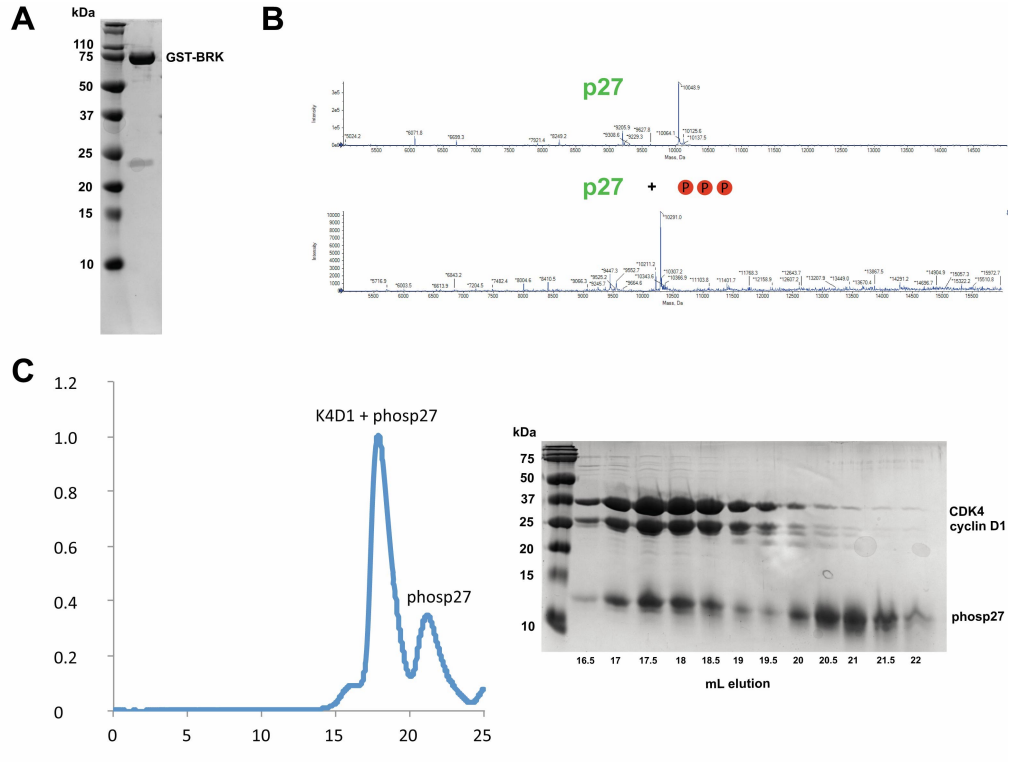

Figure 4.10. Related to Figures 3, 4, and 5. Preparation of phosp27 and reconstitution of the phosp27-Cdk4-CycD1 trimer. (A) Coomassie-stained gel of purified recombinant GST-BRK kinase. **(B)** Electrospray mass spectrometry demonstrates that purified p27 (residues 25-93) is phosphorylated on three sites after treatment with GST-BRK. **(C)** Purification of the assembled phosp27-Cdk4-CycD1 trimer using Superdex 200 size-exclusion chromatography. The excess phosp27 introduced upon mixing with purified Cdk4-CycD1 dimer elutes as a separate peak.

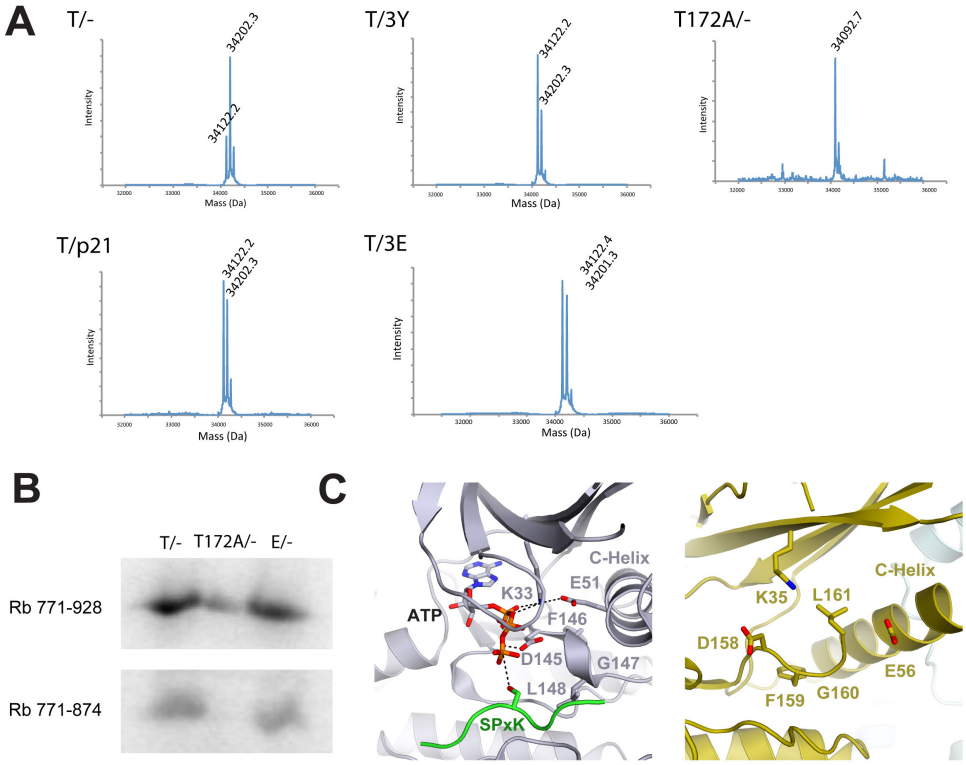

Figure 4.11. Related to Figure 3. Characterization of Cdk4-CycD1 activation segment phosphorylation (A) Electrospray mass spectrometry analysis of our Cdk4 samples suggests that p27 and p21 inhibits T172 phosphorylation. Cdk4-CycD1 purified from insect cells (T/-) shows ~70% T172 phosphorylation whereas co-expression with either p21 (T/p21) or p27 (T/3Y and T/3E) results in ~30%-50% phosphorylation. (**B**) The phosphorylated and phosphomimetic Cdk4 show greater activity towards Rb 771-928 than a T172A mutant kinase. ^{32}P kinase assay as in Figure 3A is shown. **(C)** Comparison of the activation segment in the Cdk4-CycD1-p27 structure and the Cdk2-CycA2 structure with a substrate peptide bound (PDB code: 1QMZ). In the Cdk4 trimer structure, the DFG is seen in the "in" conformation and is disordered beyond the L161 in the following position. L161 appears to occlude the c-helix from its active "in" conformation. In contrast, the corresponding L148 from Cdk2, in contacting substrate, adopts a conformation that is compatible with the active c-helix position. We propose that substrate binding to Cdk4 similarly positions the DFGL sequence to allow c-helix rotation. The phosp27-Cdk4-CycD complex structure, like the previous Cdk4-CycD dimer crystal structures, still resembles an inactive kinase in that the c-helix adopts the "out" conformation, with the critical glutamate pointing away from the active site (Day et al., 2009; Takaki et al., 2009; Taylor and Kornev, 2011). However, these complexes are phosphorylated on their activation segment and are active in solution. It may be that ATP or RbC binding is also required to generate the c-helix "in" conformation. Our phosphorylated p27 crystal structure was crystallized in the presence of 10 mM ADP or ATPγS, but the nucleotides had very low occupancy, likely a result of crystallization favoring the p27 D2-bound conformation in which the G-loop is not formed. Interestingly, one of the dimer structures, which has a properly formed G-loop, was similarly solved in the presence of AMP-PNP but lacked nucleotide electron density in the ATP-site (Takaki et al., 2009). Our structural data demonstrate how p27 induces a conformational change in the N-lobe that supports the active structure and ATP binding. Previous data indicate that the K_M for ATP is decreased when Rb is complexed with Cdk4 (Konstantinidis et al., 1998), suggesting Rb docking can potentially introduce a similar activating allosteric change as p27.

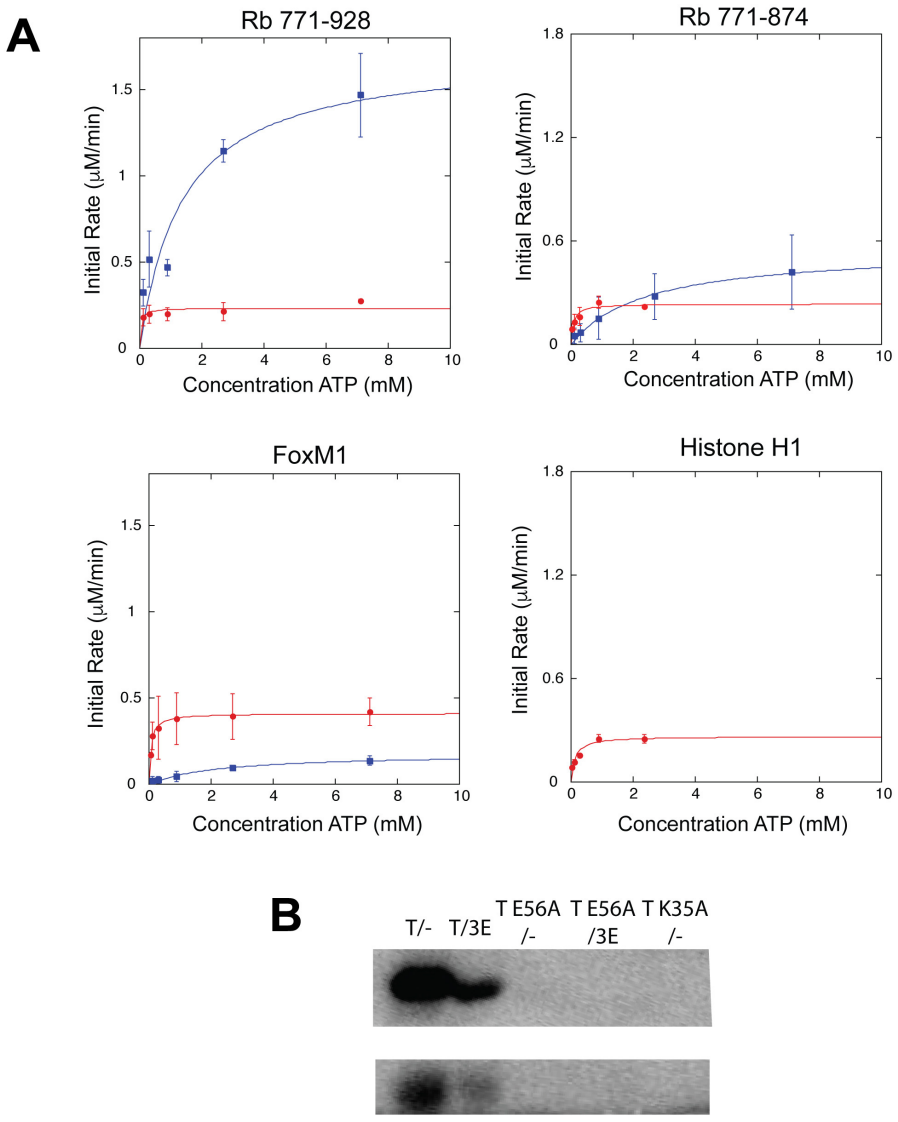

Figure 4.12. Related to Figures 3 and 4. Data supporting mechanism for p27 activation of Cdk4-CycD1. (A) Steady state kinetic analysis of Cdk4-CycD1 activity toward the indicated substrate. Red circles are measurements using Cdk4-CycD1 dimer with the T172E mutation (E/-); blue squares are measurements using the T172E mutant dimer assembled with p27 containing the triple glutamate mutation (E/EEE). The data points and error bars shown in the graphs are the averages and standard deviations, respectively, of initial rates at each concentration point across three replicates. (**B)** ^{32}P-ATP kinase assay using Rb 771-928 as substrate as in Figure 3A. Cdk4-CycD1 dimer (T/-) and trimer with the triple glutamate mutation in p27 (T/3E) were used as enzymes along with mutations to E56 and K35 in Cdk4. The loss of phosphorylation demonstrates the importance of those residues for Cdk4 kinase activity.

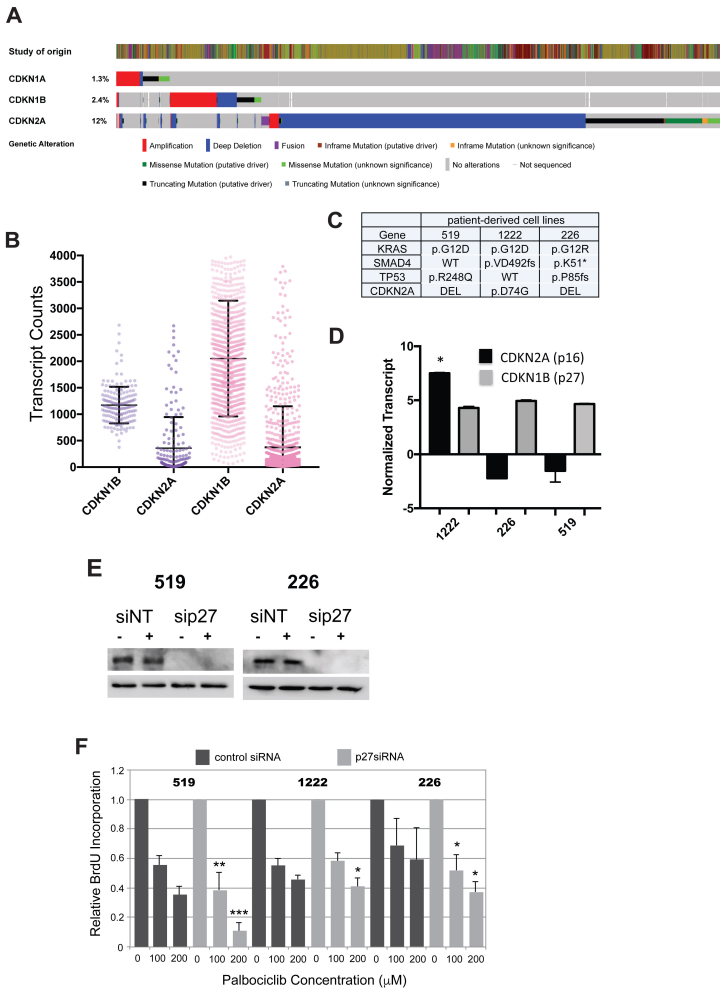

Figure 4.13. Related to Figure 7. Data supporting siRNA knockdown of p27 in patient-derived pancreatic cancer cell lines. (**A**) Relative to p21 and p27 are not commonly deleted or mutated in tumors. cBioPortal (http://www.cbioportal.org) report of annotated alterations of *CDKN1A* (p21), *CDKN1B* (p27), and *CDKN2A* (p16) across all entries in the database. The percentage is of the number of total alterations in the current cBioPortal data set. (**B**) RNA sequencing data of 179 pancreatic cancer and 1,1000 breast cancer cases from the TCGA was mined for the expression of CDKN1B and CDKN2A. The mean and standard deviation (error bars) for transcript counts in shown. The expression of CDKN2A is significantly lower than the expression of CDKN1B ($p<0.000001$) by student t-test. We have found that his relationship is also preserved in multiple other solid tumor types that retain RB1 (not shown). (**C**) Table shows status of typical genetic drivers of pancreatic cancer in the cell lines used in this study. * indicates that the SMAD 51K mutant allele is expressed. (**D**) p27 and p16 transcript levels measured in the pancreatic cancer cell lines. * indicates that the D74G mutant allele is expressed. (**E**) Western blot of p27 levels upon treatment with control and p27 siRNA in the different cell lines. See Figure 4D for 1222 cells. (**F**) Data are shown from the siRNA and cell proliferation experiment presented in Fig. 4C, but here the data are normalized within the p27 siRNA groups to zero palbociclib concentration in order to compare more clearly the changes induced by palbociclib addition. Asterisks indicate confidence in pairwise comparisons of the experimental and control data at the same palbociclib concentration (* $p < 0.05$, ** $p < 0.01$, *** $p < 0.001$).

4.4 Materials and Methods

4.4.1 Protein Expression and peptides

Human Cdk4 (residues 1-303), cyclinD1 (16-267), $p27^{KID}$ (25-93), $p21^{CIP}$ (9-84), and BRK (1-451), were expressed and purified from Sf9 cells. The Cdk4 contains a mutation in a glycine-rich sequence (ΔG45-G47, G43E, G44E) that mimics Cdk6 and is required for crystallization (Day et al., 2009). Cdk4, p27, p21 and BRK were expressed as GST fusion proteins. CycD1 was co-expressed with other components untagged. Lysates were first purified by GS4B affinity chromatography. The protein was then eluted from the resin and subject to SOURCE 15Q (GE Healthcare) anion exchange chromatography. The elution fraction was then subjected to TEV protease cleavage overnight in 25 mM Tris, 200mM NaCl, 1 mM DTT, 0.5 mM EDTA (pH 8.0). The protein was then passed over GS4B affinity resin again to remove free GST, concentrated, and stored in a buffer containing 20 mM Tris, 200mM NaCl, 1 mM DTT, and 20% glycerol (pH 8.0).

4.4.2 Phosphorylation of p27

Recombinant $p27^{KID}$ (25-98) was expressed as a GST-fusion in *E. coli* and purified as described above. It was treated with 10 % GST-BRK (m/m) in a buffer containing 50 mM Tris, 150 mM NaCl, 1 mM DTT, 10 mM $MgCl_2$ and 1 mM ATP (pH 8.0) and incubated at 4°C for 24 hours. The phosphorylated p27 was purified by passing through GS4B affinity resin and eluted from a Superdex 75 column in a buffer containing 25 mM Tris, 100 mM NaCl, and 1 mM DTT (pH 8.0). The extent of phosphorylation was confirmed using electrospray mass spectrometry on a SCIEX X500 QTOF spectrometer.

4.4.3 Kinase assays

Cdk4 complexes (0.5 μM) were mixed with substrate (20 μM) in a buffer containing 25 mM Tris, 200 mM NaCl, 10 mM $MgCl_2$, 1 mM DTT, 250 μM ATP, and 100 μCi of ^{32}P-γ-ATP (pH 8.0). Substrate was diluted into the reaction buffer, and the reaction was initiated

through addition of ATP. Substrate concentrations in the quantitative rate assays (Figs. 2b and 2c) were 50 μM for $Rb^{771-928}$, $Rb^{771-874}$, and $FoxM1^{526-748}$ and 10 μM for histone H1. Reactions were quenched after 30 min through addition of SDS–PAGE loading buffer. Independent time course experiments confirmed that phosphate addition is still linear with time beyond 45 min using our experimental conditions. SDS–PAGE gels were imaged with a Typhoon scanner and bands quantified using the ImageJ software package. For each assay, three to five replicates were performed. The kinetic parameters (K_M, $k_{cat,}$ K_i) were determined for each individual replicate, and the reported values are averages of the replicates with standard deviations reported as errors.

4.4.4 Crystallization, data collection, structure determination, and model refinement

Table 4.1 X-ray crystallography data collection and refinement statistics for CDK4 complexes. Values in parentheses are for highest resolution shell.

CDK4-CycD1-	p27	p21	phosp27	p27 3E
Data collection				
Space group	$P2_122_1$	$P2_122_1$	$P2_122_1$	$P2_122_1$
Resolution	93.64-2.30 (2.38-2.30)	92.68-3.19 (3.41-3.19)	45.72-2.89 (2.99-2.89)	62.77-2.80 (2.9-2.8)
Cell dimensions				
a, b, c	62.40, 67.48, 187.28	62.6, 67.9, 185.4	62.85, 66.63, 184.24	62.58, 66.73, 184.85
α, β, γ	90, 90, 90	90, 90, 90	90, 90, 90	90, 90, 90
R_{merge}	13.0 (116.0)	16.7 (83.7)	18.8 (99.9)	19.4 (82.6)
Total reflections	274807 (34774)	81814 (14232)	232992 (36095)	139972 (21264)
Unique reflections	35354 (4854)	13821 (2439)	18044 (2830)	19805 (2851)
I/σ	9.9 (2.2)	9.2 (2.1)	14.3 (2.9)	8.3 (2.4)
CC1/2	0.99 (0.68)	0.99 (0.75)	0.99(0.81)	0.98 (0.78)
Completeness	98.2 (94.5)	99.9 (99.8)	99.8(99.0)	99.8 (99.9)
Redundancy	7.8 (7.2)	5.9 (5.8)	12.9 (12.8)	7.1 (7.5)
Refinement				
R_{work}/R_{free}	18.5/22.2	21.2/26.8	19.7/25.6	22.9/28.6
No. of Atoms	4657	4371	4451	4440
Protein	4532	4371	4451	4440
Water	123	-	-	-
RMS deviation				
Bond lengths	0.004	0.004	0.005	0.007
Bond angles	0.69	0.96	1.01	1.08
Ramachandran Favored/Outliers	99.46/0.54	98.9/1.1	99.45/0.55	99.27/0.73
B-Factor	58.6	80.2	59.9	50.2

The Cdk4 complexes were prepared for crystallization by elution from a Superdex 200 column in a buffer containing 10 mM Tris, 100 mM NaCl, and 1 mM DTT (pH 8.0). The p21-

Cdk4-CycD1 and p27-Cdk4-CycD1 complexes were crystallized by microbatch method under Al's oil at 22°C. Rods formed after three days in 100mM Tris, 10% PEG 8000 and 200mM $MgCl_2$ pH 7.0. Crystals were frozen in the reservoir solution with 25% glycerol.

The phosp27-Cdk4-CycD1 complex was prepared for crystallization by mixing equimolar amounts of phosphorylated p27 and Cdk4-CycD1 dimer followed by elution from a Superdex 200 (GE Healthcare) column in a buffer containing 10 mM Tris, 100 mM NaCl, and 1 mM DTT, pH 8.0. The complex was crystallized by sitting drop vapor diffusion method at 22°C. Rods formed after three days in 100mM Tris, 17% PEG 3350, 100 mM $CaCl_2$ and 10 mM $MgCl_2$ pH 7.0. Crystals were frozen in the reservoir solution with 25% glycerol

Data were collected at the Advanced Photon Source, Argonne National Laboratory at beamline 23-IDB and the Advanced Light Source, Laurence Berkeley National Laboratory at beamline 8.3.1. and 5.0.1. Diffraction spots were integrated using MOSFLM (Leslie, 2006), and data were merged and scaled using Scala (Bailey, 1994).The model was built with Coot (Emsley and Cowtan, 2004), and the model was refined with Phenix (Adams et al., 2010).

4.4.5 siRNA knockdown

Cells were reverse transfected with siRNAs using Dharmacon Human siGENOME RNAi targeting *CDKN1B* (p27) or Non-targeting control (Thermo Fisher). Transfection was performed using Lipofectamine RNAiMax Transfection Reagent (Invitrogen) according to manufacturer's protocol. Following 24-hour transfection, cells were incubated with palbociclib or vehicle control at the concentration indicated. Proliferation was determined using a chemiluminescent BrdU ELISA assay (Sigma 11669915001) as described by the manufacturer. Luminescence was read on a Biotek Synergy 2 plate reader. Parallel experiments were performed using immunoblot analysis in which cells were exposed to 200 nM palbociclib at to 72-hour following reverse transfection.

4.4.6 Western blot and antibodies

Primary antibodies for immunoblot analysis were obtained from Cell Signaling Technology (phosRb S807/S811, #8516; CycE1, #4129; p27, #2552; p21, #2947) and Santa Cruz Biotechnology (Actin, SC-47778; CycD1, SC-20044). Whole-cell extracts were prepared by lysing the cells with RIPA lysis buffer in the presence of 1X Halt protease inhibitor (Thermo Fisher) and 1 mM PMSF (Sigma). The extracted proteins (20 µg) were resolved by SDS-PAGE and transferred to PVDF membranes, which were then incubated with primary antibodies at 4°C overnight, followed by incubation with HRP tagged anti-mouse or anti-rabbit secondary antibodies at room temperature up to 1 hour. An enhanced chemiluminescence kit (Thermo Fisher, 34076) was used to detect the immuno-reactive bands.

Acknowledgments:

This research was supported by grants from the National Cancer Institute, NIH to K.G. (F31 CA206244), A.K.W (R01 CA211878), and S.M.R. (R01 CA132685). Data collection at the ALS Beamline 8.3.1 is supported by the UC Office of the President, Multicampus Research Programs and Initiatives Grant MR-15-328599 and Program for Breakthrough Biomedical Research, which is partially funded by the Sandler Foundation. The authors acknowledge Julien Sage for helpful discussions.

4.5 References

Adams, P.D., Afonine, P.V., Bunkoczi, G., Chen, V.B., Davis, I.W., Echols, N., Headd, J.J., Hung, L.W., Kapral, G.J., Grosse-Kunstleve, R.W*., et al.* (2010). PHENIX: a comprehensive Python-based system for macromolecular structure solution. Acta Crystallogr D Biol Crystallogr *66*, 213-221.

Anders, L., Ke, N., Hydbring, P., Choi, Yoon J., Widlund, Hans R., Chick, Joel M., Zhai, H., Vidal, M., Gygi, Stephen P., Braun, P*., et al.* (2011). A Systematic Screen for CDK4/6 Substrates Links FOXM1 Phosphorylation to Senescence Suppression in Cancer Cells. Cancer Cell *20*, 620-634.

Bailey, S. (1994). The Ccp4 Suite - Programs for Protein Crystallography. Acta Crystallographica Section D-Biological Crystallography *50*, 760-763.

Bencivenga, D., Caldarelli, I., Stampone, E., Mancini, F.P., Balestrieri, M.L., Della Ragione, F., and Borriello, A. (2017). p27(Kip1) and human cancers: A reappraisal of a still enigmatic protein. Cancer Lett *403*, 354-365.

Brotherton, D.H., Dhanaraj, V., Wick, S., Brizuela, L., Domaille, P.J., Volyanik, E., Xu, X., Parisini, E., Smith, B.O., Archer, S.J*., et al.* (1998). Crystal structure of the complex of the cyclin D-dependent kinase Cdk6 bound to the cell-cycle inhibitor p19INK4d. Nature *395*, 244-250.

Brown, N.R., Noble, M.E., Endicott, J.A., and Johnson, L.N. (1999). The structural basis for specificity of substrate and recruitment peptides for cyclin-dependent kinases. Nat Cell Biol *1*, 438-443.

Cen, L., Carlson, B.L., Schroeder, M.A., Ostrem, J.L., Kitange, G.J., Mladek, A.C., Fink, S.R., Decker, P.A., Wu, W., Kim, J.S*., et al.* (2012). p16-Cdk4-Rb axis controls sensitivity to a cyclin-dependent kinase inhibitor PD0332991 in glioblastoma xenograft cells. Neuro Oncol *14*, 870-881.

Cheng, M., Olivier, P., Diehl, J.A., Fero, M., Roussel, M.F., Roberts, J.M., and Sherr, C.J. (1999). The p21(Cip1) and p27(Kip1) CDK 'inhibitors' are essential activators of cyclin D-dependent kinases in murine fibroblasts. EMBO J *18*, 1571-1583.

Chu, I.M., Hengst, L., and Slingerland, J.M. (2008). The Cdk inhibitor p27 in human cancer: prognostic potential and relevance to anticancer therapy. Nat Rev Cancer *8*, 253-267.

Clare, P.M., Poorman, R.A., Kelley, L.C., Watenpaugh, K.D., Bannow, C.A., and Leach, K.L. (2001). The cyclin-dependent kinases cdk2 and cdk5 act by a random, anticooperative kinetic mechanism. J Biol Chem *276*, 48292-48299.

Day, P.J., Cleasby, A., Tickle, I.J., O'Reilly, M., Coyle, J.E., Holding, F.P., McMenamin, R.L., Yon, J., Chopra, R., Lengauer, C*., et al.* (2009). Crystal structure of human CDK4 in complex with a D-type cyclin. Proceedings of the National Academy of Sciences *106*, 4166-4170.

Dick, F.A., and Rubin, S.M. (2013). Molecular mechanisms underlying RB protein function. Nat Rev Mol Cell Biol *14*, 297-306.

Emsley, P., and Cowtan, K. (2004). Coot: model-building tools for molecular graphics. Acta Crystallogr D Biol Crystallogr *60*, 2126-2132.

Fero, M.L., Rivkin, M., Tasch, M., Porter, P., Carow, C.E., Firpo, E., Polyak, K., Tsai, L.H., Broudy, V., Perlmutter, R.M*., et al.* (1996). A syndrome of multiorgan hyperplasia with features of gigantism, tumorigenesis, and female sterility in p27Kip1-deficient Mice. Cell *85*, 733-744.

Finn, R.S., Martin, M., Rugo, H.S., Jones, S., Im, S.A., Gelmon, K., Harbeck, N., Lipatov, O.N., Walshe, J.M., Moulder, S*., et al.* (2016). Palbociclib and Letrozole in Advanced Breast Cancer. N Engl J Med *375*, 1925-1936.

Gibbs, C.S., and Zoller, M.J. (1991). Rational scanning mutagenesis of a protein kinase identifies functional regions involved in catalysis and substrate interactions. Journal of Biological Chemistry *266*, 8923-8931.

Grimmler, M., Wang, Y., Mund, T., Cilensek, Z., Keidel, E.M., Waddell, M.B., Jakel, H., Kullmann, M., Kriwacki, R.W., and Hengst, L. (2007). Cdk-inhibitory activity and stability of p27Kip1 are directly regulated by oncogenic tyrosine kinases. Cell *128*, 269-280.

Hallett, S.T., Pastok, M.W., Morgan, R.M.L., Wittner, A., Blundell, K., Felletar, I., Wedge, S.R., Prodromou, C., Noble, M.E.M., Pearl, L.H.*, et al.* (2017). Differential Regulation of G1 CDK Complexes by the Hsp90-Cdc37 Chaperone System. Cell Rep *21*, 1386-1398.

Harper, J.W., Adami, G.R., Wei, N., Keyomarsi, K., and Elledge, S.J. (1993). The p21 Cdk-interacting protein Cip1 is a potent inhibitor of G1 cyclin-dependent kinases. Cell *75*, 805-816.

Hunter, T., and Pines, J. (1994). Cyclins and cancer. II: Cyclin D and CDK inhibitors come of age. Cell *79*, 573-582.

James, M.K., Ray, A., Leznova, D., and Blain, S.W. (2008). Differential modification of p27Kip1 controls its cyclin D-cdk4 inhibitory activity. Molecular and cellular biology *28*, 498-510.

Jeffrey, P.D., Russo, A.A., Polyak, K., Gibbs, E., Hurwitz, J., Massague, J., and Pavletich, N.P. (1995). Mechanism of CDK activation revealed by the structure of a cyclinA-CDK2 complex. Nature *376*, 313-320.

Kato, A., Takahashi, H., Takahashi, Y., and Matsushime, H. (1997). Inactivation of the cyclin D-dependent kinase in the rat fibroblast cell line, 3Y1, induced by contact inhibition. J Biol Chem *272*, 8065-8070.

Kim, L.C., Song, L., and Haura, E.B. (2009). Src kinases as therapeutic targets for cancer. Nat Rev Clin Oncol *6*, 587-595.

Kitagawa, M., Higashi, H., Jung, H.K., Suzuki-Takahashi, I., Ikeda, M., Tamai, K., Kato, J., Segawa, K., Yoshida, E., Nishimura, S.*, et al.* (1996). The consensus motif for phosphorylation by cyclin D1-Cdk4 is different from that for phosphorylation by cyclin A/E-Cdk2. The EMBO journal *15*, 7060-7069.

Knight, Z.A., and Shokat, K.M. (2005). Features of selective kinase inhibitors. Chemistry and Biology *12*, 621-637.

Konstantinidis, a.K., Radhakrishnan, R., Gu, F., Rao, R.N., and Yeh, W.K. (1998). Purification, characterization, and kinetic mechanism of cyclin D1. CDK4, a major target for cell cycle regulation. The Journal of biological chemistry *273*, 26506-26515.

LaBaer, J., Garrett, M.D., Stevenson, L.F., Slingerland, J.M., Sandhu, C., Chou, H.S., Fattaey, A., and Harlow, E. (1997a). New functional activities for the p21 family of CDK inhibitors. Genes Dev *11*, 847-862.

LaBaer, J., Garrett, M.D., Stevenson, L.F., Slingerland, J.M., Sandhu, C., Chou, H.S., Fattaey, A., and Harlow, E. (1997b). New functional actvities for the p21 family of CDK inhibitors. Genes and Development *11*, 847-862.

Ladha, M.H., Lee, K.Y., Upton, T.M., Reed, M.F., and Ewen, M.E. (1998). Regulation of exit from quiescence by p27 and cyclin D1-CDK4. Mol Cell Biol *18*, 6605-6615.

Langan, T.A., Gautier, J., Lohka, M., Hollingsworth, R., Moreno, S., Nurse, P., Maller, J., and Sclafani, R.A. (1989). Mammalian growth-associated H1 histone kinase: a homolog of cdc2+/CDC28 protein kinases controlling mitotic entry in yeast and frog cells. Mol Cell Biol *9*, 3860-3868.

Leslie, A.G. (2006). The integration of macromolecular diffraction data. Acta Crystallogr D Biol Crystallogr *62*, 48-57.

Malumbres, M. (2014). Cyclin-dependent kinases. Genome Biol *15*, 122.

Martín-caballero, J., Flores, J.M., García-palencia, P., Martı, J., Garcı, P., and Serrano, M. (2001). Tumor Susceptibility of p21 Waf1 / Cip1 -deficient Mice. Cancer Research *61*, 6234-6238.

Ostrander, J.H., Daniel, A.R., and Lange, C.A. (2010). Brk/PTK6 signaling in normal and cancer cell models. Curr Opin Pharmacol *10*, 662-669.

Otto, T., and Sicinski, P. (2017). Cell cycle proteins as promising targets in cancer therapy. Nat Rev Cancer *17*, 93-115.

Ou, L., Ferreira, A.M., Otieno, S., Xiao, L., Bashford, D., and Kriwacki, R.W. (2011). Incomplete folding upon binding mediates Cdk4/cyclin D complex activation by tyrosine phosphorylation of inhibitor p27 protein. Journal of Biological Chemistry *286*, 30142-30151.

Pan, W., Cox, S., Hoess, R.H., and Grafstrom, R.H. (2001). A cyclin D1/cyclin-dependent kinase 4 binding site within the C domain of the retinoblastoma protein. Cancer Res *61*, 2885-2891.

Patel, P., Asbach, B., Shteyn, E., Gomez, C., Coltoff, A., Bhuyan, S., Tyner, A.L., Wagner, R., and Blain, S.W. (2015). Brk/Protein Tyrosine Kinase 6 Phosphorylates p27 KIP1 , Regulating the Activity of Cyclin D–Cyclin-Dependent Kinase 4. Molecular and Cellular Biology *35*, 1506-1522.

Patel, P., Tsiperson, V., Gottesman, S.R.S., Somma, J., and Blain, S.W. (2018). Dual Inhibition of CDK4 and CDK2 via Targeting p27 Tyrosine Phosphorylation Induces a Potent and Durable Response in Breast Cancer Cells. Molecular Cancer Research, 1-18.

Ramsey, M.R., Krishnamurthy, J., Pei, X.H., Torrice, C., Lin, W., Carrasco, D.R., Ligon, K.L., Xiong, Y., and Sharpless, N.E. (2007). Expression of p16Ink4a compensates for p18Ink4c loss in cyclin-dependent kinase 4/6-dependent tumors and tissues. Cancer Res *67*, 4732-4741.

Russo, A.A., Jeffrey, P.D., Patten, A.K., Massagué, J., and Pavletich, N.P. (1996a). Crystal structure of the p27(Kip1) cyclin-dependent-kinase inhibitor bound to the cyclin A-Cdk2 complex. In Nature, pp. 325-331.

Russo, A.A., Jeffrey, P.D., and Pavletich, N.P. (1996b). Structural basis of cyclin-dependent kinase activation by phosphorylation. Nat Struct Biol *3*, 696-700.

Russo, A.A., Tong, L., Lee, J.-O., Jeffrey, P.D., and Pavletich, N.P. (1998). Structural basis for inhibition of the cyclin-dependent kinase Cdk6 by the tumour suppressor p16 INK4a. Nature *395*, 237-243.

Schulman, B.A., Lindstrom, D.L., and Harlow, E. (1998). Substrate recruitment to cyclin-dependent kinase 2 by a multipurpose docking site on cyclin A. Proc Natl Acad Sci U S A *95*, 10453-10458.

Schulze-Gahmen, U., De Bondt, H.L., and Kim, S.H. (1996). High-resolution crystal structures of human cyclin-dependent kinase 2 with and without ATP: Bound waters and natural ligand as guides for inhibitor design. Journal of Medicinal Chemistry *39*, 4540-4546.

Schulze-Gahmen, U., and Kim, S.H. (2002). Structural basis for CDK6 activation by a virus-encoded cyclin. Nature Structural Biology *9*, 177-181.

Sherr, C.J., Beach, D., and Shapiro, G.I. (2016a). Targeting CDK4 and CDK6: From discovery to therapy. Cancer Discovery *6*, 353-367.

Sherr, C.J., Beach, D., and Shapiro, G.I. (2016b). Targeting CDK4 and CDK6: From Discovery to Therapy. Cancer Discov *6*, 353-367.

Sherr, C.J., and Roberts, J.M. (1999). CDK inhibitors: positive and negative regulators of G1-phase progression. Genes Dev *13*, 1501-1512.

Soos, T.J., Kiyokawa, H., Yan, J.S., Rubin, M.S., Giordano, A., DeBlasio, A., Bottega, S., Wong, B., Mendelsohn, J., and Koff, A. (1996). Formation of p27-CDK complexes during the human mitotic cell cycle. Cell Growth Differ *7*, 135-146.

Sperka, T., Wang, J., and Rudolph, K.L. (2012). DNA damage checkpoints in stem cells, ageing and cancer. Nat Rev Mol Cell Biol *13*, 579-590.

Takaki, T., Echalier, a., Brown, N.R., Hunt, T., Endicott, J.a., and Noble, M.E.M. (2009). The structure of CDK4/cyclin D3 has implications for models of CDK activation. Proceedings of the National Academy of Sciences of the United States of America *106*, 4171-4176.

Taylor, S.S., and Kornev, A.P. (2011). Protein kinases: Evolution of dynamic regulatory proteins. Trends in Biochemical Sciences *36*, 65-77.

Toyoshima, H., and Hunter, T. (1994). p27, a novel inhibitor of G1 cyclin-Cdk protein kinase activity, is related to p21. Cell *78*, 67-74.

Verba, K.A., Wang, R.Y.-R., Arakawa, A., Liu, Y., Shirouzu, M., Yokoyama, S., Agard, D.A., Taylor, S.S., Keshwani, M.M., Steichen, J.M.*, et al.* (2016). Atomic structure of Hsp90-Cdc37-Cdk4 reveals that Hsp90 traps and stabilizes an unfolded kinase. Science (New York, NY) *352*, 1542-1547.

Wang, H., Nicolay, B.N., Chick, J.M., Gao, X., Geng, Y., Ren, H., Gao, H., Yang, G., Williams, J.A., Suski, J.M.*, et al.* (2017). The metabolic function of cyclin D3-CDK6 kinase in cancer cell survival. Nature *546*, 426-430.

Weinberg, R.A. (1995). The retinoblastoma protein and cell cycle control. Cell *81*, 323-330.

Young, R.J., Waldeck, K., Martin, C., Foo, J.H., Cameron, D.P., Kirby, L., Do, H., Mitchell, C., Cullinane, C., Liu, W.*, et al.* (2014). Loss of CDKN2A expression is a frequent event in primary invasive melanoma and correlates with sensitivity to the CDK4/6 inhibitor PD0332991 in melanoma cell lines. Pigment Cell Melanoma Res *27*, 590-600.

Zhang, H., Hannon, G.J., and Beach, D. (1994). p21-containing cyclin kinases exist in both active and inactive states. Genes Dev *8*, 1750-1758.

Zhang, J., Bu, X., Wang, H., Zhu, Y., Geng, Y., Nihira, N.T., Tan, Y., Ci, Y., Wu, F., Dai, X.*, et al.* (2018). Cyclin D-CDK4 kinase destabilizes PD-L1 via cullin 3-SPOP to control cancer immune surveillance. Nature *553*, 91-95.

Chapter 5: MuvB and nucleosome binding

5.1 Introduction

The DNA in the nucleus of the eukaryotic cell is organized and packaged by histones into chromatin, which can be either in an active open euchromatin state, or a repressed condensed histone-rich heterochromatin state (Wang et al. 2016). The histone proteins wrapping DNA form an octamer complex consisting of two histone 2A/B dimers, and a single histone 3/4 tetramer. A double DNA wrap (~146bp) around a single octamer constitutes the nucleosome-core-particle (NCP) (Luger et al. 1997). Nucleosomes spanning promoter regions of the genome have distinct positions, whereas intergenic nucleosomes are, in general, scattered and random (Yuan et al. 2005). Housekeeping genes have more open and less phased promoters than genes under temporal regulation (Lee et al. 2007). The transcriptional start site (TSS) has low occupancy of nucleosomes, and the width of this "nucleosome free" region (NFR) changes with the state of transcriptional activity (Deniz et al. 2016). The positions of nucleosomes relative to the transcriptional start site (TSS) can distinguish between active or repressed genes. Active genes tend to have open nucleosome free regions and lower occupancy of the -1 nucleosome, where housekeeping genes have essentially no -1 nucleosome (Lee et al. 2007). During the cell cycle, nucleosome positioning is rearranged such that the NFR width is greatest during S-phase and the -1 nucleosome is less enriched (Deniz et al. 2016). The S phase of the cell cycle is the point at which most transcription of cell cycle dependent genes occurs (Liu et al. 2017). The mechanism that directs -1 nucleosome occupancy in a cell cycle dependent manner is not known.

The MuvB complex is an evolutionary conserved regulator of cell cycle dependent gene expression (Litovchick et al. 2007). MuvB consists of five core proteins (LIN54, LIN9, LIN37, LIN52 and RBAP48) that remain in the complex throughout the cell cycle. During quiescence and G1, MuvB functions as a repressor of cell cycle dependent genes when associated with p130-E2F4-DP1 (DREAM) (Litovchick et al. 2007). When cells enter S

phase, MuvB forms a new complex with B-Myb to activate mitotic genes (MMB) (Sadasivam et al. 2012). Although MuvB's function is established as a transcriptional regulator, the mechanism it executes to mediate this function is not known. Given MuvB can bind DNA through LIN54, and histone H3 through RBAP48, we hypothesize that it is playing a role in mediating the width of the NFR surrounding the TSS. Recently, it was shown that MuvB acts as a repressor in the absence of the LIN35 pocket protein in *C. elegans* (Goetsch et al. 2017). *C. elegans* also do not encode for a Myb protein, altogether suggesting MuvB's innate function is a repressor. We therefore propose that MuvB plays a role in binding to and stabilizing the -1 nucleosome position, and that B-Myb acts as an antagonist to remove the nucleosome from this position.

5.2 Results

5.2.1 *MuvB and B-Myb binds to a probed nucleosome-core-particle*

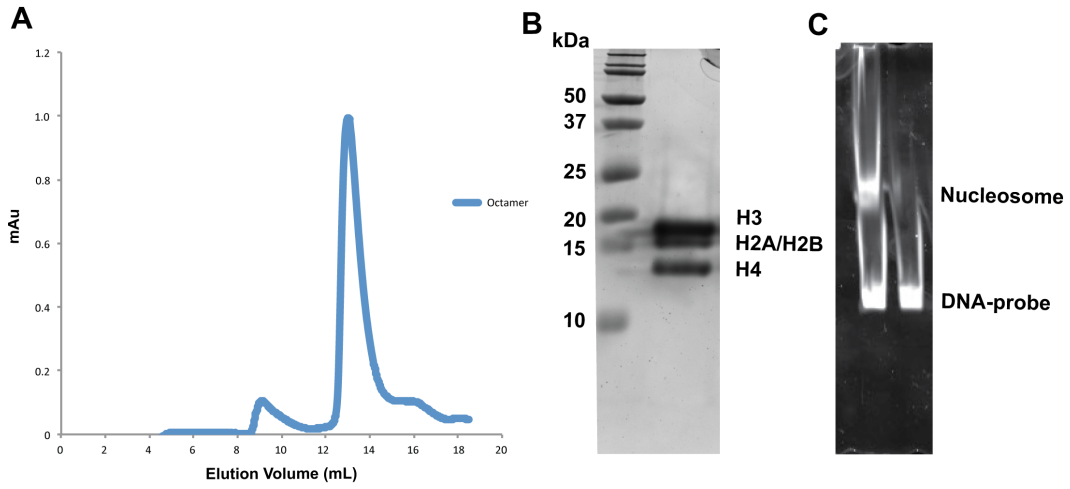

Figure 5.1. Recombinant histones assemble into the nucleosome-core-particle. (A) Refolded histone octamer co-elutes on SD200 column. (B) SDS-PAGE of the peak fraction contains the four histones. (C) A native PAGE shows the shift in MW when octamer is added to the DNA-probe.

To determine whether the MuvB complex can bind the NCP, and if B-Myb disrupts this interaction, we reconstituted human MuvB and MMB from Sf9 cells (**Figure 3.2**), and the nucleosome-core-particle from *X. laevis* histones in E. coli (**Figure 5.1**). To monitor binding, we labeled the nucleosome positioning sequence (601) (Lowary and Widom 1998) with fluorescein. We used a fluorescence polarization (FP) assay to determine the strength of NCP interactions with MuvB and MMB. We found that MuvB and RBAP48 bind the nucleosome with similar affinity (**Figure 5.2**). The cell cycle homology region (CHR) is a DNA motif that is recognized by MuvB core protein LIN54 (Marceau et al. 2016). The MuvB complex was found to bind nucleosomes with 4-fold higher affinity compared to the CHR. We also found that MuvB does not interact with the 601 sequence non-specifically, altogether suggesting MuvB can bind to the NCP.

Given the -1 nucleosome occupancy in cell-cycle gene promoters is reduced during S-phase when B-Myb is recruited to MuvB, we reasoned that B-Myb binding to MuvB would weaken the affinity for the nucleosome. Contrary to our original hypothesis, MMB bound the nucleosome with 85-fold higher affinity compared to MuvB. Moreover, B-Myb and MMB binding affinity was comparable. B-Myb phosphorylation by CDK2-cyclin A is correlated with enhanced transcriptional transactivation (Lane et al. 1997). We tested whether phosphorylation of B-Myb altered its interaction with the NCP. The FP ratio was significantly altered between phosphorylated and unphosphorylated forms of B-Myb suggesting an alternative conformation between these two states. The affinity for the NCP was reduced 3-fold upon phosphorylation, suggesting although a conformational change occurs, it does not seem to significantly affect nucleosome binding.

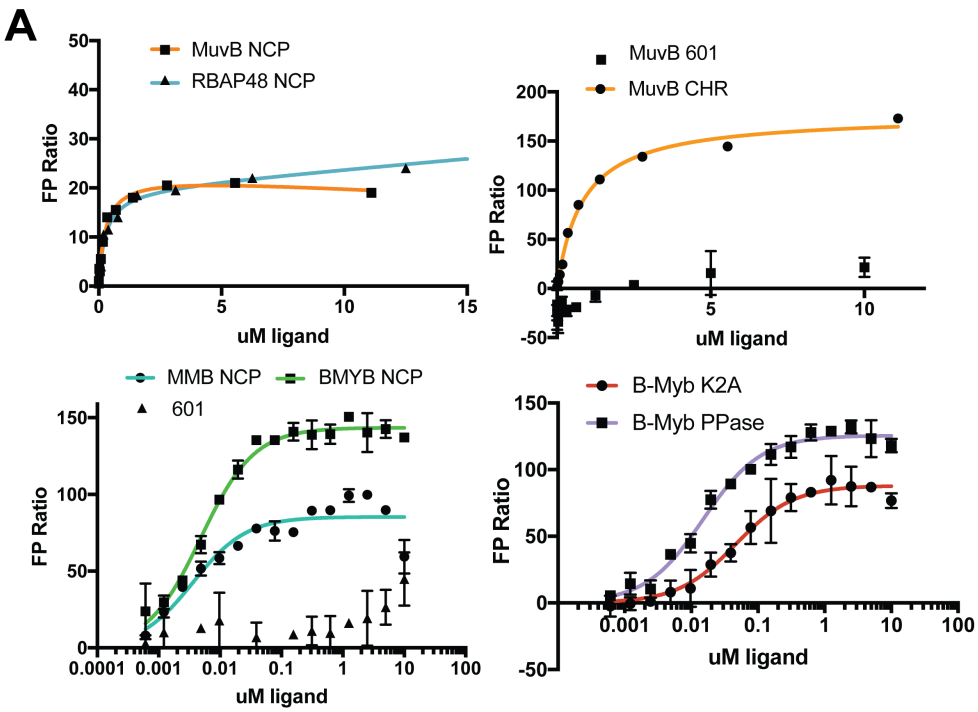

B

Protein	NCP K_D (nM)	DNA	K_D (nM)
MuvB	310 ± 50	CHR	830 ± 60
		601	-
MMB	3.6 ± 0.7		
B-Myb	4.9 ± 0.4	601	-
B-Myb PPase	15.1 ± 0.1		
B-Myb K2A	46.4 ± 0.8		
RBAP48	280 ± 50		

Figure 5.2. MuvB and MMB bind the NCP. (A) FP plots for MuvB and MMB binding to the NCP. (B) K_D values calculated from the FP assay.

5.3 Discussion

The MuvB complex can function as a repressor and an activator of transcription at different phases during the cell cycle. The innate function of MuvB is a repressor and the recruitment of B-Myb is necessary to de-repress mitotic genes (Goetsch et al. 2017)(Sadasivam et al. 2012). Our hypothesis for this mechanism was that B-Myb

recruitment results in the disruption of MuvB-nucleosome interactions. Strikingly, we found that B-Myb alone is sufficient to bind nucleosomes, and when in complex with MuvB, enhances its interaction

B-Myb has been shown to interact with the transcriptional co-activator p300 to transactivate genes (Saville and Watson 1998)(Schubert et al. 2004). It is possible that the B-Myb interaction with the nucleosome is a priming mechanism to directly recruit p300 histone acetyltransferase activity to the +1 nucleosomes on Myb-MuvB target gene promoters, analogous to what has previously been seen for CREB and CBP (Zhang et al. 2000).

Given that B-Myb did not disrupt MuvB binding to the nucleosome, an alternative for MuvB's repressor function could be to inhibit H3K4me3 on the +1 nucleosome. The +1 nucleosome is where peak H3K4 methylation occurs and is a signature of active genes (Soares et al. 2017). The structure of the H3 tail bound to RBAP48 revealed that H3K4 is buried in the center of the beta propeller domain, potentially shielding the residue from activator chromatin modifiers such as mixed-lineage leukemia (MLL) (Schmitges et al. 2011).

5.4 Materials and Methods

5.4.1 Protein expression, purification

Human LIN52, LIN37, RBBP48, LIN9, LIN54 and B-Myb were expressed and purified from Sf9 cells (Expression Systems, Davis CA) using baculovirus vectors as described previously.

Xenopus laevis H2A, H2B, H3 and H4 were expressed separately using pET vector in E. coli BL21 pLysS cells. The cells were induced with 0.2 mM IPTG and grown at 37°C for 3-4 hours. The bacterial pellet was resuspended in a buffer composed of 50 mM Tris pH 8, 1M NaCl, 2M Urea. The cells were lysed, and centrifuged at 19000 rpm for 30 min. The pellet was resuspended in the same buffer and centrifuged again. This step was repeated three

more times. The washed pellet was then resuspended in 7M guanidine HCl, 20 mM Tris pH 8 and 10 mM DTT. The resuspended pellet was then incubated at 37℃ for 10 minutes. The solubilized inclusion bodies were cleared by centrifugation at 19000 for 30 min. The supernatant was then dialyzed into 50 mM NaOAc pH 5 and 1 mM 2-mercaptoethanol. The protein was then loaded onto a SOURCE S cation exchange column in 50 mM NaOAc pH 5, 6M urea, 100 mM NaCl, 5 mM 2-mercaptoethanol, and eluted in the same buffer as a gradient with 1M NaCl. Pooled fractions were then dialyzed into water with 1 mM 2-mercaptoethanol and lyophilized.

To reconstitute the histone octamer, equimolar amounts of histone were resuspended in a buffer containing 7M guanidine HCl, 20 mM Tris pH 8 and 10 mM DTT. The dissolved histones were dialyzed in a buffer containing 20 mM Tris pH 8, 2M NaCl, 1 mM EDTA and 5 mM 2-mercaptoethanol overnight at 4℃. The Octamer was then eluted from a Superdex 200 (GE Healthcare) column in a buffer containing 20 mM Tris pH 8, 2M NaCl, 1 mM EDTA and 5 mM 2-mercaptoethanol. The octamer was then stored at -80℃ in the presence of 20% glycerol.

5.4.2 Nucleosome reconstitution

To reconstitute the nucleosome-core-particle, the WIDOM 601 positioning sequence was amplified by PCR with forward primer 5'-ATCCCTATACGCGGCCGCCCTGGA-3' and reverse primer fluorescein-5'-ACAGGATGTATATATCTGACACGTG-3'. The DNA was purified by gel-extraction. Following purification, the DNA was resuspended with equimolar amounts of histone octamer in a buffer containing 20 mM Tris pH 8, 2M NaCl, 1 mM EDTA and 10 mM DTT. The suspended octamer and DNA mixture was then dialyzed into a low salt buffer containing 20 mM Tris pH 8, 250mM NaCl, 1 mM EDTA and 10 mM DTT over 48 hours at 4℃. The nucleosome-core-particle was then analyzed and purified from 5% native PAGE.

5.4.3 Fluorescence Polarization Assay

fluorescein-labeled nucleosome was mixed at 20 nM with MuvB, RBAP48, B-Myb or MMB in a buffer containing 50 mM Tris, 50 mM NaCl, 1 mM DTT, 0.1% Tween, pH 8.0. 20 µL of the reaction was used for the measurement in a 384-well plate well. FP measurements were made in triplicate using a Perkin-Elmer EnVision plate reader.

5.5 References

Anscombe E, Meschini E, Mora-Vidal R, Martin MP, Staunton D, Geitmann M, Danielson UH, Stanley WA, Wang LZ, Reuillon T, et al. 2015. Identification and Characterization of an Irreversible Inhibitor of CDK2. *Chem Biol* **22**: 1159–1164. http://dx.doi.org/10.1016/j.chembiol.2015.07.018.

Bryant KL, Mancias JD, Kimmelman AC, Der CJ. 2014. KRAS: Feeding pancreatic cancer proliferation. *Trends Biochem Sci* **39**: 91–100. http://dx.doi.org/10.1016/j.tibs.2013.12.004.

Burke JR, Hura GL, Rubin SM. 2012. Structures of inactive retinoblastoma protein reveal multiple mechanisms for cell cycle control. 1156–1166.

Cerqueira A, Hunt S, Tardy C, Newton K, Santamarı D, Dubus P, Malumbres M, Barbacid M, Ca JF. 2007. Cdk1 is sufficient to drive the mammalian cell cycle. **448**: 811–816.

Chen D, Pacal M, Wenzel P, Knoepfler PS, Leone G, Bremner R. 2009. Division and apoptosis of E2f-deficient retinal progenitors. *Nature* **462**: 925–929. http://dx.doi.org/10.1038/nature08544.

Chu I, Sun J, Arnaout A, Kahn H, Hanna W, Narod S, Sun P, Tan CK, Hengst L, Slingerland J. 2007. p27 Phosphorylation by Src Regulates Inhibition of Cyclin E-Cdk2. *Cell* **128**: 281–294.

Cilloni D, Saglio G. 2012. Molecular pathways: BCR-ABL. *Clin Cancer Res* **18**: 930–937.

Cobrinik D, Lee MH, Hannon G, Lee DCM, Hannon G, Mulligan G, Bronson RT, Dyson N, Harlow E, Beach D, et al. 1996. Shared role of the pRB-related pl30 and pi07 proteins in limb development. 1633–1644.

Cooper G. 2000. *The Cell: A Molecular Approach*. 2nd ed.

Dannenberg JH, Schuijff L, Dekker M, Van Der Valk M, Te Riele H. 2004. Tissue-specific tumor suppressor activity of retinoblastoma gene homologs p107 and p130. *Genes Dev* **18**: 2952–2962.

Dawson MA. 2017. The cancer epigenome: Concepts, challenges, and therapeutic opportunities. *Science (80-)* **1**: 379–385. http://science.sciencemag.org/content/355/6330/1147/tab-pdf.

Deniz Ö, Flores O, Aldea M, Soler-López M, Orozco M. 2016. Nucleosome architecture throughout the cell cycle. *Sci Rep* **6**: 1–11. http://dx.doi.org/10.1038/srep19729.

Dick F a, Rubin SM. 2013a. Molecular mechanisms underlying RB protein function. *Nat Rev Mol Cell Biol* **14**: 297–306. http://www.ncbi.nlm.nih.gov/pubmed/23594950 (Accessed August 15, 2013).

Dick FA, Rubin SM. 2013b. Molecular mechanisms underlying RB protein function. *Nat Rev Mol Cell Biol* **14**: 297–306. http://dx.doi.org/10.1038/nrm3567.

Ding Q, Zhang Z, Liu JJ, Jiang N, Zhang J, Ross TM, Chu XJ, Bartkovitz D, Podlaski F, Janson C, et al. 2013. Discovery of RG7388, a potent and selective p53-MDM2 inhibitor in clinical development. *J Med Chem* **56**: 5979–5983.

Donehower LA, Harvey M, Slagle BL, McArthur MJ, Montgomery CA, Butel JS, Bradley A. 1992. Mice deficient for p53 are developmentally normal but susceptible to spontaneous tumours. *Nature* **356**: 215–221. http://www.nature.com/doifinder/10.1038/356215a0.

ElSawy KM, Verma CS, Joseph TL, Lane DP, Twarock R, Caves LSD. 2013. On the interaction mechanisms of a p53 peptide and nutlin with the MDM2 and MDMX proteins: A Brownian dynamics study. *Cell Cycle* **12**: 394–404.

Fischer M. 2017. Census and evaluation of p53 target genes. *Oncogene* **36**: 3943–3956. http://dx.doi.org/10.1038/onc.2016.502.

Fischer M, Steiner L, Engeland K. 2014. The transcription factor p53: Not a repressor, solely an activator. *Cell Cycle* **13**: 3037–3058.

Fletcher O, Easton D, Anderson K, Gilham C, Jay M, Peto J. 2004. Lifetime risks of common cancers among retinoblastoma survivors. *J Natl Cancer Inst* **96**: 357–363.

Foster DA, Yellen P, Xu L, Saqcena M. 2011. Regulation of G1 cell cycle progression: Distinguishing the restriction point from a nutrient-sensing cell growth checkpoint(s). *Genes and Cancer* **1**: 1124–1131.

Gil J, Peters G. 2006. Regulation of the INK4b-ARF-INK4a tumour suppressor locus: All for one or one for all. *Nat Rev Mol Cell Biol* **7**: 667–677.

Goetsch PD, Garrigues JM, Strome S. 2017. Loss of the Caenorhabditis elegans pocket protein LIN-35 reveals MuvB's innate function as the repressor of DREAM target genes. *PLoS Genet* **13**: 1–25.

Guiley KZ, Liban T, Felthousen J, Ramanan P, Litovchick L, Rubin SM. 2015. Structural mechanisms of DREAM complex assembly and regulation. *Genes Dev* **120**: 1–9.

Hanahan D, Weinberg RA. 2000. The hallmarks of cancer. *Cell* **100**: 57–70. http://www.ncbi.nlm.nih.gov/pubmed/10647931.

Hanahan D, Weinberg R a. 2011. Hallmarks of cancer: The next generation. *Cell* **144**: 646–674. http://dx.doi.org/10.1016/j.cell.2011.02.013.

Hardy PA, Zacharias H. 2005. Reappraisal of the Hansemann e Boveri hypothesis on the origin of tumors. **29**.

Herrera-abreu MT, Palafox M, Asghar U, Rivas MA, Cutts RJ, Garcia-murillas I, Pearson A, Guzman M, Elliott R, Rodriguez O, et al. 2016. Early Adaptation and Acquired Resistance to CDK4 / 6 Inhibition in Estrogen Receptor – Positive Breast Cancer.

Hukkelhoven E, Liu Y, Yehs N, Ciznadijas D, Blain SW, Koffs A. 2012. Tyrosine phosphorylation of the p21 cyclin-dependent kinase inhibitor facilitates the development of proneural glioma. *J Biol Chem* **287**: 38523–38530.

Jacks T, Fazeli A, Schmitt EM, Bronson RT, Goodell MA, Weinberg RA. 1992. Effects of an Rb mutation in the mouse. *Nature* **359**: 295–300.

Jackson PK. 2008. BenchMarks The Hunt for Cyclin. 199–202.

James MK, Ray A, Leznova D, Blain SW. 2008. Differential modification of p27Kip1 controls its cyclin D-cdk4 inhibitory activity. *Mol Cell Biol* **28**: 498–510.

Jeffrey P, Russo A, Polyak K, Gibbs E. 1995. Mechanism of CDK activation revealed by the structure of a cyclinA-CDK2 complex. *Nature*. http://www.chem.uwec.edu/Webpapers2005/twarosed/sources/1FIN_journal.pdf (Accessed June 24, 2014).

Jiang H, Karnezis AN, Tao M, Guida PM, Zhu L. 2000. pRB and p107 have distinct effects when expressed in pRB-deficient tumor cells at physiologically relevant levels. *Oncogene* **19**: 3878–87. http://www.ncbi.nlm.nih.gov/pubmed/10951581.

Jiang L, Sheikh MS, Huang Y. 2010. Decision Making by p53: Life versus Death. *Mol Cell Pharmacol* **2**: 69–77. http://www.pubmedcentral.nih.gov/articlerender.fcgi?artid=2877278&tool=pmcentrez&rendertype=abstract.

Kandoth C, Mclellan MD, Vandin F, Ye K, Niu B, Lu C, Xie M, Zhang Q, Mcmichael JF, Wyczalkowski MA, et al. 2013. Mutational landscape and significance across 12 major cancer types. *Nature* **502**: 333–339.

Kastenhuber ER, Lowe SW. 2017. Putting p53 in Context. *Cell* **170**: 1062–1078. http://dx.doi.org/10.1016/j.cell.2017.08.028.

Kleinerman RA, Tucker MA, Tarone RE, Abramson DH, Seddon JM, Stovall M, Li FP, Fraumeni JF. 2005. Risk of new cancers after radiotherapy in long-term survivors of retinoblastoma: An extended follow-up. *J Clin Oncol* **23**: 2272–2279.

Knudson a G. 2001. Two genetic hits (more or less) to cancer. *Nat Rev Cancer* **1**: 157–162.

Knudson AG. 1971. Mutation and Cancer : Statistical Study of Retinoblastoma. **68**: 820–823.

Koretzky G a. 2007. Review series introduction The legacy of the Philadelphia chromosome. *J Clin Invest* **117**: 2030–2032.

Krupczak-Hollis K, Wang X, Kalinichenko V V., Gusarova GA, Wang IC, Dennewitz MB, Yoder HM, Kiyokawa H, Kaestner KH, Costa RH. 2004. The mouse Forkhead Box m1 transcription factor is essential for hepatoblast mitosis and development of intrahepatic bile ducts and vessels during liver morphogenesis. *Dev Biol* **276**: 74–88.

Lane AN, Fan TWM. 2015. Regulation of mammalian nucleotide metabolism and biosynthesis. *Nucleic Acids Res* **43**: 2466–2485.

Lane S, Farlie P, Watson R. 1997. B-Myb function can be markedly enhanced by cyclin A-dependent kinase and protein truncation.

Lee MG, Nurse P. 1987. Complementation used to clone a human homologue of the fission yeast cell cycle control gene cdc2. *Nature* **327**: 31–5.

Lee W, Tillo D, Bray N, Morse RH, Davis RW, Hughes TR, Nislow C. 2007. A high-resolution atlas of nucleosome occupancy in yeast. *Nat Genet* **39**: 1235–1244.

Leone G, Sears R, Huang E, Rempel R, Nuckolls F, Park CH, Giangrande P, Wu L, Saavedra HI, Field SJ, et al. 2001. Myc requires distinct E2F activities to induce S phase and apoptosis. *Mol Cell* **8**: 105–113.

Liban TJ, Medina EM, Tripathi S, Sengupta S, Henry RW, Buchler NE. 2017. Conservation and divergence of C-terminal domain structure in the retinoblastoma protein family.

Linzer DIH, Levine AJ. 1979. Characterization of a 54K Dalton cellular SV40 tumor antigen present in SV40-transformed cells and uninfected embryonal carcinoma cells. *Cell* **17**: 43–52.

Litovchick L, Sadasivam S, Florens L, et al. 2007. Evolutionarily Conserved Multisubunit RBL2/p130 and E2F4 Protein Complex Represses Human Cell Cycle-Dependent Genes in Quiescence. *Mol Cell* **3**: 539–551. http://www.sciencedirect.com/science/article/pii/S1097276507002511 (Accessed October 29, 2013).

Liu H, Tang X, Srivastava A, Pécot T, Daniel P, Hemmelgarn B, Reyes S, Fackler N, Bajwa A, Kladney R, et al. 2015. Redeployment of Myc and E2f1 – 3 drives Rb -deficient cell cycles. **17**.

Liu Y, Chen S, Wang S, Soares F, Fischer M, Meng F, Du Z, Lin C, Meyer C, DeCaprio JA, et al. 2017. Transcriptional landscape of the human cell cycle. *Proc Natl Acad Sci* **114**: 3473–3478. http://www.pnas.org/lookup/doi/10.1073/pnas.1617636114.

Lloyd AC. 2013. XThe regulation of cell size. *Cell* **154**: 1194–1205. http://dx.doi.org/10.1016/j.cell.2013.08.053.

Lowary PT, Widom J. 1998. New DNA sequence rules for high affinity binding to histone octamer and sequence-directed nucleosome positioning. *J Mol Biol* **276**: 19–42.

Lowe D. 2013. Overselling p53 Drugs. http://blogs.sciencemag.org/pipeline/archives/2013/01/03/overselling_p53_drugs.

Luger K, Mäder AW, Richmond RK, Sargent DF, Richmond TJ. 1997. Crystal structure of the nucleosome core particle at 2.8 Å resolution. *Nature* **389**: 251–260.

Luna RM de O, Wagner DS, Lozano G. 1995. Rescue of early embroyonic lethality in mdm2-deficient mice by deletion of p53. *Nature*.

Malkin D, Li F, Strong L, Fraumeni J, Nelson C, Kim D, Kassel J, Gryka M, Bischoff F, Tainsky M, et al. 1990. Germ line p53 mutations in a familial syndrome of breast cancer, sarcomas, and other neoplasms. *Science (80-)* **250**: 1233–1238. http://www.sciencemag.org/cgi/doi/10.1126/science.1978757.

Malumbres M, Barbacid M. 2009. Cell cycle, CDKs and cancer: A changing paradigm. *Nat Rev Cancer* **9**: 153–166.

Marceau AH, Felthousen JG, Goetsch PD, Iness AN, Lee H-W, Tripathi SM, Strome S, Litovchick L, Rubin SM. 2016. Structural basis for LIN54 recognition of CHR elements in cell cycle-regulated promoters. *Nat Commun* **7**: 12301. http://www.nature.com/doifinder/10.1038/ncomms12301.

Martı J, Flores JM, Garcı P, Serrano M. 2001. Tumor Susceptibility of p21 Waf1 / Cip1 - deficient Mice 1. 6234–6238.

Medsker B, Forno E, Simhan H, Juan C, Sciences R. 2016. An oncogenic MYB feedback loop drives alternate cell fates in adenoid cystic carcinoma. *Nat Genet* **70**: 773–779.

Mesri EA, Feitelson MA, Munger K. 2014. Human viral oncogenesis: A cancer hallmarks analysis. *Cell Host Microbe* **15**: 266–282. http://dx.doi.org/10.1016/j.chom.2014.02.011.

Munger K, Gwin TK, Mclaughlin-drubin M. 2013. p16 in HPV-associated cancers. **4**.

Musa J, Aynaud M-M, Mirabeau O, Delattre O, Grünewald TG. 2017. MYBL2 (B-Myb): a central regulator of cell proliferation, cell survival and differentiation involved in tumorigenesis. *Cell Death Dis* **8**: e2895. http://www.nature.com/doifinder/10.1038/cddis.2017.244.

Myatt SS, Lam EW-F-F. 2007. The emerging roles of forkhead box (Fox) proteins in cancer. *Nat Rev Cancer* **7**: 847–59. http://www.nature.com/doifinder/10.1038/nrc2223%0Ahttp://dx.doi.org/10.1038/nrc2223.

Ohshima K, Hatakeyama K, Nagashima T, Watanabe Y, Kanto K, Doi Y, Ide T, Shimoda Y, Tanabe T, Ohnami S, et al. 2017. Integrated analysis of gene expression and copy number identified potential cancer driver genes with amplification-dependent overexpression in 1,454 solid tumors. *Sci Rep* **7**: 1–13. http://dx.doi.org/10.1038/s41598-017-00219-3.

Ohtani N, Zebedee Z, Huot TJG, Stinson JA, Sugimoto M, Ohashi Y, Sharrocks AD, Peters G, Hara E. 2001. Opposing effects of Ets and Id proteins on p16INK4a expression during cellular senescence. *Nature* **409**: 1067–1070. http://www.nature.com/doifinder/10.1038/35059131.

Otto T, Sicinski P. 2017. Cell cycle proteins as promising targets in cancer therapy. *Nat Rev Cancer* **17**: 93–115. http://dx.doi.org/10.1038/nrc.2016.138.

Pardee AB, Li CJ, Reddy GPV, Kaelin WG, Ann B. 2004. Concepts nd es Bio sci en Do No t D ist r. 1091–1094.

Park SJ, Woo SJ, Park KH. 2014. Incidence of retinoblastoma and survival rate of

retinoblastoma patients in Korea using the Korean National Cancer Registry Database (1993-2010). *Investig Ophthalmol Vis Sci* **55**: 2816–2821.

Paweletz N. 2001. Walther Flemming : pioneer of mitosis research. **2**: 72–75.

Poppy Roworth A, Ghari F, La Thangue NB. 2015. To live or let die – complexity within the E2F1 pathway. *Mol Cell Oncol* **2**: e970480. https://www.tandfonline.com/doi/full/10.4161/23723548.2014.970480.

Ressler S, Bartkova J, Niederegger H, Bartek J, Scharffetter-Kochanek K, Jansen-Dürr P, Wlaschek M. 2006. p16INK4A is a robust in vivo biomarker of cellular aging in human skin. *Aging Cell* **5**: 379–389.

Russo AA, Jeffrey PD, Patten AK, Massagué J, Pavletich NP. 1996. Crystal structure of the p27(Kip1) cyclin-dependent-kinase inhibitor bound to the cyclin A-Cdk2 complex. *Nature* **382**: 325–331.

Sadasivam S, DeCaprio JA. 2013. The DREAM complex: Master coordinator of cell cycle-dependent gene expression. *Nat Rev Cancer* **13**: 585–595.

Sadasivam S, Duan S, DeCaprio JA. 2012. The MuvB complex sequentially recruits B-Myb and FoxM1 to promote mitotic gene expression. *Genes Dev* **26**: 474–489.

Saville MK, Watson RJ. 1998. The cell-cycle regulated transcription factor B-Myb is phosphorylated by cyclin A/Cdk2 at sites that enhance its transactivation properties. *Oncogene* **17**: 2679–2689.

Schmitges FW, Prusty AB, Faty M, Stützer A,
Lingaraju GM, Aiwazian J, Sack R, Hess D, Li L, Zhou S, et al. 2011. Histone Methylation by PRC2 Is Inhibited by Active Chromatin Marks. *Mol Cell* **42**: 330–341.

Schubert S, Horstmann S, Bartusel T, Klempnauer KH. 2004. The cooperation of B-Myb with the coactivator p300 is orchestrated by cyclins A and D1. *Oncogene* **23**: 1392–1404. http://www.ncbi.nlm.nih.gov/entrez/query.fcgi?cmd=Retrieve&db=PubMed&dopt=Citation&list_uids=14973551.

Sherr CJ, Beach D, Shapiro GI. 2016. Targeting CDK4 and CDK6: From discovery to therapy. *Cancer Discov* **6**: 353–367.

Sherr CJ, McCormick F. 2002. The RB and p53 pathways in cancer. *Cancer Cell* **2**: 103–112.
Soares LM, He PC, Chun Y, Suh H, Kim TS, Buratowski S. 2017. Determinants of Histone H3K4 Methylation Patterns. *Mol Cell* **68**: 773–785.e6. https://doi.org/10.1016/j.molcel.2017.10.013.

Tanaka Y, Patestos NP, Maekawa T, Ishii S. 1999. B-myb is required for inner cell mass formation at an early stage of development. *J Biol Chem* **274**: 28067–28070.

Tyner SD. 2002. P53 Mutant Mice That Display Early Aging-Associated Phenotypes. *Nature* **415**: 45–53. http://dx.doi.org/10.1038/415045a.

Vogelstein BB, Hughes MDH, Kimmel S, Cancer C. 2010. p53 : The Most Frequently Altered Gene in Human Cancers. 1–6.

Wang J, Jia ST, Jia S. 2016. New Insights into the Regulation of Heterochromatin. *Trends Genet* **32**: 284–294. http://dx.doi.org/10.1016/j.tig.2016.02.005.

Wirt SE, Sage J. 2010. P107 in the public eye: An Rb understudy and more. *Cell Div* **5**: 1–13.

Yuan G, Liu Y, Dion MF, Slack MD, Wu LF, Altschuler SJ, Oliver J. 2005. Genome-Scale Identification of Nucleosome Positions in S . Cerevisiae. 626–631.

Zetterberg A, Larsson O, Wiman KG. 1995. What is the restriction point? *Curr Opin Cell Biol* **7**: 835–842.

Zhang Q, Vo N, Goodman RH. 2000. Histone binding protein RbAp48 interacts with a complex of CREB binding protein and phosphorylated CREB. *Mol Cell Biol* **20**: 4970–8. http://www.pubmedcentral.nih.gov/articlerender.fcgi?artid=85947&tool=pmcentrez&rendertype=abstract.

Zhao R, Choi BY, Lee MH, Bode AM, Dong Z. 2016. Implications of Genetic and Epigenetic Alterations of CDKN2A (p16INK4a) in Cancer. *EBioMedicine* **8**: 30–39. http://dx.doi.org/10.1016/j.ebiom.2016.04.017.